

Design and Experimental Applications of Acoustic Metamaterials

by

Lucian Zigoneanu

Department of Electrical and Computer Engineering
Duke University

Date: _____

Approved:

Steven A. Cummer, Supervisor

Donald B. Bliss

Martin A. Brooke

William T. Joines

David R. Smith

Dissertation submitted in partial fulfillment of the requirements for the degree of
Doctor of Philosophy in the Department of Electrical and Computer Engineering
in the Graduate School of Duke University
2013

ABSTRACT

Design and Experimental Applications of Acoustic Metamaterials

by

Lucian Zigoneanu

Department of Electrical and Computer Engineering
Duke University

Date: _____

Approved:

Steven A. Cummer, Supervisor

Donald B. Bliss

Martin A. Brooke

William T. Joines

David R. Smith

An abstract of a dissertation submitted in partial fulfillment of the requirements for
the degree of Doctor of Philosophy in the Department of Electrical and Computer
Engineering
in the Graduate School of Duke University
2013

Copyright © 2013 by Lucian Zigoneanu
All rights reserved except the rights granted by the
Creative Commons Attribution-Noncommercial Licence

Abstract

Acoustic metamaterials are engineered materials that were extensively investigated over the last years mainly because they promise properties otherwise hard or impossible to find in nature. Consequently, they open the door for improved or completely new applications (e.g. acoustic superlens that can exceed the diffraction limit in imaging or acoustic absorbing panels with higher transmission loss and smaller thickness than regular absorbers). Our objective is to surpass the limited frequency operating range imposed by the resonant mechanism that some of these materials have. In addition, we want acoustic metamaterials that could be experimentally demonstrated and used to build devices with overall performances better than the previous ones reported in the literature.

Here, we start by focusing on the need of engineered metamaterials in general and acoustic metamaterials in particular. Also, the similarities between electromagnetic metamaterials and acoustic metamaterials and possible ways to realize broadband acoustic metamaterials are briefly discussed. Then, we present the experimental realization and characterization of a two-dimensional (2D) broadband acoustic metamaterial with strongly anisotropic effective mass density. We use this metamaterial to realize a 2D broadband gradient index acoustic lens in air. Furthermore, we optimize the lens design by improving each unit cell's performance and we also realize a 2D acoustic ground cloak in air. In addition, we explore the performance of some novel applications (a 2D acoustic black hole and a three-dimensional (3D) acoustic

cloak) using the currently available acoustic metamaterials. In order to overcome the limitations of our designs, we approach the active acoustic metamaterials path, which offers a broader range for the material parameters values and a better control over them. We propose two structures which contain a sensing element (microphone) and an acoustic driver (piezoelectric membrane or speaker). The material properties are controlled by tuning the response of the unit cell to the incident wave. Several samples with interesting effective mass density and bulk modulus are presented.

We conclude by suggesting few natural directions that could be followed for the future research based on the theoretical and experimental results presented in this work.

To all who made this possible.

Contents

Abstract	iv
List of Figures	x
1 Introduction	1
1.1 Electromagnetic Metamaterials	2
1.2 Acoustic Metamaterials	4
1.3 From EM Metamaterials to Acoustic Metamaterials	6
1.4 Motivation	8
1.5 Contributions	9
2 Broadband 2D Acoustic Metamaterial with Anisotropic Mass Density	12
2.1 Experimental Development of 1D Waveguide for Reflection and Transmission Measurements	15
2.2 Unit Cell Design	18
2.3 Measurement Results	19
2.4 Perforated Plates Designed as Acoustic Metamaterials	26
2.5 Transmission Loss Measurements for Perforated Plates	28
2.6 Conclusions	36
3 Broadband 2D Gradient Index Acoustic Lens	37
3.1 Design of the Index of Refraction Profile	38
3.2 Lens Characterization	46

3.3	Conlusions	51
4	Sound Manipulation Using Transformation Acoustics and Acoustic Metamaterials	52
4.1	2D Acoustic Black Hole	53
4.2	3D Acoustic Ground Cloak	59
4.2.1	Square Pyramid Shaped Cloak	60
4.2.2	Cone Shaped Cloak	64
4.2.3	Crescent Shaped Cloak	67
4.3	Conclusions	69
5	Active Acoustic Metamaterials	70
5.1	Motivation	70
5.2	One Path to AAMM	71
5.3	Theoretical Model	73
5.4	Piezoelectric Based Active Acoustic Metamaterial	75
5.4.1	Experimental Design	75
5.4.2	Measurements and Results	76
5.4.3	Theoretical Model Evaluation	81
5.5	Piezoelectric Based Active Acoustic Metamaterial - Rectangular Unit Cell	82
5.6	Speaker Based Active Acoustic Metamaterials - Rectangular Unit Cell	86
5.7	Conclusions	89
6	Conclusions and Suggested Future Work	90
6.1	Summary	90
6.2	Suggested Future Work	91
	Appendix A Description of the Data Acquisition Process in the 1D Acoustic Waveguides (Circular and Rectangular)	93

Appendix B Description of the Data Acquisition Process in the 2D Parallel Plate Acoustic Waveguide	96
Appendix C 3D Acoustic Cloak Transformations	102
C.1 Square Pyramid Cloak	102
C.2 Cone Shaped Cloak	104
C.3 Crescent Shaped Cloak	105
Bibliography	107
Biography	113

List of Figures

2.1	Incident, reflected and transmitted wave fields for three-medium problem.	13
2.2	1D Waveguide Experimental setup: 1 - microphone and preamplifier; 2 - sample holder; 3 - NI terminal block; 4 - anechoic termination; 5 - example of the signal sent from PC; 6 - example of signals collected at the microphones before the sample (top) and after the sample (bottom).	15
2.3	Microphone preamplifier design.	16
2.4	(a) Unit cell used to analyze the effective density and material properties;(b) Unit cell orientation and the samples that were generated using it.	19
2.5	(a) Simulations for acoustic plane wave propagation in the x direction ($f = 3$ kHz);(b) Simulations for acoustic plane wave propagation in the y direction ($f = 3$ kHz); (c) Broadband effective mass density in the x direction; (d) Broadband effective mass density in the y direction.	20
2.6	Example of signals used to determine the reflection and transmission coefficients: (a) Initial signals collected at Channel 1 with sample, air and perfect reflector (incident signal and first reflection, aligned); (b) Isolated first reflection; (c) Reflected signal from the sample modified in amplitude and phase to overlap over the signal from perfect reflector.	21
2.7	Propagation in the x direction. Reflection and transmission coefficients amplitude (a) and phase (b).	22
2.8	Propagation in the y direction. Reflection and transmission coefficients amplitude (a) and phase (b).	24
2.9	Effective mass density and bulk modulus in the x direction.	25
2.10	Effective mass density and bulk modulus in the y direction.	25

2.11	Perforated plate unit cell used to analyze the effective density and bulk modulus: x orientation.	27
2.12	Perforated plate unit cell used to analyze the effective density and bulk modulus: y orientation.	28
2.13	Measured pressure field for ground (top left), empty waveguide (bottom left), ground and object to hide (top right) and the cloaked object plus the ground (bottom right).	29
2.14	BSWA Impedance tube system: (a) actual system; (b) schematic diagram.	30
2.15	Transmission loss for one unit cell, measured and simulated for the ideal case.	33
2.16	Transmission loss for one unit cell, measured and simulated for the non-ideal case.	34
2.17	Transmission loss for more than one unit cell in the propagation direction, non-ideal case.	35
3.1	(a) GRIN lens and its orientation; (b) Desired index of refraction along the direction transverse to propagation direction.	39
3.2	(a) Unit cell with square solid inclusion (first attempt); (b) Actual lens simulation for unit cells made with square rods commercially available.	41
3.3	(a) Unit cell dimensions;(b) Index of refraction vs. a dimension of the cross;(c) Simulations for acoustic wave propagation ($f = 3$ kHz).	42
3.4	Frequency dependence of the material parameters for the largest cross unit cell.	43
3.5	(a) Index of refraction along the direction transverse on the propagation direction (desired and realized in practice);(b) Unit cells impedance and their position on the axis perpendicular to propagation direction.	44
3.6	(a)Unit cell dimensions;(b)Simulations for acoustic wave propagation ($f = 3\text{kHz}$).	46
3.7	Comparison between simulated sound fields for an idealized lens with continuous material parameters (left) the actual structured lens (right).	47
3.8	The actual lens, side and top view (left column) and the actual waveguide where the measurements are performed with the GUI that we created (right column).	48

3.9	(a) Simulated pressure field amplitude (left) and phase (right) for continuous lens domain; (b) Measured pressure field amplitude (left) and phase (right); (c) Pressure amplitude (arbitrary units) on a line passing through the focal point in the propagation direction (left) and in a direction transverse on the propagation direction (right).	49
3.10	(a) Simulated pressure fields for the entire domain (left) and measured/simulated pressure amplitude slices through focal point and far away from the focal point at 4.5 kHz (right);(b) Simulated pressure fields for the entire domain (left) and measured/simulated pressure amplitude slices through focal point and far away from the focal point at 1.5 kHz (right).	50
4.1	Ray trajectories inside an artificial black hole.	54
4.2	2D acoustic black hole pressure field map ($f=12$ kHz, maximum index of refraction 2.5).	56
4.3	2D acoustic black hole pressure field map ($f=12$ kHz, maximum index of refraction 6).	57
4.4	2D acoustic black hole pressure field map ($f=3$ kHz, maximum index of refraction 6).	58
4.5	2D acoustic black hole pressure field map (maximum index of refraction 6, $f=12$ kHz (a) and $f=3$ kHz (b)).	59
4.6	3D acoustic cloak for a square pyramid solid object.	60
4.7	Cross sectional pressure field maps for: (a) perfect reflector, (b) square pyramid object to hide, (c) square pyramid object to hide and ideal cloak, (d) square pyramid object to hide and non ideal cloak ($m=2.5$).	62
4.8	(a)Unit cell and (b) cloaking shell filling suggestions for square pyramid cloak.	63
4.9	3D acoustic cloak for a cone shaped solid object.	65
4.10	Cross sectional pressure field maps for: (a) perfect reflector, (b) cone shaped object to hide, (c) cone shaped object to hide and ideal cloak, (d) cone shaped object to hide and non ideal cloak ($m=2.5$).	66
4.11	3D acoustic cloak for a cone shaped solid object.	67
4.12	3D acoustic cloak for a crescent shaped solid object.	67

4.13	Cross sectional pressure field maps for: (a) perfect reflector, (b) crescent shaped object to hide, (c) crescent shaped object to hide and ideal cloak, (d) crescent shaped object to hide and non ideal cloak ($m=2.5$)	68
5.1	Schematic diagram of an active acoustic metamaterial unit cell: (a) sensing element and active driving circuit, (b) acoustic driver.	71
5.2	AAMM unit cell based on a cavity and a piezoelectric membrane.	72
5.3	Snapshots of a 1D PZT based AAMM unit cell: (a) front view (towards the incident wave) and (b) back view.	75
5.4	PZT based AAMM sample 1: real part (top) and imaginary part (bottom) for the effective mass density and bulk modulus.	77
5.5	PZT based AAMM sample 2: real part (top) and imaginary part (bottom) for the effective mass density and bulk modulus.	78
5.6	PZT based AAMM sample 3: real part (top) and imaginary part (bottom) for the effective mass density and bulk modulus.	80
5.7	Measured theoretical model parameters for: (a) sample 1, (b) sample 2 and (c) sample 3.	81
5.8	(a) custom made rectangular acoustic waveguide, (b) rectangular, PZT based active acoustic metamaterial with front view (left, towards the incident wave) and back view (right).	83
5.9	Numerical simulation results for a perforated panel used as a holder for rectangular, PZT based active acoustic metamaterial.	84
5.10	PZT based AAMM sample 4: real part (top) and imaginary part (bottom) for the effective mass density and bulk modulus.	85
5.11	Speaker based AAMM sample, front view (left, towards the incident wave) and back view (right).	87
5.12	Numerical simulation results for a perforated panel used as a holder for rectangular, speaker based active acoustic metamaterial.	87
5.13	Speaker based AAMM sample 1: real part (top) and imaginary part (bottom) for the effective mass density and bulk modulus.	88
B.1	2D acoustic waveguide graphical user interface.	97
B.2	2D acoustic waveguide: schematic diagram.	98

C.1	Cross section square pyramid cloak.	102
C.2	Cross section cone cloak.	104

1

Introduction

People have tried for centuries to understand and eventually control materials behavior and scientists invested a large amount of energy and knowledge to determine mathematical or physical models and equations that explain how materials work.

The ground zero for all the advancements in the applied sciences is given by improvements in materials used either we talk about engineering, optics or computing technology. And, for thousands of years, scientists used the same classic approach: given the chemical elements from the periodic table, find a better recipe and a proper technology to develop a material with better properties. Scientists have been so stubborn in using this method not because of a lack of imagination. They needed a feasible method capable of working with the macroscopic characteristics of a material and to produce palpable results. And yet, we are still far away from the end of the chemical combinations that can be made. On the other hand, despite tremendous results gained along this track, its limitations made some scientists to look for other possible paths. Is it possible that instead of atoms to use a set of macroscopic structures periodically disposed in space such that the new material will act as a continuous medium? Will the new material have properties that do not exist in

nature? The answer to these questions was yes and a new term emerged in literature: metamaterials. This new field promises to create new materials with new properties by using artificial elements [1].

The term metamaterials was introduced for the first time in 1999 and was used to describe “**Macroscopic composites having a manmade, three-dimensional, periodic cellular architecture designed to produce an optimized combination, not available in nature, of two or more responses to a specific excitation**” [2]. Even though this definition enlightens the reader about what metamaterials are, the terms *response* and *excitation* are very broad. Also, it is not very clear if metamaterials draw their behavior from chemical composition too and not only from the cellular arrangements. In consequence, a new and more specific definition was needed. Since the most forward steps in the field of metamaterials were made in the electromagnetic (EM) area, a definition commonly accepted among the EM scientists is: “**A metamaterial is a macroscopic composite of periodic or non-periodic structure, whose function is due to both the cellular architecture and the chemical composition**” [3]. Although this definition is also broad, it can be subsequently improved by adding specific characteristics. For example, if the effective medium theory is to be used, the metamaterials are required to have unit cells much smaller than the wavelength. Two major research branches have been developed in the field of metamaterials: basic theory and applications [1]. As expected, new materials require new research tools. That is, one will need new physical models and new mathematical tools (e.g. a new set of equations could be the physical model and a new numerical solver could be the mathematical tool).

1.1 Electromagnetic Metamaterials

As of now, it is impossible to take into consideration the deepest internal structure of a sample material (i.e. each atom) that contains an enormous number of de-

grees of freedom and then to quantify what happens when an electromagnetic wave travels through. In consequence, a macroscopic model is necessary. This model will somehow average the individual contributions. After numerous years of experimental observations, Maxwell formulated a model and a set of equations (known as Maxwell's equations) which use a small number of parameters to describe the EM wave - matter interaction. The following constitutive relations are used to describe this interaction:

$$D = \epsilon E + \alpha H \quad (1.1)$$

$$B = \beta E + \mu H \quad (1.2)$$

where D and B are electric and magnetic flux densities, E and H are electric and magnetic fields, ϵ , α , β , μ are material parameters. For most materials α and β parameters (used to describe the electric sample response to magnetic fields and magnetic sample response to electric fields) are zero. Electric permittivity (ϵ) and magnetic permeability (μ) are tridimensional tensors. Most of natural materials offer a relatively small range and positive value for electric permittivity and magnetic permeability. Thus, the main motivation was to develop metamaterials with a large spectrum of values (even negative) for permeability and permittivity.

It was only in 1967 that Veselago theoretically demonstrated for the first time that materials with negative constitutive parameters can exist (i.e. do not contradict Maxwell equations) or be manufactured [4]. Although some natural materials can exhibit a negative permittivity for certain frequencies, this is not the case for permeability. Almost three decades after Veselago's work, Pendry et al. proposed a wire structure to realize a negative permittivity and, later on, a split ring resonator (SRR) to realize a negative permeability [5, 6]. One year later, Smith et al. announced the successful combination of the two structures and the first realization of a metamaterial with negative index of refraction (NIM) [7].

After the design of the first electromagnetic metamaterials, the new field of metamaterials has fully emerged and numerous research groups have designed novel devices. For example, the left-handed materials (metamaterials that have simultaneously negative materials parameters) exhibit interesting properties and could lead to great applications. From the electromagnetic wave reflection and propagation point of view: the refracted beam is in the same half space as the incident beam, considering the entire space divided in two halves by the surface normal. This could be used for perfect lenses that, unlike the conventional lenses, could break the diffraction limit [8, 9, 10].

However, not only metamaterials with negative materials parameters are of great interest. Having the ability to create and precisely control the values for permittivity and permeability (positive or negative) lead to a new theory: transformation optics [11]. This technique allows an accurate control over the way that the wave propagates through the materials (e.g. bending and stretching of EM waves is possible) and was used to implement in practice novel applications such as cloaking devices (a coating applied to arbitrarily shaped objects in order to make them invisible to electromagnetic radiation) [12].

1.2 Acoustic Metamaterials

The possibility to have EM metamaterials that exhibit material properties challenging or impossible to obtain in natural materials and to rigorously control them has ignited the interest for a new class of materials: acoustic metamaterials. Intensive theoretical and experimental research has been done in the last few years in order to explore this new field.

Again, the main motivation is to develop structures with a large range of values (including negative values) for material properties, bulk modulus and mass density. These material properties are defined as follows:

$$B = -V \frac{dp}{dV} \quad (1.3)$$

$$\rho = \frac{dp}{dV} \frac{F}{V} \quad (1.4)$$

where B is the bulk modulus, V is the volume, p is the pressure, ρ is the density, F is the applied force. As it was the case for electromagnetic metamaterials, the index of refraction could be defined as:

$$n^2 = \frac{B_0}{B} \frac{\rho}{\rho_0} \quad (1.5)$$

Chan et al. demonstrated theoretically that an acoustic metamaterial with both negative bulk modulus and effective mass density is physically realizable [13]. They showed that in order to have a propagating plane wave inside the structure, B and ρ should be both either positive or negative. That is, n could have negative values if both B and ρ are negative. Moreover, they considered a particular case of rubber spheres suspended in water and showed that negative bulk modulus and negative mass density are obtained from a single resonant structure. This is not the case for electromagnetic metamaterials where the negative permittivity and permeability are derived from two distinct mechanisms. Once again it is worth mentioning that: (1) such materials with both negative bulk modulus and density do not exist in nature and (2) it is also extremely important, as we will see later, that material parameters can be precisely controlled even if they do not have negative values.

Engineered materials with negative effective density and/or negative bulk modulus have been demonstrated in literature [13, 14, 15, 16]. Corresponding applications for these kind of materials have been shown and include: the acoustic superlens [17], the magnifying acoustic hyperlens [18] that can exceed the diffraction limit in imaging and are easier to manufacture than conventional lenses, and acoustic ab-

sorbing panels [19] with higher transmission loss and smaller thickness than regular absorbers.

1.3 From EM Metamaterials to Acoustic Metamaterials

There are two paths that led the scientists to acoustic metamaterials. The direct route started in the early 1990s when a particular class of engineered materials began to be studied: acoustic phononic crystals (APC). These crystals consist of a periodic structure with elastic or fluid inclusions inside of another fluid matrix. When each unit cell is spatially distributed on the order of acoustic wavelength, they exhibit interesting properties such as focusing through negative refraction. This effect is not actually caused by a negative refraction index but by a complex mixture of the waves transmitted through inclusions and through entire structure with scattered waves (Bragg scattering) [20, 21]. Or, as a different example, it has been shown that periodic structures formed from solid cylinders placed in a fluid or gaseous background could act as a homogeneous medium, with specific effective parameters controlled by the filing ratio [22, 23, 24].

The indirect path consisted in two different routes. One approach was to design something similar with electromagnetic materials. That is, to use localized resonant structures that will create an interaction (constructive or destructive, as desired) between large scattered fields and reradiated fields. These structures with local resonating "cells" could be furthermore classified into:

- a) *intrinsic acoustic metamaterials*, where resonances are created by inclusions which have a phase speed significantly smaller than the phase speed of the fluid matrix. For example, these inclusions could be made of rubber, which has a phase speed with two orders of magnitude smaller than regular solids [13, 25].

b) *inertial acoustic metamaterials*, where local resonances in each unit cell are created by structures that act like a mass-spring-damper oscillator. There are two types of resonators currently used in acoustic metamaterials fields: Helmholtz resonators (a cavity in a rigid material connected to the fluid through a narrow neck) and coated rubber spheres or cylinders.

A second, different approach started from the observation that EM and acoustic waves are both waves and, at least intuitively, the way that these waves interact with matter should be analogous. Therefore, the theory and perhaps the design techniques and applications could be extrapolated to some extent from EM metamaterials to acoustic metamaterials. For the EM case, Maxwell's equations are invariant to coordinate transformation. This leads to the concept of transformation electromagnetics [11]. This is not the case for acoustic wave equations which are not transformation invariant in general [26]. However, for two-dimensional (2D) case the acoustic wave equations are transformation invariant [27]. For example, z-invariant 2D transverse electric Maxwell equations and acoustic equations are exactly the same if the following set of variable exchange is used:

$$[-E_z, -H_\phi, -H_r, \mu_\phi, \mu_r, \epsilon_z] <-> [p, v_r, v_\phi, \rho_r, \rho_\phi, B^{-1}]; \quad (1.6)$$

where E and H are the electric and magnetic fields, ϵ and μ are magnetic permeability and permittivity, p is the pressure, v is the velocity, ρ and B are density and bulk modulus. The subscripts represent the corresponding cylindrical components.

Later on it has been shown that the three-dimensional (3D) acoustic wave equations are transformation invariant if the way in which the velocity vector and pressure scalar change is different than the electric and magnetic field vectors change in the EM case [28, 29]. This work has led to the concept of transformation acoustics [28, 27, 30, 31, 32, 33], in which arbitrary bending of acoustic waves can be realized

using acoustic metamaterials that generally have anisotropic mass density. Several material design methods have been proposed in order to achieve this anisotropy and to control the effective material parameters in the desired way: elastic cylinders with a special spatial arrangement [34], concentric multilayers of isotropic sonic crystals [35, 32], rigid inclusions disposed in an array [36, 37], arrays of fluid cavities joined by piezoelectric edges [38] or Helmholtz resonators with piezoelectric diaphragms [39]. However, some of these designs have resonant mechanisms and consequently a reduced operating frequency range, while others offer a large impedance mismatch with the surroundings and only a small portion of the sound energy goes through the device.

1.4 Motivation

Metamaterials in general and the acoustic metamaterials in particular are extremely promising because these engineered materials have extreme and/or rigorously controlled properties. In addition, it is a relatively new topic with a little bit more over a decade of scientific investigations. This presumably offers numerous paths yet to be explored. However, before and during the time of the researched summarized here, there is a lack of experimental implementations. There are certain reasons for these limitations, described in detail in this dissertation, like hard to obtain extreme material parameters or limited operating frequency range. Therefore, a certain need is present to fill this gap, that is to experimentally confirm theoretically designed devices using acoustic metamaterials. We search for acoustic metamaterials that have precisely controlled values for the mass density and bulk modulus. Moreover, these values need to be easily tunable and vary on a relatively large scale. Also, we want that the final products realized using our acoustic metamaterials to be as broadband as possible and, not the last, easy to fabricate.

1.5 Contributions

We start with specific applications and use numerical simulations to design proper acoustic metamaterials, with specific effective material parameters. We experimentally characterize these materials and then use them in the desired configuration and evaluate the overall performance of the device. Overall, this work produced six peer reviewed authored/coauthored journal publications (three as first author), one peer reviewed conference paper (first author), three conference talks, and three poster presentations. Here, we specifically summarize the contributions to the acoustic metamaterials research field:

- Experimentally demonstrated that an asymmetric solid inclusion in air background will produce a 2D anisotropic mass density and a bulk modulus that are rigorously controlled and tuned. In order to characterize our samples, I have built a 1D acoustic waveguide and used a non-standard method to measure the reflection and transmission coefficients. More specifically, instead of using a standard and standing wave method, we send a particularly designed pulse through the acoustic tube. Then, the reflection and transmission coefficients are measured and inverted in order to obtain the mass density and bulk modulus. [*L. Zigoneanu, B. I. Popa, A.F. Starr, and S. A. Cummer. Design and measurements of a broadband 2d acoustic metamaterial with anisotropic mass density. Journal of Applied Physics, 109:054906, 2011.*]
- Used the insights from the previous work and designed an isotropic, optimized, cross shaped unit cell that could be used to experimentally create a gradient index of refraction. The desired refractive index is used to create a flat, 2D gradient index lens. In order to characterize the final device, I have built a 2D, parallel plate acoustic waveguide where we can measure the pressure field

maps and compare them with the theoretical ones. [L. Zigoneanu, B. I. Popa, and S. A. Cummer. Design and measurements of a broadband two-dimensional acoustic lens. Phys. Rev. B, 84:024305, 2011.]

- Furthermore, the unit cell and therefore the lens were optimized using a genetic algorithm approach. My contributions targeted the design, fabrication and measurement steps. [D. Li, L. Zigoneanu, B. I. Popa and S. A. Cummer. Design of an Acoustic Metamaterial Lens Using Genetic Algorithms. JASA, 132:2823, 2012.].
- Contributed to evaluation of the feasibility of acoustic metamaterial unit cells for a 2D ground cloak, and to the fabrication and the measurement of a 2D acoustic ground cloak in air background.[B. I. Popa, L. Zigoneanu, and S. A. Cummer. Experimental acoustic ground cloak in air. Phys. Rev. Lett., 106:253901, 2011.]
- Characterized the perforated plates as acoustic metamaterials, measuring their transmission loss and absorption. [L. Zigoneanu, B. I. Popa, and S. A. Cummer. Experimental characterization of perforated plates as acoustic metamaterials. (to be submitted, 2013)]
- Evaluated the performance of a 2D artificial black hole and a 3D acoustic ground cloak realized using the currently available acoustic metamaterials. They were not implemented in practice yet due to their large size and the lack of the corresponding experimental setup to characterize them.[L. Zigoneanu, B. I. Popa, S. A. Cummer. Sound manipulation with acoustic metamaterials. Proceedings of the Internoise 2012/ASME NCAD meeting, New York NY (2012).]
- Contributed to the fabrication and measurements of a labyrinthine acoustic

metamaterial structure used for experimental demonstration of broadband negative refractive index. [Y. Xie, B. I. Popa, L. Zigoneanu, and S. A. Cummer (*in review, 2013*).]

- Contributed to the design process of new, active acoustic metamaterials which use a sensing element and an active element (piezoelectric membrane or speaker) to control the reflected and transmitted acoustic energy by the material, therefore its effective material properties.

2

Broadband 2D Acoustic Metamaterial with Anisotropic Mass Density

As we have seen in the introductory chapter, metamaterials topic is not only about composites that have negative material parameters, but also about materials with anisotropic or spatially variant material parameters. Moreover, these material parameters can have a wide range of values and could be precisely controlled.

The primary goal of the work presented in this chapter was to experimentally validate the effective parameters of the unit cell designed theoretically using a procedure previously described in the literature [37]. We developed a one dimensional (1D) waveguide where we can measure the reflection and transmission coefficients and used a retrieval method to compute the effective mass density and effective bulk modulus from these reflection and transmission coefficients.

The problem that we have to solve is well known: propagation of an acoustic plane wave through three-media (Fig. 2.1, adapted from Ref. [40]).

The pressure fields in the media I, II, III could be written as (the time-dependent term is not shown) [40] :

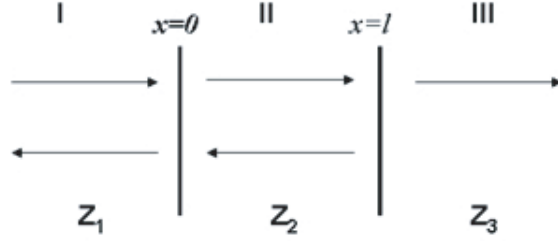


FIGURE 2.1: Incident, reflected and transmitted wave fields for three-medium problem [40].

$$P_I = A_1 e^{-j k_1 x} + B_1 e^{+j k_1 x} \quad (2.1)$$

$$P_{II} = A_2 e^{-j k_2 x} + B_2 e^{+j k_2 x} \quad (2.2)$$

$$P_{III} = A_3 e^{-j k_3 (x-l)} \quad (2.3)$$

where k is the wavenumber.

Using the boundary conditions at the interfaces (i.e. continuity of pressure and particle velocity), general expressions for transmission (A_3/A_1) and reflection (B_1/A_1) coefficients could be found:

$$T = \frac{2}{(1 + Z_1/Z_3) \cos k_2 l + j(Z_2/Z_3 + Z_1/Z_2) \sin k_2 l} \quad (2.4)$$

$$R = \frac{(1 - Z_1/Z_3) \cos k_2 l + j(Z_2/Z_3 - Z_1/Z_2) \sin k_2 l}{(1 + Z_1/Z_3) \cos k_2 l + j(Z_2/Z_3 + Z_1/Z_2) \sin k_2 l} \quad (2.5)$$

where Z is the characteristic acoustic impedance, k is the wave number and the subscripts denote the media **I**, **II** or **III**. Particular cases could be derived based

on the value of k_2l relatively to wavelength (e.g. $k_2l = n\pi$, an even number of half wavelengths).

In order to retrieve the effective acoustic material properties, density and bulk modulus, from reflection and transmission coefficients, we used the findings for retrieving the EM material parameters from reflection and transmission coefficients [41] and then apply the duality between electromagnetism and acoustics in the 2D case [27].

Assuming that regions **I** and **III** are air and region **II** is the material of interest, in electromagnetism the following relations for refractive index n and impedance Z could be obtained inverting the expressions for reflection and transmission coefficients:

$$n = \pm \frac{1}{k_0 l} \cos^{-1} \left[\frac{1}{2T} (1 - R^2 + T^2) + 2\pi m \right] \quad (2.6)$$

$$Z = \pm \sqrt{\frac{(1 + R)^2 - T^2}{(1 - R)^2 - T^2}} \quad (2.7)$$

where m is an arbitrary integer. Then, using the above mentioned duality, we can write:

$$\rho = nZ \leftrightarrow \mu \quad (2.8)$$

$$B = Z/n \leftrightarrow \epsilon^{-1} \quad (2.9)$$

We should note that the same results (2.6,2.7,2.8,2.9) were obtained in a similar way by writing the equations (2.4,2.5) for acoustic waves and then inverting them in order to get the effective density and bulk modulus [42]. Also, it has been shown in the same work that the ambiguity of the sign branch in equations (2.6,2.7) could be

eliminated by imposing the condition that the real part of Z is positive (for passive acoustic metamaterials).

2.1 Experimental Development of 1D Waveguide for Reflection and Transmission Measurements

Having the method to determine the effective material parameters, the next step was to design the experimental setup that will allow us to generate the acoustic plane wave - material interaction and to measure the reflection and transmission coefficients. Although professional impedance tube kits for acoustic material measurements are commercially available (e.g. *Brüel and Kjær*), we chose to build our own waveguide in the lab, given the versatility in design offered by this solution. The schematic diagram and a photograph of the actual experimental setup are presented Fig. 2.2 (adapted from Ref. [43]).

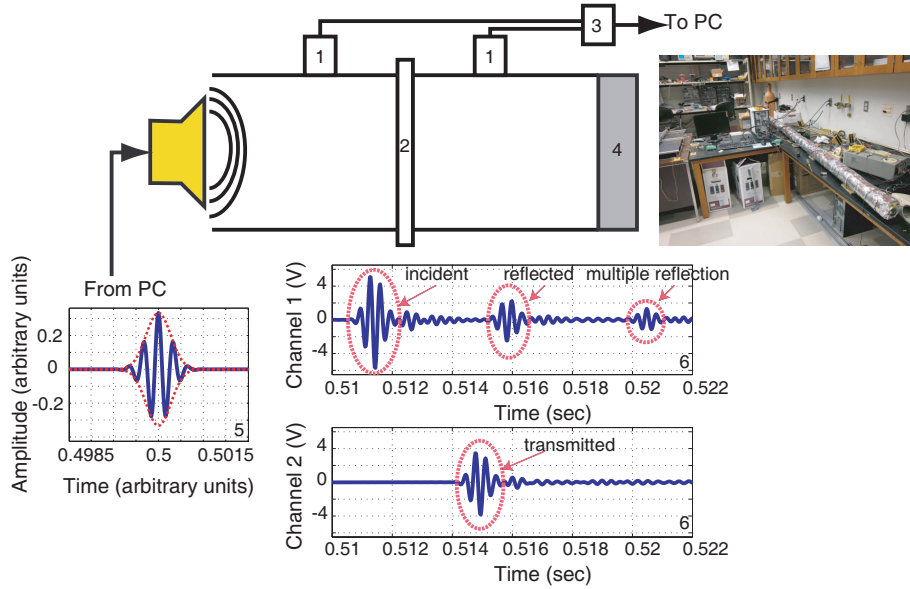
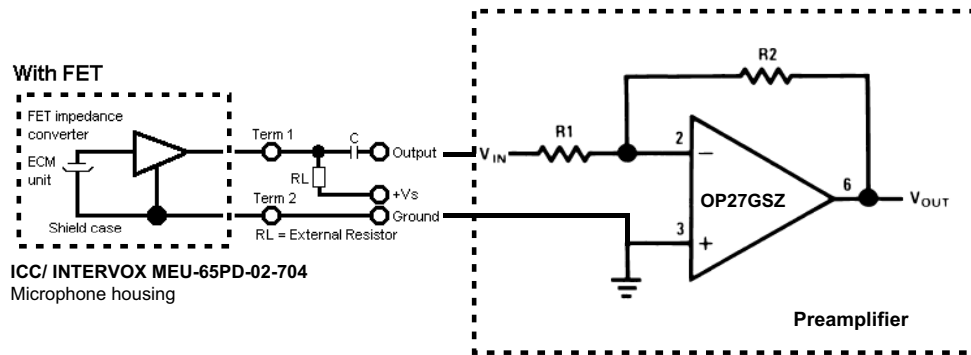


FIGURE 2.2: 1D Waveguide Experimental setup: 1 - microphone and preamplifier; 2 - sample holder; 3 - NI terminal block; 4 - anechoic termination; 5 - example of the signal sent from PC; 6 - example of signals collected at the microphones before the sample (top) and after the sample (bottom).

The waveguides are circular PVC pipes of 3" inner diameter and 0.25" thick, wrapped in foil and fiberglass insulation. The speaker is a regular external PC speaker of 3" diameter. It was decided that the frequency range of interest will be lower than 3 KHz. This will allow us to have a relatively large waveguide, which makes the sample fabrication and holding system easier. Also, this frequency range is suitable for the microphones used (unidirectional electret condenser microphones, chosen based on their relatively small size, 6 mm diameter; moreover, they have a relatively large signal/noise ratio (>38dB) and a frequency range between 100Hz-12kHz were other factors that makes them suitable for our experiment).

The signals from each microphone are then passed to a preamplifier. We choose to make one very simple amplifier for each channel (Fig. 2.3). The values used for the discrete electronic components are: $C=10 \mu F$, $RL=27 k\Omega$, $Vs=15 V$, $R1=100 \Omega$, $R2= 220 k\Omega$. The operational amplifier used is a low noise, precision amplifier produced by Analog Devices, OP27.



Adapted from: http://www.icc107.com/Search/Product_Description_inc_print2.cfm?search&PartNum=MEU-65PD-02-704

FIGURE 2.3: Microphone preamplifier design.

The single-ended signals from each preamplifier are then transferred to a terminal block (*National Instruments*TM (NI), unshielded, 68-PIN I/O, CB-68LP) via BNC connectors and 50Ω coaxial cables. A shielded cable (NI SHC68-68) is used to transfer the signals from terminal block to the first two analog inputs of an NI high speed, multifunction data acquisition (DAQ) card (NI PCI-6251 M). *Matlab*[®] codes are used to generate the waveforms via computer speaker and to collect the data via NI DAQ. The data acquisition is manually triggered, the sampling frequency is 44.1 KHz and the amplitude resolution is 16 bit. Several measurements are made and averaged in order to increase the signal to noise ratio.

An amplitude modulation (AM) like signal is obtained by a product between a cosine function and a Gaussian pulse is sent from the computer to the speaker (Fig. 2.2):

$$s_i(t) = \exp[-0.74(f_0 t)^2] \cos(2\pi f_0 t) \quad (2.10)$$

where f_0 is the desired frequency and t is the time.

This kind of signal ensures that the pulse is sufficiently small in time such that the incident and reflection pulses do not overlap and not so broad in frequency such that the material parameters will be relatively constant along the bandwidth. Since we want to measure broadband samples, we chose a Gaussian pulse width of 5 periods of the sinusoidal signal of frequency f_0 . The ratio of full width half power bandwidth to central frequency is 0.455, which is a relatively wide bandwidth. This, again, is not a problem for our broadband samples, but it could be unsuitable for materials with strong frequency dispersion.

2.2 Unit Cell Design

In addition to proving that the design methodology previously proposed [37] is experimentally valid, we imposed some other requirements for the metamaterial designed.

Our aim was to have:

- a) the effective material properties (effective mass density and effective bulk modulus) relatively unchanged in a large frequency range;
- b) a unit cell that is significantly subwavelength such that our engineered material could be described in terms of effective material parameters;
- c) a material with anisotropic effective mass density and with the ratio between the relevant components of the mass density tensor of at least 2, a value that is usually required by transformation acoustics applications;
- d) last but not the least, a set of dimensions for the unit cell that obey the subwavelenght requirement and that will generate samples which could be relatively easy to fabricate and measured in our experimental setup.

This set of requirements led to the unit cell presented in Fig. 2.4 (a) and (b) (adapted from Ref. [43]). The samples were made in Aluminum because it is highly available and easy to machine.

The theorecticsl effective material parameters are retrieved from two sets of simulations performed using Acoustic-Structure Interaction (frequency response analysis) module of *COMSOL®* Multiphysics simulation environment (Fig. 2.5(a,b),adapted from Ref. [43]). The two pressure fields computed when a plane wave is normally incident onto each sample are used to determine the reflection and transmission coefficients which, in turn, are inverted using the procedure previously described in order to obtain the effective material parameters. As can be seen in Fig. 2.5(c,d) (adapted

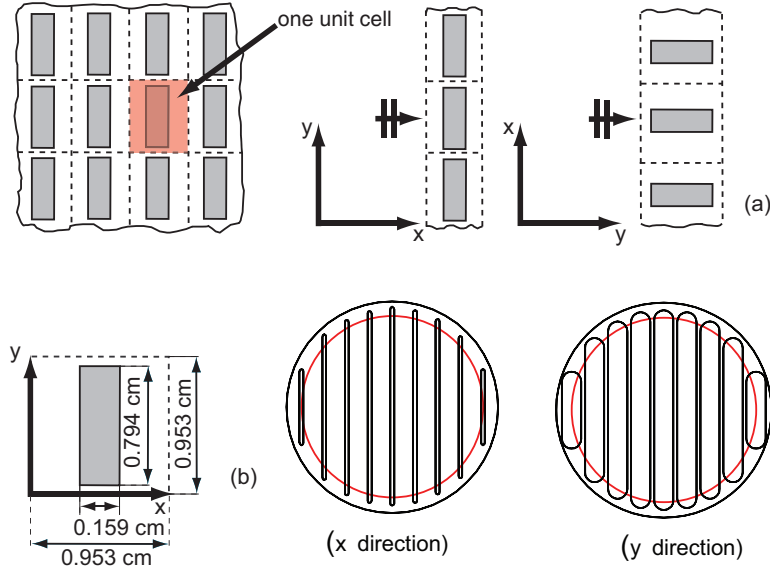


FIGURE 2.4: (a) Unit cell used to analyze the effective density and material properties;(b) Unit cell orientation and the samples that were generated using it.

from Ref. [43]), the expected results are in fully agreement with the requirements imposed above. We note that one component of the mass density tensor slightly varies in the frequency range, while the other is virtually constant.

2.3 Measurement Results

After the two designed samples were fabricated, they were placed in the 1D acoustic waveguide and the reflection and transmission coefficients were measured for frequencies ranging from 500 Hz to 3 kHz (we performed measurements every 100 Hz). At each frequency, the central frequency of the pulse sent to the speaker is the same as the frequency of interest (e.g. at 3 kHz, $f_0=3$ kHz in equation 2.10). There are some limitations over the frequency range that can be explored, imposed by the experimental setup: below 500 Hz, the incident and the reflected signals will start to overlap and above 3 kHz the higher propagating modes will occur.

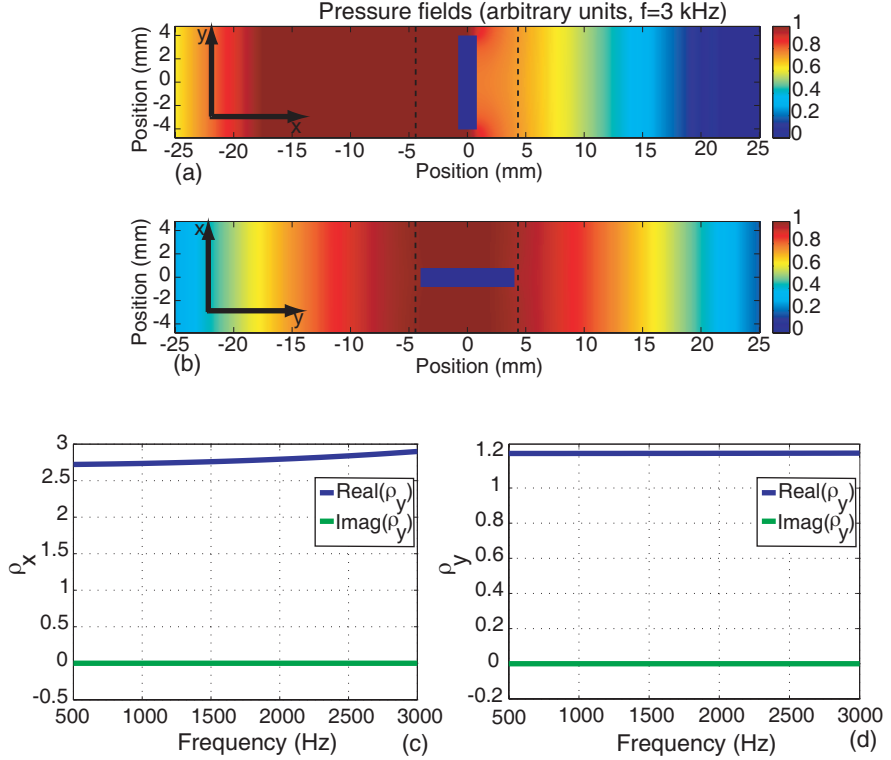


FIGURE 2.5: (a) Simulations for acoustic plane wave propagation in the x direction ($f = 3$ kHz);(b) Simulations for acoustic plane wave propagation in the y direction ($f = 3$ kHz); (c) Broadband effective mass density in the x direction; (d) Broadband effective mass density in the y direction.

The reflection and transmission coefficients are computed using a time domain technique that is exemplified in Fig. 2.6 (adapted from Ref. [43]). At every frequency, we performed 3 sets of measurements and an example of the *Matlab*[®] code used to perform the measurements is presented in Appendix A. Therefore, we measured the signals at the two microphones for the actual sample, for the empty waveguide and for a solid, thick disc instead of the sample. The last two sets of measurements will be used as reference for the perfect transmission and reflection, respectively.

The three sets of signals collected at the first microphone are aligned with respect to one of them (Fig. 2.6 (a)) because differences in time processing of the PC could lead to errors (i.e. the incident signal measured by the first microphone should be at

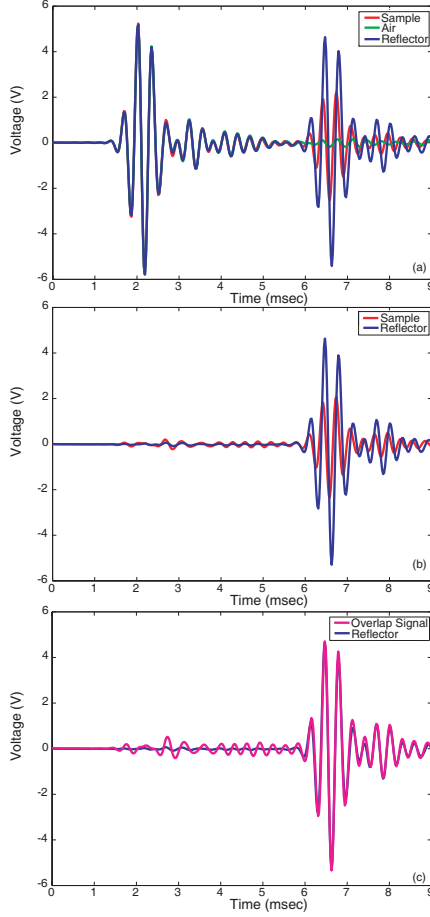


FIGURE 2.6: Example of signals used to determine the reflection and transmission coefficients: (a) Initial signals collected at Channel 1 with sample, air and perfect reflector (incident signal and first reflection, aligned); (b) Isolated first reflection; (c) Reflected signal from the sample modified in amplitude and phase to overlap over the signal from perfect reflector.

the same moment in time for all measurements). Then, the signals recorded by the second microphone are moved with the same time shift (i.e. the signals should be recorded at the same time for the two channels). The next step will be to isolate the signal reflected by the sample under test (s_1 , Sample), Fig. 2.6 (b) (subtract from the signal measured with the sample under test the signal measured with empty waveguide). We compare this signal to the similar signal produced by the perfect reflector (s_2 , Reflector) and determine the delay, phase, and amplitude change needed

by s_1 in order to overlap it over s_2 . In order to perform this complex scaling, we use the translation and scaling properties of s_1 and s_2 Fourier transforms (e.g. Fig. 2.6 (c)):

$$\text{If } h(x) = f(x - x_0), \text{ then } \hat{h}(\omega) = e^{-2\pi i x_0 \omega} \hat{f}(\omega) \quad (2.11)$$

$$\text{If } h(x) = f(ax), \text{ then } \hat{h}(\omega) = \frac{1}{|a|} \hat{f}\left(\frac{\omega}{a}\right) \quad (2.12)$$

where $h(x)$ and $f(x)$ are integrable functions and the hat symbol denotes their Fourier transform; ω is the frequency and a and x_0 are real numbers.

The corrections are iteratively determined such that the error between two iterations is minimized. The phase and amplitude corrections represent, from definition, the phase and amplitude of the reflection coefficient. Similarly, the transmission coefficient is computed comparing the incident portion of the signals transmitted to the second microphone for the measurements performed with no empty waveguide and with sample under test, respectively.

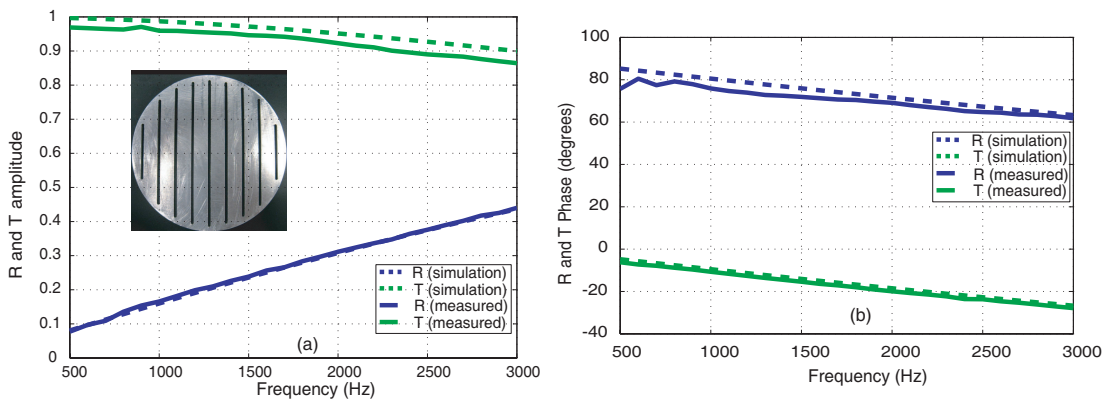


FIGURE 2.7: Propagation in the x direction. Reflection and transmission coefficients amplitude (a) and phase (b).

The results for the propagation in x direction are summarized in Fig. 2.7 (adapted

from Ref. [43]), which shows the measured reflection and transmission coefficients (amplitude (a) and phase (b)) compared with expected results produced by simulations. This sample corresponds to the sample in the middle in Fig. 2.4 (b). As can be seen, an excellent agreement between the simulations and the measured reflection and transmission coefficients, both amplitude and phase, is observed. We should note that the transmission coefficient is approximately 3% lower than the expected value across the entire frequency range. We believe that this deviation from the expected results is caused by pressure leakage around the sample in the system and that the measurements could be perhaps improved if we will use a better holding system for the sample holder. This will ensure a better sealing of the joints between samples and tubes.

We performed the same set of measurements for the second sample (the pressure plane wave propagating in the y direction) and the results are presented in Fig. 2.8 (adapted from Ref. [43]). This sample corresponds to the one in the right side of Fig. 2.4 (b). Again, an excellent agreement between simulations and measurements is obtained for the amplitude and phase of both coefficients. As it was the case for the previous sample, the measured transmission coefficient is a few percent smaller than the predicted values from numerical simulations.

Unlike the first sample, the measured phase of the reflection coefficient starts to diverge from the simulation for frequencies below 1.5 kHz. This behavior is because:

- a) the sample is acoustically thin at low frequencies; in consequence, the reflected signal is very weak and our time domain processing technique does not allow reliable processing of the phase information when the signal to noise ratio is small.
- b) the size of the inclusion is small; for the first sample the inclusion size is also small compared with the wavelength at low frequencies but this dimension is

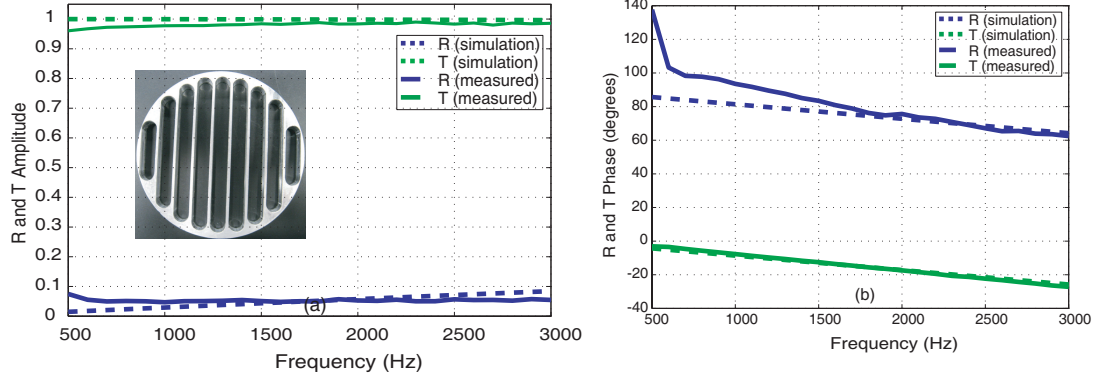


FIGURE 2.8: Propagation in the y direction. Reflection and transmission coefficients amplitude (a) and phase (b).

5 times larger than for the second sample. In consequence, the reflected signal is about 5 times larger (e.g. 0.09 compared with 0.02 at 500 Hz), which gives a higher signal-to-noise ratio for the first sample compared with the second sample.

- c) as the frequency decreases the pulse corresponding to the first reflection partly overlaps with the incident pulse and subsequent reflections because the microphones are on a fixed position on the tube.

After we measured the transmission and reflection coefficients, the effective mass density and bulk modulus in both directions, x and y were computed using the procedure described in the first section of the current chapter [42]. These measured effective parameters along with the expected values from the simulations are shown in Fig. 2.9 and Fig. 2.10.

In general, the measured effective material parameters have values close to the expected results over the entire bandwidth analyzed (500 Hz to 3 kHz). We should note that:

- a) the effective mass densities resulted from measurements are nearly invariant

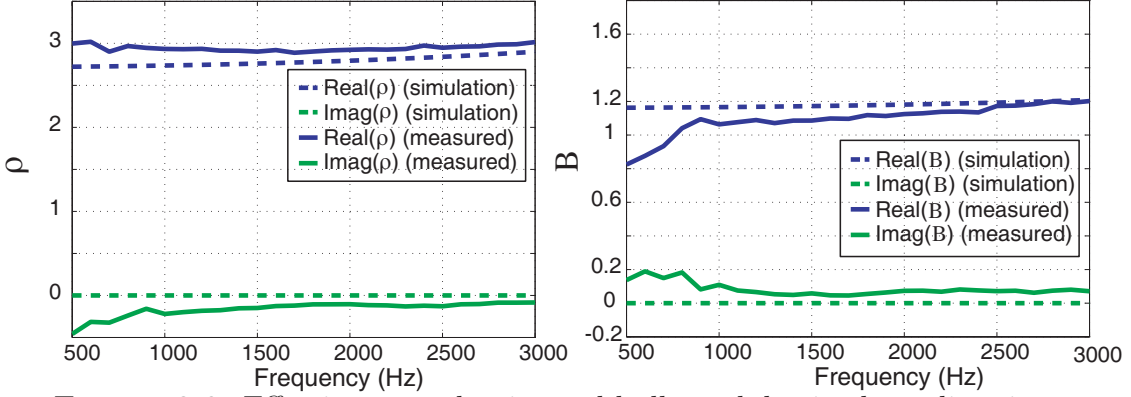


FIGURE 2.9: Effective mass density and bulk modulus in the x direction.

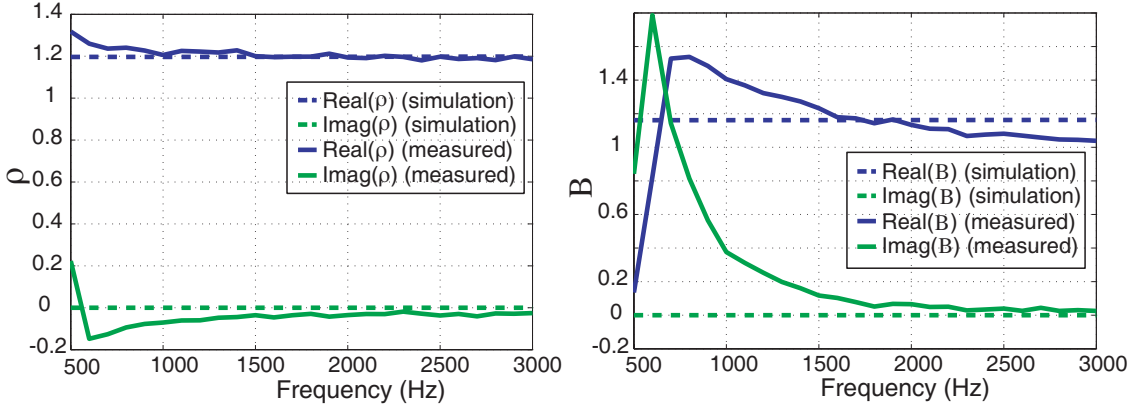


FIGURE 2.10: Effective mass density and bulk modulus in the y direction.

with frequency and the mass anisotropy ratio varies from 2.28 to 2.54 from 500 to 3000 Hz, which is extremely close to the designed value;

- b) the relative mass density exceeds one in both directions because the Al inclusions have a density greater than air, the surrounding background.

These two observations are very valuable, as we will see in the following chapters. The effective bulk modulus is about 1.2, relative to the air bulk modulus in both directions of propagation. It is constant and close to the expected values from numerical simulations for almost the entire frequency band analyzed. However, for the second sample, the small reflection magnitudes produce significant errors in the

bulk modulus for frequencies below 1.5 kHz.

As can be seen from the equations that give the bulk modulus (2.6,2.7,2.9):

$$\lim_{R \rightarrow 0; T \rightarrow 1} \frac{\partial B}{\partial R} = \infty \quad (2.13)$$

This means that for this particular case when the reflection coefficient is extremely small, low variations of the measured reflection coefficient R compared with the expected value will produce high dissimilarities between the measured bulk modulus and the predicted one.

2.4 Perforated Plates Designed as Acoustic Metamaterials

As we have already seen in the previous section, this numerical technique to design acoustic metamaterials has numerous advantages: it is relatively easy to use and is able to produce broadband acoustic metamaterials with material parameters precisely controlled. However, for some applications, the fabrication of these materials could be challenging. For example, for the previous design, the effective mass density is increasing as the gap between consecutive unit cells is decreasing. Therefore, if large values in one direction and small values in the other direction for mass density are needed, the solid inclusions will be extremely thin and close to each other. This is hard to experimentally realize since thin and tall (in order to fill the waveguide in the invariant direction) plates will require strong materials in which machining small, uniform gaps is hard. One way to overcome this problem will be to invert the solid and air from the previous design, that is to have a solid unit cell with a rectangular hole. Since rectangular holes with different dimensions are also hard to be experimentally created, we could replace it with a circular hole. Another way, presented in detail in Ref. [44], could be to search for a different, optimal shape of the solid inclusion that will lead to the desired effective mass density and bulk mod-

ulus. The quest for the best solid inclusion is performed in this case using relatively random shapes and a genetic algorithm that selects the best candidates.

In the case studied here, a unit cell is composed of a solid material with a circular hole in the middle. Since we are considering air as background, almost any solid will have a large impedance contrast with it. For this unit cell, the mass density in one direction will be controlled by the hole dimension (radius) and in the other direction by the plate thickness. The effective bulk modulus will be controlled again by the solid over air volume ratio, similarly with the previous unit cell. Several simulations were performed in order to confirm that while the unit cell has the y orientation, the effective material parameters are dictated only by the slab thickness and are minimally influenced by the hole radius. The *COMSOL®* Multiphysics - Acoustics Module simulations for this type of unit cell are presented in Fig. 2.11 for x orientation and Fig. 2.12 for y orientation, respectively.

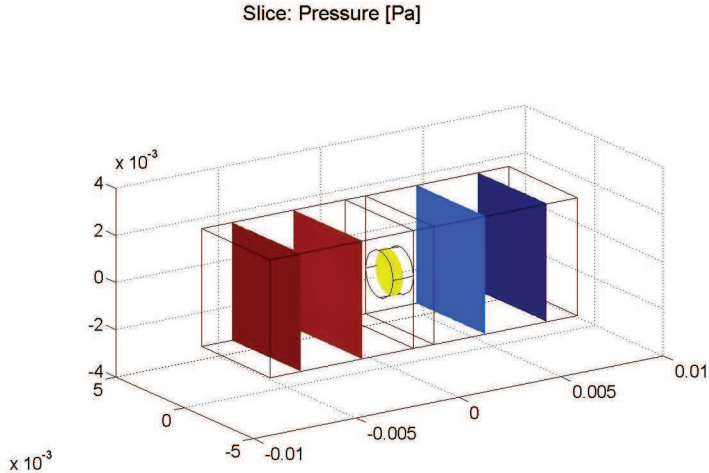


FIGURE 2.11: Perforated plate unit cell used to analyze the effective density and bulk modulus: x orientation.

The goal of this unit cell is to optimize the unit cell dimensions such that it will be easy to obtain specific material parameters. More specifically, for a 2D acoustic

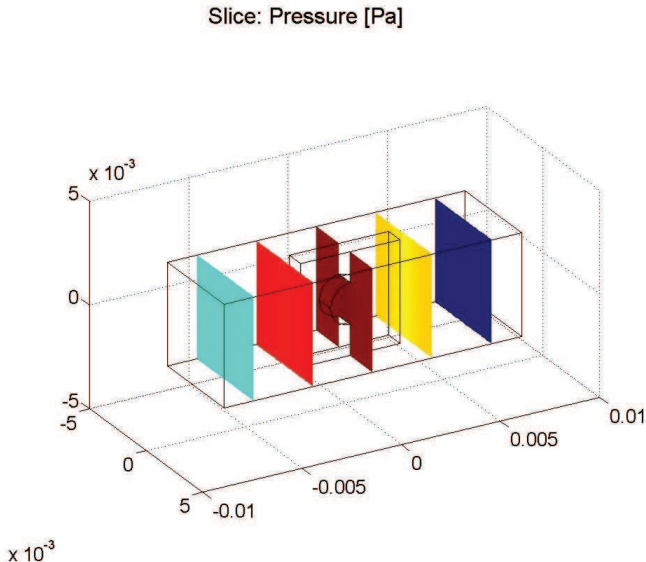


FIGURE 2.12: Perforated plate unit cell used to analyze the effective density and bulk modulus: y orientation.

ground cloak in air, the desired effective mass densities (relative to the the air density) will be 5.7 and 1.1 while the effective bulk modulus will be 1.25. A cube unit cell with 5 mm edge that has inside a 1 mm thick plate with a 0.8 mm perforation in the middle will have 5.6 and 1.23 effective mass densities and 1.22 effective bulk modulus. The perforated plate with these dimensions is relatively easy to fabricate and was successfully used to experimentally demonstrate the realization of a 2D broadband acoustic ground cloak in air (see Ref. [45] for a detailed presentation of the design methodology and the experimental implementation).

2.5 Transmission Loss Measurements for Perforated Plates

When designing an ideal 2D ground cloak in air, the following problem occurs [45]: one component of the mass density tensor should be smaller than the mass density of the background and also the bulk modulus should be less than it is for air. Since it is impossible to find such a material, we could solve this problem by considering as

background a material that has slightly higher material parameters than air. In this case, all the material parameters of the cloak will go to the desired values previously specified (see Chapter 4 for a complete description of the method used to scale up the effective material parameters). However, the price paid is a slight mismatch between the impedance of the cloaked region and the air background, which leads to a great but not ideal cloaking performance.

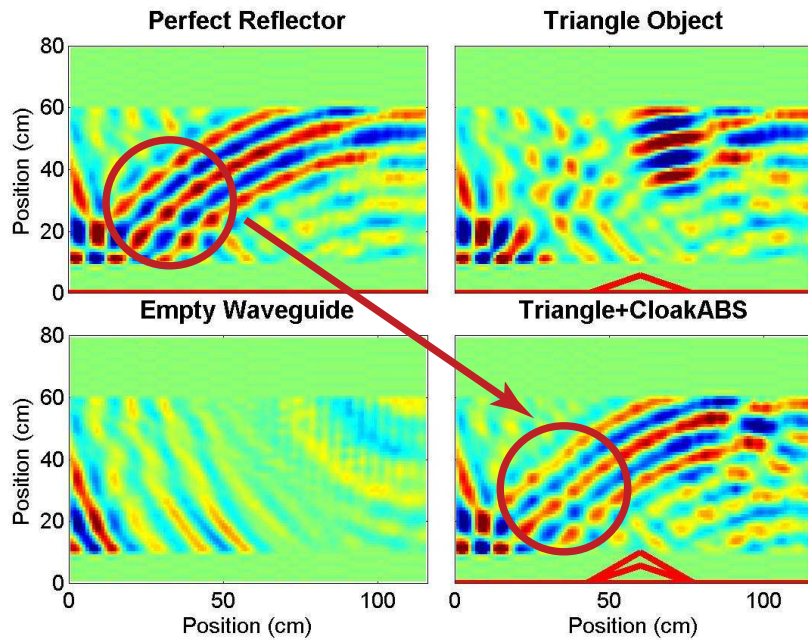


FIGURE 2.13: Measured pressure field for ground (top left), empty waveguide (bottom left), ground and object to hide (top right) and the cloaked object plus the ground (bottom right).

In Fig. 2.13 we show the measurements performed in a 2D acoustic waveguide for the pressure fields in four cases: ground present in the waveguide (top left), empty waveguide (bottom left), ground and object to hide present in the waveguide (top right) and the cloaked object plus the ground placed inside the parallel plate waveguide (bottom right). In the ideal case, a perfectly cloaked object will produce no difference between the measurements with the ground only and the measurements

with the cloaked object placed on top of the ground. However, due to the impedance mismatch between the cloak and the air background there is a modest difference, highlighted in the red circle of the bottom right snapshot, which shows a slight attenuation in the wavefront. Also, in numerous applications the microperforated panels (MPP) are used as sound absorbers and have been widely investigated over the last several decades (see for example one of the most representative papers, Ref. [46] or Refs. [47, 48, 49, 50, 51, 52]). Here, we aim to show that the material used for the 2D ground cloak is not an absorber and therefore has a modest, quantifiable transmission loss at the operating frequencies.

In order to perform measurements for transmission loss, we use a commercial impedance tube measurement system provided by *BSWA Technology Co., Ltd.* The actual system, without the microphones and the data acquisition hardware, as well as the schematic diagram are presented in Fig. 2.14.

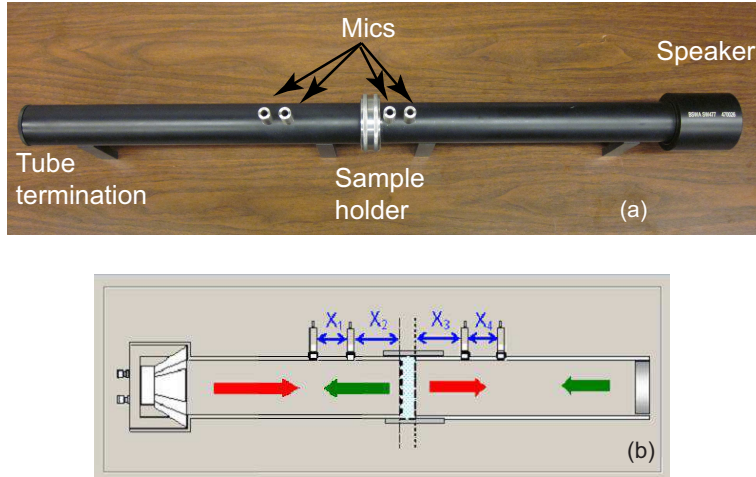


FIGURE 2.14: BSWA Impedance tube system: (a) actual system; (b) schematic diagram.

The measurement technique is described in the ASTM standard E2611-09 [53]: a sound source is generating a random noise with uniform spectral density in the frequency range of interest and the pressure field is measured at four fixed locations.

The position of the microphones is chosen such that the spacing is less than the smallest half wavelength. Also, the tube diameter is selected to ensure no propagation of higher order modes. In order to determine all four components of the transfer matrix, two independent measurements should be performed: one for the tube ended with a rigid cap and one for the tube open (i.e. no cap at the end). The reference for the transfer functions is the microphone 1 (according to the standard, it could also be a different location or the signal used to excite the speaker).

The pressure field at the four microphones could be expressed as (the time-dependent term is not shown) [53]:

$$P_1 = A e^{-j k x_1} + B e^{+j k x_1} \quad (2.14)$$

$$P_2 = A e^{-j k x_2} + B e^{+j k x_2} \quad (2.15)$$

$$P_3 = C e^{-j k x_3} + D e^{+j k x_3} \quad (2.16)$$

$$P_4 = C e^{-j k x_2} + D e^{+j k x_2} \quad (2.17)$$

where k is the wavenumber in air. A, B, C, D are amplitude constants used for the wave field decomposition into forward and backward traveling waves. These constants could be computed using the following relations:

$$A = j \frac{P_1 e^{j k x_2} - P_2 e^{j k x_1}}{2 \sin(k s_1)} \quad (2.18)$$

$$B = j \frac{P_2 e^{-j k x_1} - P_2 e^{-j k x_2}}{2 \sin(k s_1)} \quad (2.19)$$

$$C = j \frac{P_3 e^{j k x_4} - P_4 e^{j k x_3}}{2 \sin(k s_2)} \quad (2.20)$$

$$D = j \frac{P_2 e^{-j k x_3} - P_2 e^{-j k x_4}}{2 \sin(k s_2)} \quad (2.21)$$

where s_1 and s_2 are the distances between the microphones 1 and 2 and microphones 3 and 4, respectively.

These constants are then used to compute the pressure and particle velocity on both sides of the specimen, for each tube termination:

$$P_0 = A + B \quad (2.22)$$

$$P_d = C e^{-j k d} + D e^{j k d} \quad (2.23)$$

$$v_0 = \frac{A - B}{\rho c} \quad (2.24)$$

$$v_d = \frac{C e^{-j k d} - D e^{j k d}}{\rho c} \quad (2.25)$$

where ρ is the air density and c is the speed of sound in air.

Finally, the components of the transfer matrix function could be determined from the following equation:

$$\begin{pmatrix} P_0^{(a)} & P_0^{(b)} \\ v_0^{(a)} & v_0^{(b)} \end{pmatrix} = \begin{pmatrix} T_{11} & T_{12} \\ T_{21} & T_{22} \end{pmatrix} = \begin{pmatrix} P_d^{(a)} & P_d^{(b)} \\ v_d^{(a)} & v_d^{(b)} \end{pmatrix} \quad (2.26)$$

where a and b superscripts denotes the measurements for the two distinct terminations of the tube.

The transmission loss is then calculated as:

$$t = \frac{2e^{jkd}}{T_{11} + (T_{12}/\rho c) + \rho c T_{21} + T_{22}} \quad (2.27)$$

$$TL = 20 \log_{10} \left| \frac{1}{t} \right| \quad (2.28)$$

where t is the transmission coefficient and TL is the transmission loss expressed in decibels. The same relation 2.28 will be used also in the numerical simulations. As it was the case for the previous unit cell, a numerical simulation is performed in *COMSOL®* Multiphysics - Acoustics Module and the reflection and transmission coefficients are computed for the entire frequency range of interest. Then, the equation 2.28 is used to compute the transmission loss.

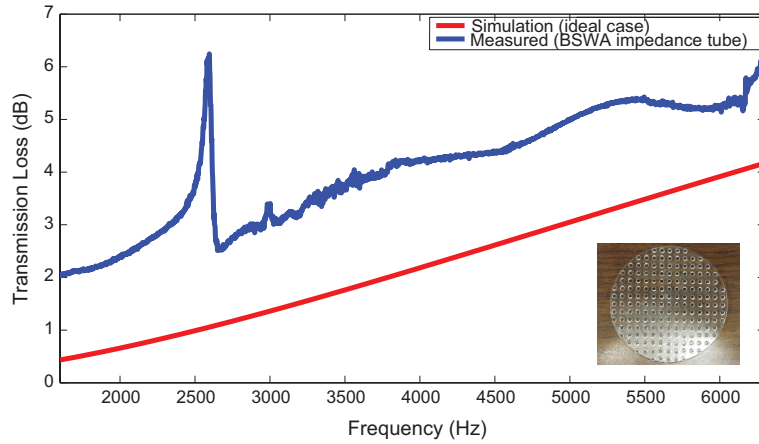


FIGURE 2.15: Transmission loss for one unit cell, measured and simulated for the ideal case.

In the Fig. 2.15, the results of the measurement and simulation of transmission loss are presented. For both cases, only one unit cell in the propagation direction has been used and for the measured transmission loss, the diameter of the tube was filled with unit cells (i.e. the sample has only one unit cell in the propagation

direction and numerous unit cells in the other two, invariant directions). There is a clear difference between the measured transmission loss and the expected values, which are smaller. This is due to the fact that the losses in the actual unit cell are not taken into consideration. However, if we model the unit cell like a continuous domain with the actual mass density and bulk modulus of the perforated plate and add losses as an imaginary part for the bulk modulus (see Ref. [45] for details), we obtain an almost perfect agreement between the simulation and the measurements, as can be seen in Fig. 2.16.

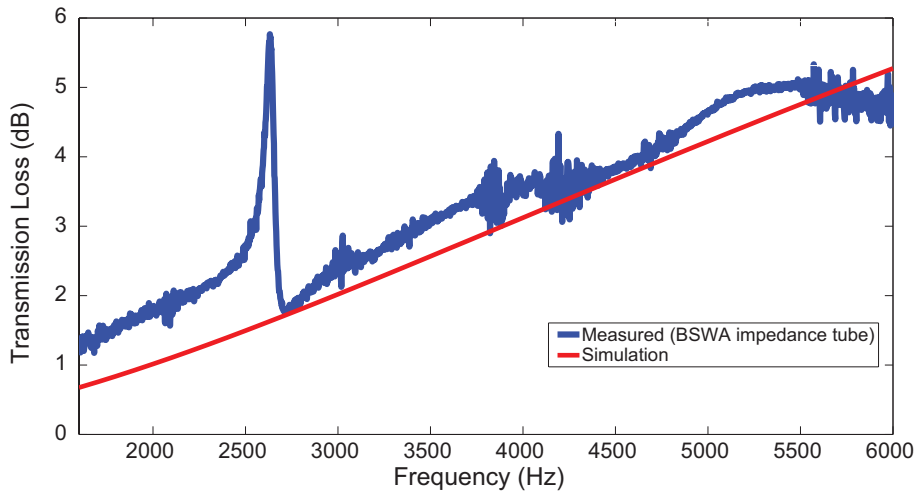


FIGURE 2.16: Transmission loss for one unit cell, measured and simulated for the non-ideal case.

Not only we obtain a better match simulation-measurements for this case, but can also observe the relatively modest transmission loss values around the design frequency, 3 kHz. According to the sound transmission class (STC) ratings (which is equal to the transmission loss in dB), any STC smaller than 30 is considered modest insulation. For example, the normal speech can be easily heard and understood.

- STC 25: normal speech can be understood
- STC 30: loud speech can be understood

- STC 35: loud speech audible but not intelligible
- STC 40: onset of "privacy"
- STC 42: loud speech barely audible
- STC 45: loud speech not audible for most people

We should mention that the procedure to assign STC ratings is specified in Ref. [54] and it was used just for comparison at some frequencies. Therefore, no STC rating was assigned to our acoustic metamaterial.

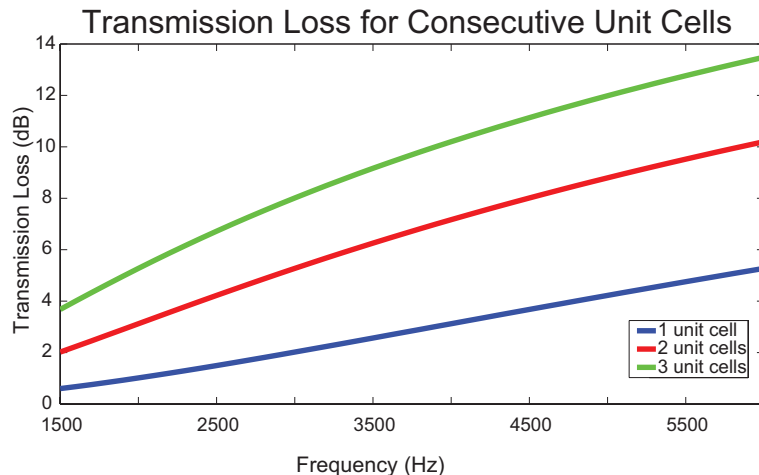


FIGURE 2.17: Transmission loss for more than one unit cell in the propagation direction, non-ideal case.

A different study aimed to investigate the behavior of more than one unit cell in the direction of propagation. Based on the previous excellent agreement with the measurements and due to the fact that it is hard to place more consecutive cells in the impedance tube without any extra holder which will affect the measured values of the transmission loss, we decided to only numerically investigate how the multicell setup affects the overall transmission loss (Fig. 2.17). As expected, the transmission

loss is increasing as the thickness of the material is increasing. However, the overall reduction in sound transmitted through more consecutive unit cells can still be quantified as modest, even for as many as eight unit cells (the maximum number of consecutive unit cells in the 2D acoustic ground cloak design [45]). Numerical simulations, not shown here, report a transmission loss of around 16 dB at a frequency of 3 kHz.

2.6 Conclusions

The work summarized in this chapter confirms that the technique described in Ref. [37] could be implemented in practice. It is a simple method which allows one to design strongly anisotropic and broadband acoustic metamaterials. The experimental implementation of this technique was demonstrated by designing very simple, broadband metamaterials with effective mass density anisotropy. The metamaterials consist in solid inclusions of different shapes, placed in air. We measured the reflection and transmission coefficients and then inverted them in order to get the effective material parameters of the unit cell.

In Ref [37], the simulation results demonstrate that as few as one cell in the propagation direction is sufficient to calculate the effective material parameters. Although measurements for more than one unit cell in the propagation direction would be more supportive for this statement, this kind of measurements raised several hardware setup complications regarding the mechanisms that will hold the samples perfectly aligned and will prevent pressure leakages between samples and tubes and between samples and small tube fragments that will be placed between consecutive samples. Multicell measurements could be illustrative, but are not needed. The conclusions presented here are valid, as we will see in the following chapters.

3

Broadband 2D Gradient Index Acoustic Lens

A medium in which the index of refraction or sound speed varies is called gradient index medium (GRIN). This kind of media is often present in nature. For example, the human eye or earth's atmosphere have an index of refraction which varies from point to point. The ways to have materials with varying index of refraction and to proper use them in practical applications have been intensively explored for optical frequencies since 1970s [55]. As we have seen in the previous chapters, the advances in acoustic metamaterials have made the implementation of a desired variation for index of refraction easier and more precise. For example, a periodic structure formed using solid cylinders placed in air or water background is a homogeneous medium, with specific effective parameters that could be analytically determined and that are controlled by the filing ratio [22, 23, 24].

For optical frequencies, it has been shown that there are three fundamental ways in which the index of refraction can vary: along the optical axis (*axial gradient*), transverse on the optical axis (*transverse gradient*) and symmetric around a point (*spherical gradient*) [55]. Also, it has been shown that for optical frequencies and for transverse gradient, if the gradient has a quadratic variation in a direction perpendic-

ular on the propagation direction then the medium presents the *self-focus* property. This property have been confirmed for acoustic media also. The way the index of refraction varies is controlled using periodic structures arranged in a lattice. For simple lattices (e.g. solid cylinders placed in a fluid background), analytical expressions between the effective material parameters and the filling ratio (or the lattice parameter) could be determined [56]. The practical implementation of this approach, with the background fluid being air or water, have been recently presented in the literature [57, 58].

We should note that there is at least one other way to focus the acoustic waves: through negative refractive index [59]. For this method, as we mentioned in the introductory chapter, the negative material parameters are obtained using a resonant mechanisms which leads to a small operating frequency range. Another drawback of this technique is that the lattice parameter should be comparable with the wavelength which produces extremely large lenses at low frequencies.

In this chapter we present our implementation of the gradient index lens. The unit cells are designed using the method theoretically and experimentally described in the previous chapter [37, 43]. Our final product has a higher refractive index, lighter weight, and better impedance matching than the only previous gradient acoustic lens in air demonstrated experimentally [57].

3.1 Design of the Index of Refraction Profile

According to Snell's law, the optical or acoustic rays follow a curved trajectory inside the GRIN media, being bended towards the higher index of refraction (Fig. 3.1 (a), adapted from [60]). For transverse gradient, a good choice for the profile of index of refraction would be the hyperbolic secant (Fig. 3.1 (b), adapted from [60]). Unlike the parabolic profile, this type of variation for the index of refraction n could focus the optical or acoustic waves with no aberration [55, 24]. The transverse gradient

along y axis could be written as:

$$n(y) = n_0 \operatorname{sech}(\alpha y) \quad (3.1)$$

where n_0 is the index of refraction for $y = 0$ and α is called *gradient parameter*. It is defined by the following relation:

$$\alpha = \frac{1}{h} \cosh^{-1} \left(\frac{n_0}{n_h} \right) \quad (3.2)$$

where h is half-width of the lens and n_h is the index of refraction at the edge of the lens (or, the index of refraction for the surrounding background, air in our case).

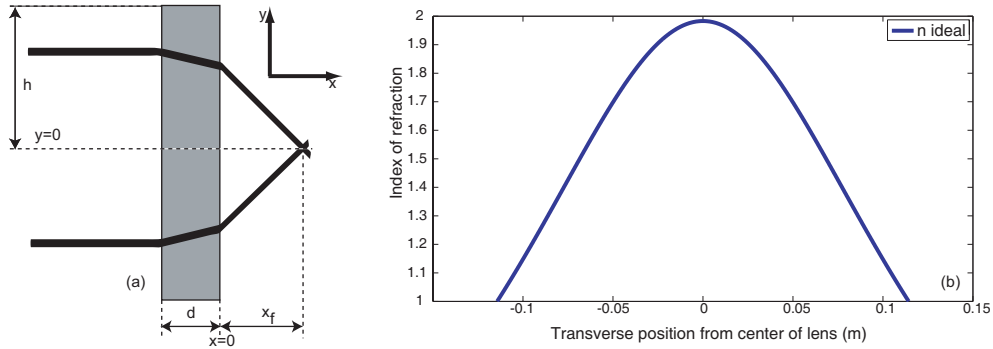


FIGURE 3.1: (a) GRIN lens and its orientation; (b) Desired index of refraction along the direction transverse to propagation direction.

Using the ray theory, the beam trajectory inside the GRIN medium could be described by the following relations [55]:

$$y(x) = \frac{1}{\alpha} \sinh^{-1} [u_0 H_f(x) + u_0 H_a(x)] \quad (3.3)$$

where u is a transformation of the Cartesian coordinate y into a hyperbolic coordinate:

$$u_0 = \sinh(\alpha y_0), y_0 = y|_{x=0} \quad (3.4)$$

$$\dot{u}_0 = \frac{\partial u_0}{\partial y} \quad (3.5)$$

The above equation represents the incident angle, 0^0 in our case.

$$H_a(x) = \frac{\alpha x}{\alpha} \quad , \quad H_f(x) = \cos(\alpha x) \quad (3.6)$$

$$\dot{H}_a = \cos(\alpha x) \quad , \quad \dot{H}_f = -\alpha \sin(\alpha x) \quad (3.7)$$

The last two equations describe the position and the slope of the axial and field rays. The focal distance could be written then as:

$$x_f = -\frac{y(d)}{\dot{y}(d)} \sqrt{\frac{1 - [\dot{y}(d)]^2 \{n^2 [y(d)] - 1\}}{n^2 [y(d)]}} \quad (3.8)$$

where

$$\dot{y}(d) = \frac{u_0 \dot{H}_f(x) + \dot{u}_0 \dot{H}_a(x)}{\alpha \cosh \{\sinh^{-1} [u_0 H_f(x) + \dot{u}_0 H_a(x)]\}} \quad (3.9)$$

The relation (3.8) is important because, as we will see later, tells us if the designed lens could be characterized using our apparatus and what decrease in thickness we will get if we increase the maximum value for the index of refraction, for the same focal length.

Our goal is to have an index profile that will ensure focusing and to implement it using subwavelength unit cells. The final product should be easier to implement and measure in our experiment setup. Also, we wanted to have broadband lens, with a maximum value for n as high as possible such that the thickness of the lens will be the smallest possible.

We decided that the background fluid will be air and the operating (design) frequency will be 3 kHz (11.43 cm wavelength). Due to the constraints explained above, the lens will be 2.0 wavelengths wide in the transverse direction and 0.31 wavelengths long in the propagation direction. The position of the focal point along the acoustic axis predicted by equation 3.8 is 10.13 cm (see Fig. 3.1 (a)). For the parameter range of our lens and that described in Ref. [57], we find that our n_{\max} of 2 yields a lens that is approximately 2.5 times thinner than previous designs [57].

In order to have a matrix of unit cells that behaves like an isotropic acoustic metamaterial, we decided to have a unit cell dimension approximately 10 times smaller than the operating wavelength. Because of the isotropic requirement for the unit cell and based on our previous experience described in Chapter 2, we started with a unit cell formed from a solid rectangular inclusion in air background (Fig. 3.2 (a)).

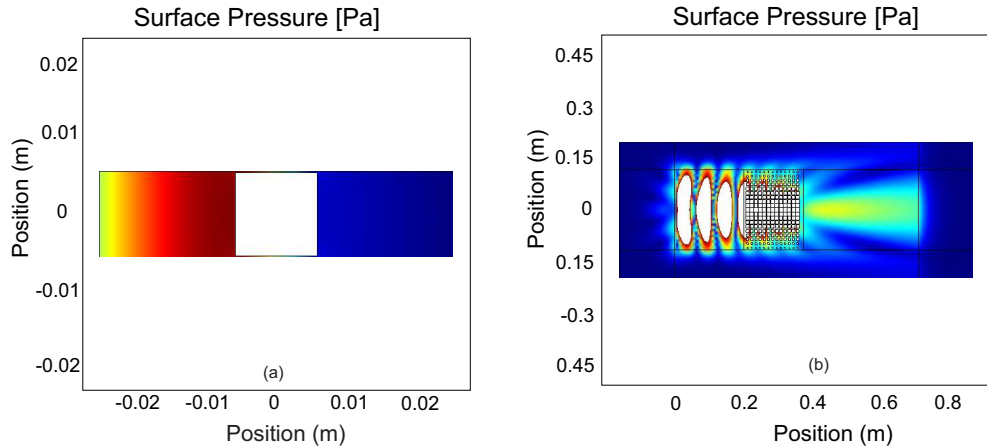


FIGURE 3.2: (a) Unit cell with square solid inclusion (first attempt); (b) Actual lens simulation for unit cells made with square rods commercially available.

To achieve the desired index of refraction profile, we varied the dimension of the square and computed the effective unit cell parameters, index of refraction and impedance (i.e. we used the same procedure described in the previous chapter: sent a plane wave normally incident on the unit cell, computed the reflection and trans-

mission coefficients and then inverted them in order to obtain n and Z). Although this design clearly showed the focusing effect, the focal point and the diffraction lobes, the unit cells in the middle had a great impedance mismatch relative to the background. Therefore, a new design was needed.

For a unit cell consisting in a solid inclusion in a fluid background, the index of refraction is controlled by the size of the gaps between consecutive solid inclusions and the bulk modulus is controlled by the volume fraction of the solid relative to the background [37, 61, 23]. Our goal will be then to keep small gaps and thus high n , while keeping the total volume fraction of the solid to a minimum, thus keeping Z close to that of air. Because $Z=nB$ and n is already chosen as in Fig. 3.1, the unit cell impedance will be minimized if the bulk modulus of the unit cell is smallest possible. Consequently, we reduced the volume ratio of solid relative to air by cutting the square into a cross (Fig. 3.3 (a), adapted from [60]).

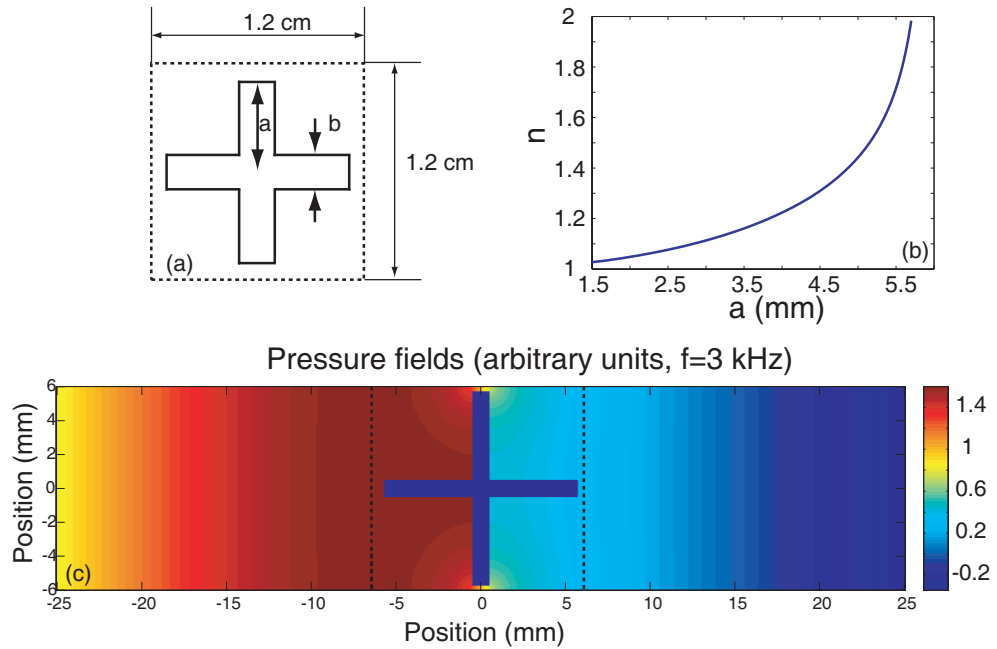


FIGURE 3.3: (a) Unit cell dimensions;(b) Index of refraction vs. a dimension of the cross;(c) Simulations for acoustic wave propagation ($f = 3$ kHz).

Therefore, we varied the dimensions a and b of the cross such that index of refraction will be like in Fig. 3.1 (b) and, in the same time we have the minimum mismatch between the impedance of air and the impedance of the unit cell, respectively. However, there is a specific way in which one can vary these dimensions. For example, the largest value of a (hence the smallest gap) cannot be larger than the value that we can actually realize in practice with our fabrication process (stereolithography). Also, the smallest value of b (hence the thinnest solid structure) cannot be smaller than a value that ensures that the final structure is stable and is not collapsing under its own weight.

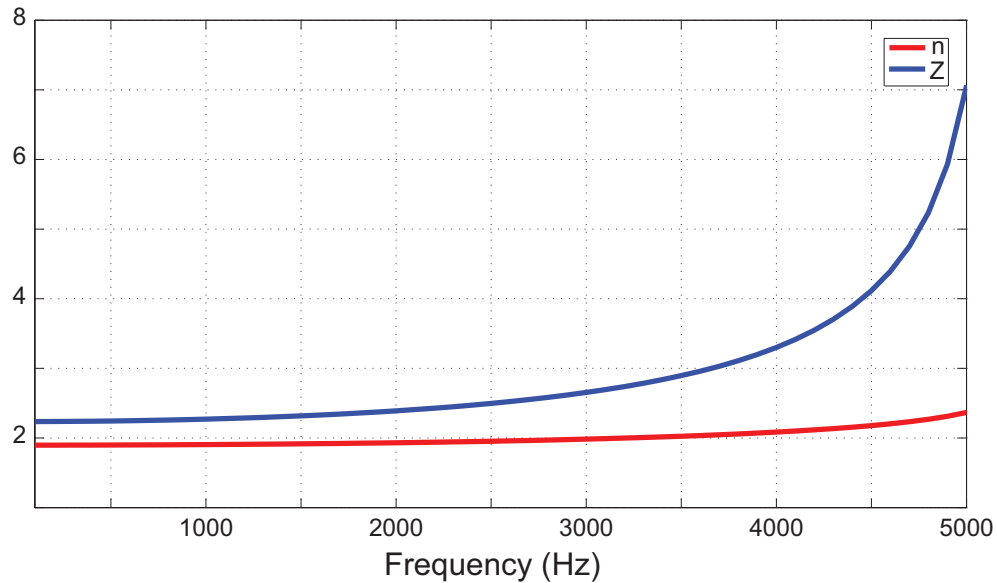


FIGURE 3.4: Frequency dependence of the material parameters for the largest cross unit cell.

The values that were confirmed to be realizable were a of 5.7 mm (or a 0.6 mm gap) and b of 1 mm. Consequently, we decided to keep $b=1$ mm fixed for all unit cells (i.e. to have the minimum impedance possible for the unit cell) and vary the dimension a in order to get the desired value for n (Fig. 3.3 (b), adapted from [60]). The maximum value for n is 1.98 and it is obtained for $a=5.7$ mm. Also,

since this unit cell with the largest solid inclusion is prone to the smallest operating frequency band, we ran a set of simulations to explore its frequency behavior. The results are shown in Fig. 3.4 and we can clearly observe that the index of refraction is relatively constant for up to 5 kHz and the price paid is an acceptable increase in the impedance mismatch.

We summarized in Fig. 3.5 (a) (adapted from [60]) the ideal profile for n in the transverse direction (only for positive values of y , the lens being symmetric with respect to its center) and the corresponding values of n for the unit cells (these values closely match the ideal values).

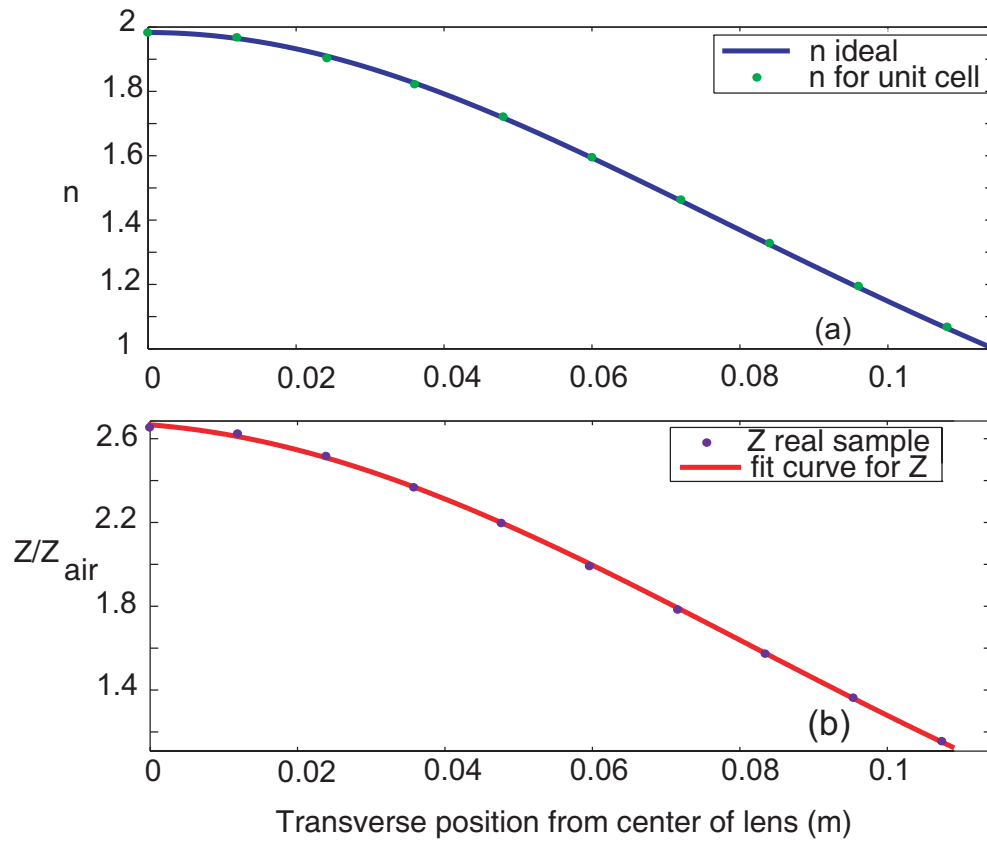


FIGURE 3.5: (a) Index of refraction along the direction transverse on the propagation direction (desired and realized in practice);(b) Unit cells impedance and their position on the axis perpendicular to propagation direction.

In Fig. 3.5 (b) (adapted from [60]) we show the effective impedance of the unit cells and the fit curve line, a line which shows how Z continuously varies along y axis. We should note that all the values presented in Fig. 3.5 (the *dots*) are obtained using the same method described in the previous chapter. Other methods to compute these results are presented in literature, for example see Ref. [62], but we preferred this technique because it is relatively simple and easy to implement for any kind of shape of the solid inclusion.

Few more remarks should be made about this design. First, both n and Z increase when a increases, so we had to choose the best compromise. However, for the n specified in Fig. 3.1, the impedance of the unit cell in the center of the lens is 2.6 times larger than that of the air, which still is approximately two times smaller than previous designs [23, 57]. Second, it has been theoretically shown that other inclusion shapes will produce a greater index of refraction without a large increase in the effective bulk modulus [37]. For example, see the Fig. 3.6 (a). In this case, for the same gap, we will obtain an index of refraction of 2.53 for $b=2.5$ mm (the impedance mismatch is 4). The best shape could be furthermore optimized using a genetic algorithm and imposing the fitness function to maximize the index of refraction, to minimize the impedance and to keep the effective material parameters relatively constant over the entire frequency range (in our case, 500 Hz - 4.5 kHz) [44]. However, for the purposes of our initial work (i.e. to show that the design technique presented in Chapter 2 could be used to create a GRIN lens), the crosses design was sufficient. Moreover, this design could be easily realized in practice without any major challenges.

In order to make sure that the array of unit cells will perform as a lens, we made two additional simulations using the Acoustic Module of *COMSOL®* Multiphysics: one for the actual lens and one where we replaced the lens with a continuous domain in which the index of refraction varies continuously as in Fig. 3.1 and the impedance

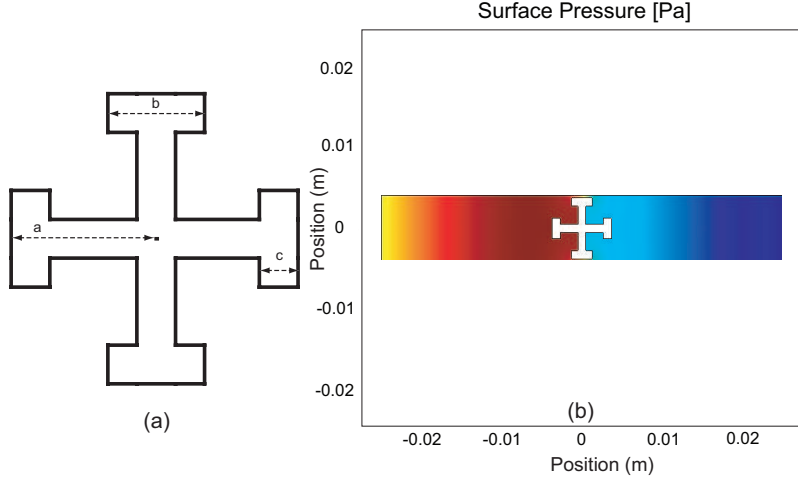


FIGURE 3.6: (a)Unit cell dimensions;(b)Simulations for acoustic wave propagation ($f = 3\text{kHz}$).

varies continuously as in Fig. 3.5 (b) (fit line). For the actual lens, we used in simulations the same material parameters that the actual crosses have in practice. The results are presented in Fig. 3.7 (adapted from [60]) and they clearly show that the acoustic metamaterial realization of the lens performs virtually exactly like the lens with idealized, smoothly inhomogeneous material properties.

3.2 Lens Characterization

After the lens design was finalized, the next step was to realize them in practice. In order to do this, the entire structure generated using a *Matlab*[®] code was exported in *Autocad*[®] where all the elements were extruded in the z direction to fill the entire waveguide. A thin, 1 mm plate was added at one end in the z direction in order to hold all the unit cells together and the entire structure was exported to a file format suitable to stereolithography technique. The lens were fabricated using *DSMSomos*[®] 9420 Photopolymer (density $\approx 1.13 \text{ g/cm}^3$ at room temperature, Poisson's ratio 0.43 and modulus of elasticity 553-850 MPa) and a finish that yielded the designed dimensions. A photograph of the lens (side and top view) as well

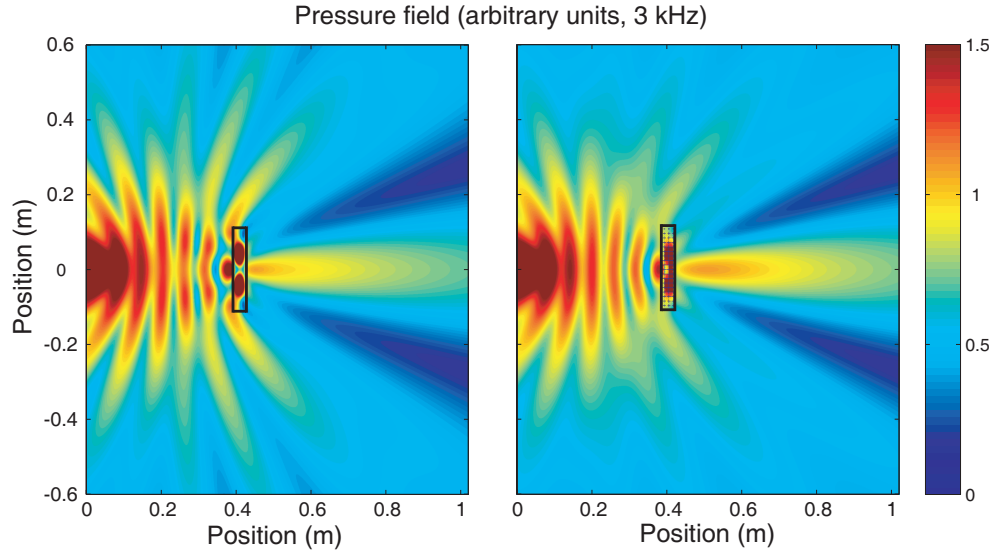


FIGURE 3.7: Comparison between simulated sound fields for an idealized lens with continuous material parameters (left) the actual structured lens (right).

as a photograph of the 2D waveguide where the measurements were performed are presented in Fig. 3.8.

In order to evaluate the lens we have made an in house 2D waveguide which consists in two 1.2 m^2 , 0.5 cm thick parallel, ABS plastic plates, placed at 5.08 cm one from each other. The separation distance between the parallel plates gives a cutoff frequency of 3.38 kHz. A regular PC speaker was used to generate a signal that travels through the waveguide. It is the same signal that was used in the previous chapter (see equation 2.10).

We collected the signals from two preamplified condenser microphones, which had the same type of amplifier as the one presented in Fig. 2.3. The first microphone was placed in a fixed position close to the speaker and was used as a time reference. The second microphone was moved inside the waveguide, using a stepper motor, and measured the pressure field inside the waveguide. We should mention that this setup does not allow measurements along the lines where the lens are placed or very close to the speaker. The measurement points were placed at every 2 cm in both directions,

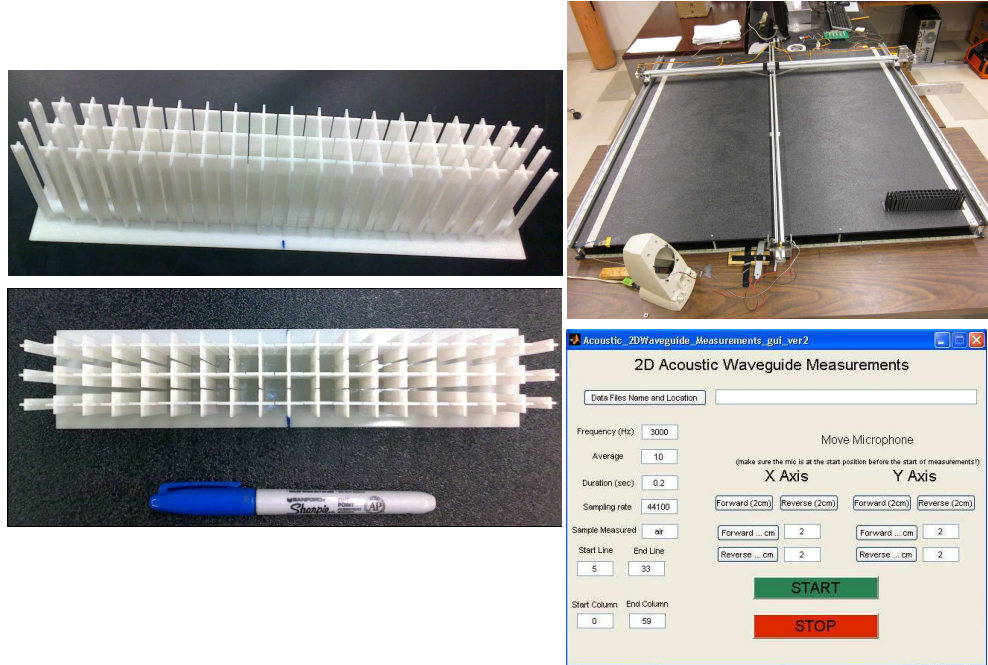


FIGURE 3.8: The actual lens, side and top view (left column) and the actual waveguide where the measurements are performed with the GUI that we created (right column).

x and *y*. As it was the case for the 1D waveguide, the signals were collected using the same National Instruments data acquisition card and signal to noise ratio was increased by doing several measurements and averaging them for each point.

The first set of measurements that we performed was at the design frequency (3 kHz). After we collected all the signals for each point, we align in time the signals collected by the microphone moving inside the waveguide using the reference signals from the microphone fixed on the waveguide. This step ensures a common phase reference for all the signals. Then, the incident and first reflection pulses are isolated from other reflections (e.g. reflections from the edges of the waveguide) and we use the Fourier transform to determine the amplitude and phase of this new signal. Although this procedure do not work very well for points that are extremely close to the edges of the waveguide (where the second reflection overlaps over the useful

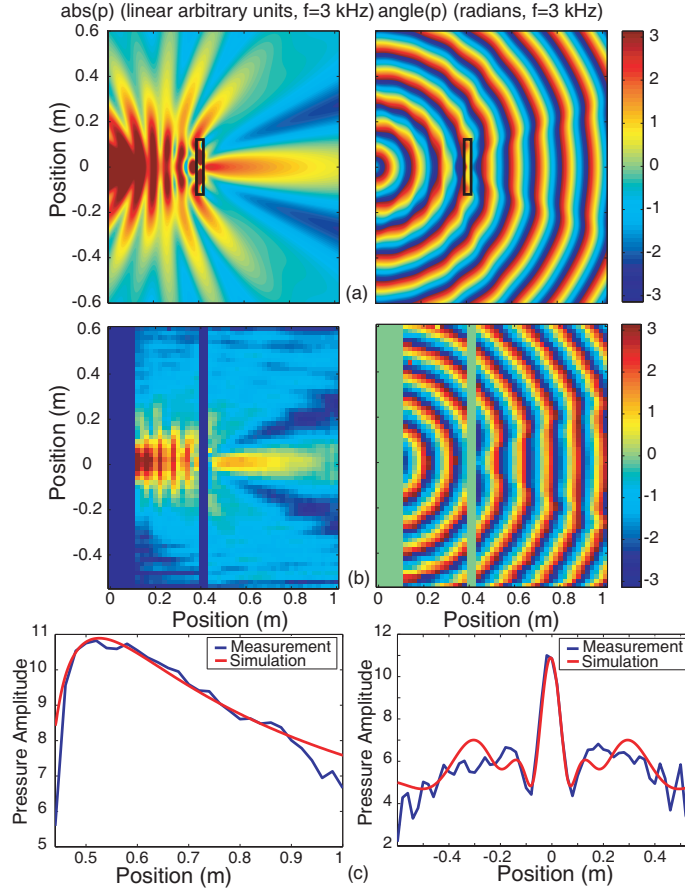


FIGURE 3.9: (a) Simulated pressure field amplitude (left) and phase (right) for continuous lens domain; (b) Measured pressure field amplitude (left) and phase (right); (c) Pressure amplitude (arbitrary units) on a line passing through the focal point in the propagation direction (left) and in a direction transverse on the propagation direction (right).

portion of the signal), the simulation and measurements are in good agreement for both, amplitude and phase of the total pressure field (see Fig. 3.9, adapted from [60]): the focusing effect and the focal distance are clearly distinguished. Moreover, the focal distance closely match the the value predicted by ray theory (≈ 10 cm). In order to furthermore emphasize the lens behavior of our structure, we extracted two relevant lines going through the focal point from Fig. 3.9 (a,b), one going in the propagation direction and one in a direction transverse on propagation direction and

we plotted the pressure profiles along these two lines (Fig. 3.9 (c)).

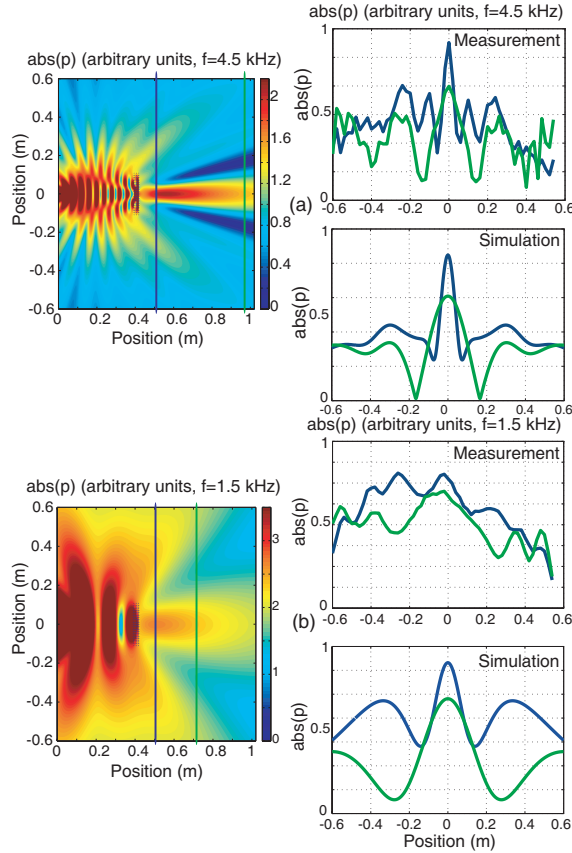


FIGURE 3.10: (a) Simulated pressure fields for the entire domain (left) and measured/simulated pressure amplitude slices through focal point and far away from the focal point at 4.5 kHz (right);(b) Simulated pressure fields for the entire domain (left) and measured/simulated pressure amplitude slices through focal point and far away from the focal point at 1.5 kHz (right).

A second set of measurements was performed to highlight the broadband properties of our lens. These measurements were slightly different, meaning that instead of measuring all the points inside the waveguide, we performed simulations for the entire domain and extracted two relevant lines perpendicular on the propagation direction: one going through the focal point and one far away after the focal point (see Fig. 3.10 (left column), adapted from [60]). The main motivation of this procedure was to highlight the pressure field maximums and minimums and to reduce the ex-

periment duration. We performed measurements for these lines and observed again a good agreement with the simulation results (Fig. 3.10 (right column), adapted from [60]). We should note that the broadband property of our lens could be explored with some limitations. First, when decreasing the frequency from 3 kHz, the dimension of the lens in the y direction will become smaller compared with the wavelength and the focusing property will diminish. Second, increasing the frequency over 3 kHz will make the unit cell larger compared with the wavelength and eventually the effective medium homogenization is lost. However, the focusing properties of the lens was confirmed for frequencies as low as 1.5 kHz and as high as 4.5 kHz (Fig. 3.10). At 1.5 kHz the agreement between the simulation and the measurements is not as good as it is at other frequencies, not only because the lens dimension is only one wavelength in the y direction and thus the focusing effect is weakest, but also because as the frequency decreases (larger wavelength), the reflections from the edge of the waveguide are harder to remove.

Also, it is worth mentioning that although over 3.4 kHz there is another propagating mode present in the waveguide, it has a group velocity much lower than the first mode and does not influence our processing technique.

3.3 Conlusions

The design procedure theoretically described in Ref. [37] and experimentally confirmed in Ref. [43] was succesfully used to design a 2D broadband gradient index acoustic lens in air. The GRIN lens designed using this technique are lighter and thinner than related GRIN lenses previously reported in the literature. Also, the broadband performance of this lens was experimentally demonstrated by measurements from 1.5 kHz to 4.5 kHz.

4

Sound Manipulation Using Transformation Acoustics and Acoustic Metamaterials

Transformation acoustics is a mathematical tool which completely specifies the material parameters needed to control the wave propagation through the material. More specifically, this method shows how the acoustic waves could be bended and stretched and what kind of material will do this. As it was the case with numerous developments for acoustic metamaterials field, this technique was also adapted from the method designed for the EM waves context [11, 63], where it was shown that the material properties (i.e. electric permittivity and magnetic permeability) could be computed imposing the condition that the Maxwell's equations are invariant to coordinate transformation. For acoustic waves, the elastodynamic equations of wave propagation are not transformation invariant in general [26], but they are for the 2D case. Also, a proper mapping of these equations to some other wave equations that are transformation invariant could be used for the 3D case [28, 29]. More detailed, let us consider a transformation from the real (r) space described by the (x, y, z) coordinates to the desired, virtual (v) space specified by the (u, v, w) coordinates. Then [28, 29] :

$$\bar{\bar{\rho}}^r = \det(A)(A^{-1})^T \bar{\bar{\rho}}^v A^{-1}, \quad B^r = \det(A)B^v \quad (4.1)$$

where $\bar{\bar{\rho}}$ is the mass density tensor, B is the bulk modulus and A is the Jacobian matrix of the transformation:

$$A = \begin{pmatrix} \frac{\partial u}{\partial x} & \frac{\partial u}{\partial y} & \frac{\partial u}{\partial z} \\ \frac{\partial v}{\partial x} & \frac{\partial v}{\partial y} & \frac{\partial v}{\partial z} \\ \frac{\partial w}{\partial x} & \frac{\partial w}{\partial y} & \frac{\partial w}{\partial z} \end{pmatrix}^{-1} \quad (4.2)$$

Therefore, the transformation acoustics is a straightforward procedure and reduces to a geometric problem which attempts to find the proper transformation between the real and virtual spaces. However, even if novel and interesting devices (e.g. beam shifters, field rotators, etc. [64]) could be relatively easily designed, only few of them have been experimentally demonstrated. This is mainly because the material parameters required by such devices have extreme values (e.g. infinite mass density) or have to vary on a large scale. In addition, these material parameters are typically inhomogeneous and anisotropic. The main goal of the work presented in this chapter was to investigate the performance of two devices, a 2D acoustic black hole and a 3D acoustic cloak, realized using the currently available material parameters for acoustic metamaterials.

4.1 2D Acoustic Black Hole

As we have seen in the previous chapter, in a medium where the index of refraction varies, the wave travels towards the higher index of refraction. The ability to precisely control the index of refraction has made the idea of artificial black holes more realistic. Rigorously, the material parameters needed for an EM black hole were initially computed using the general relativity theory in electromagnetism [65] and then refined and experimentally demonstrated [66, 67, 68, 69, 70]. It has been shown

that in order to have the waves trapped inside the device, the index of refraction should have the following variation [68]:

$$n(r) = \begin{cases} \left(\frac{r_s}{r}\right)^{\alpha/2} & , r \leq r_s \\ 1 & , r > r_s \end{cases} \quad (4.3)$$

where r_s is the shell radius and α is a constant greater or equal with 2. This index of refraction radial profile leads to the rays trajectories like the ones presented in Fig. 4.1. Here, the absorbing core is reduced to a point and different colors represent different ray trajectories, based on their entering position.

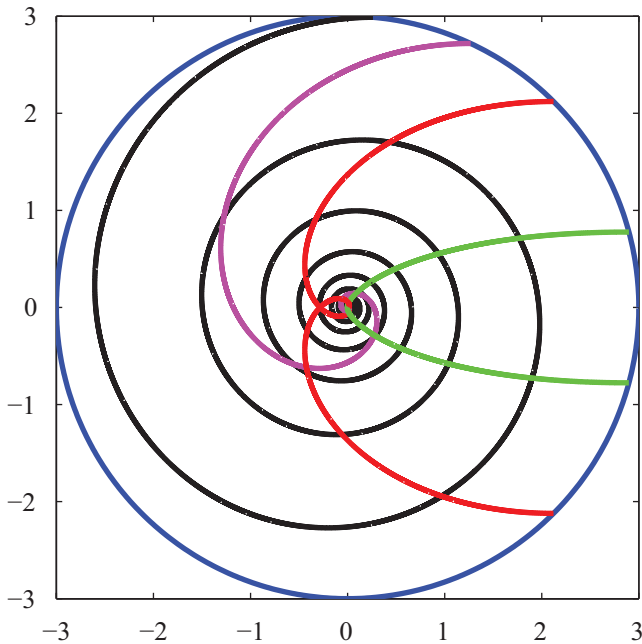


FIGURE 4.1: Ray trajectories inside an artificial black hole.

In order to build a similar artificial black hole for acoustic waves, as we have previously seen, we can either use the duality between the EM and acoustic waves or we can use the transformation acoustics. The second approach was studied in the literature for acoustic waves and a method for its practical realization was proposed [71]. However, the first method, which will be also used here, is much simpler to

convert to acoustic waves. In addition, it benefits from the variety of the solutions proposed for the EM artificial black holes. Some theoretical and experimental results for this approach have been also presented in the literature [72, 73], the index of refraction being controlled with a lattice of solid, vertical cylinders. Here, we explore the artificial black hole performance at lower frequencies, using different unit cells that will provide a larger value for the highest index of refraction and a smaller impedance mismatch between the surrounding background and the shell. As can be seen from the equation 4.3, a higher maximum value for the index of refraction allows a smaller region with graded index of refraction. Therefore, this has practical advantages, especially at lower frequencies.

For our 2D acoustic black hole we took into consideration the following: we considered our experimental setup already available in the laboratory (i.e. a 2D waveguide of 1 m^2 and with a cutoff frequency around 3.4 kHz). Therefore, our device will be placed in air background and it should have an absorbing core with a radius greater or equal with the background wavelength. The shell radius should be much larger than the same wavelength and it will also impose the maximum index of refraction that we need. According with equation 4.3, as the dimension of the device increases, the index of refraction increases. The main limitation is therefore given by the maximum value that we can get for the index of refraction with minimum shear wave effects for the current available acoustic metamaterials.

Let us consider first the cross unit cell from the previous chapter. With a better fabrication technique and a relatively small decrease in the operating frequency, the maximum value for the index of refraction that could be obtained will be close to 2.5 [44]. The pressure field map for this device is presented in Fig. 4.2. A Gaussian plane wave is impinging on the artificial black hole at an arbitrary angle and the pressure is computed at every point using the COMSOL Multiphysics® software with its Pressure Acoustics Module. Perfectly matched layers are used around the waveguide

to eliminate the reflections from the edges. As can be seen, the performance is fair and even if the acoustic wave is bended toward the absorbing core, the scattering is present in the system.

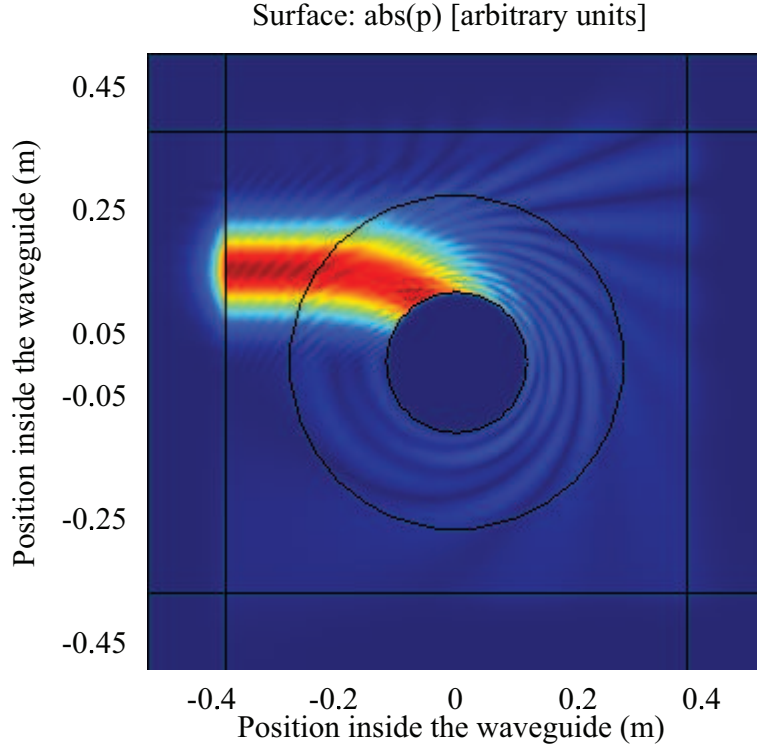


FIGURE 4.2: 2D acoustic black hole pressure field map ($f=12$ kHz, maximum index of refraction 2.5).

If we keep the same dimensions (i.e. $\alpha = 2$ and $r_s \approx 2.5r_c$) for the device but we select a different unit cell [45], the performance is greatly improved (see Fig. 4.3). We should mention that in this case, the unit cell is composed of a solid slab with a perforated hole in the middle, and the index of refraction is controlled by the size of the hole. The main advantage of this design is that it allows a maximum value for the index of refraction close to 6, but in the meantime the perforated plates are known to have large losses at low frequencies (see for example Ref. [74]). Therefore, the operating frequency for our device will be reduced.

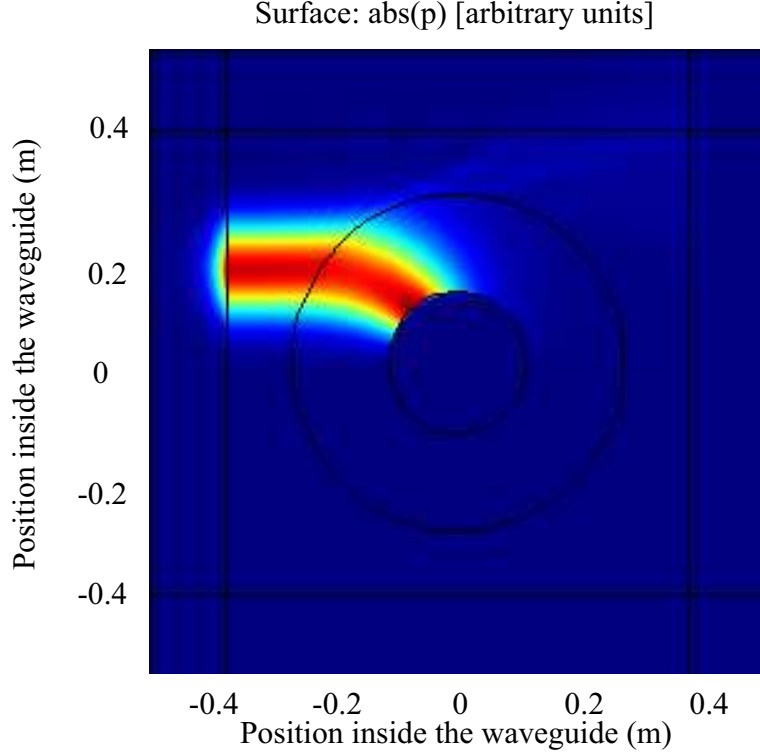


FIGURE 4.3: 2D acoustic black hole pressure field map ($f=12$ kHz, maximum index of refraction 6).

If we perform the same simulations at 3 kHz (i.e. an operating frequency suitable for the unit cells proposed and for our 2D acoustic waveguide), the performance is drastically reduced. The main reason in performance reduction is a relatively small size of the guiding shell compared with the wavelength (Fig. 4.4). We should mention that the device performance is also influenced by the overall performance of the absorbing core (e.g. absorption rate $\eta \approx 1000$ for our case), as described in Refs. [71, 73].

We performed two additional tests in order to observe the omni directional absorbing property of our device. The sound source is placed such that the Gaussian plane wave is normally incident on the device and the results showing the pressure field maps are presented in Fig. 4.5.

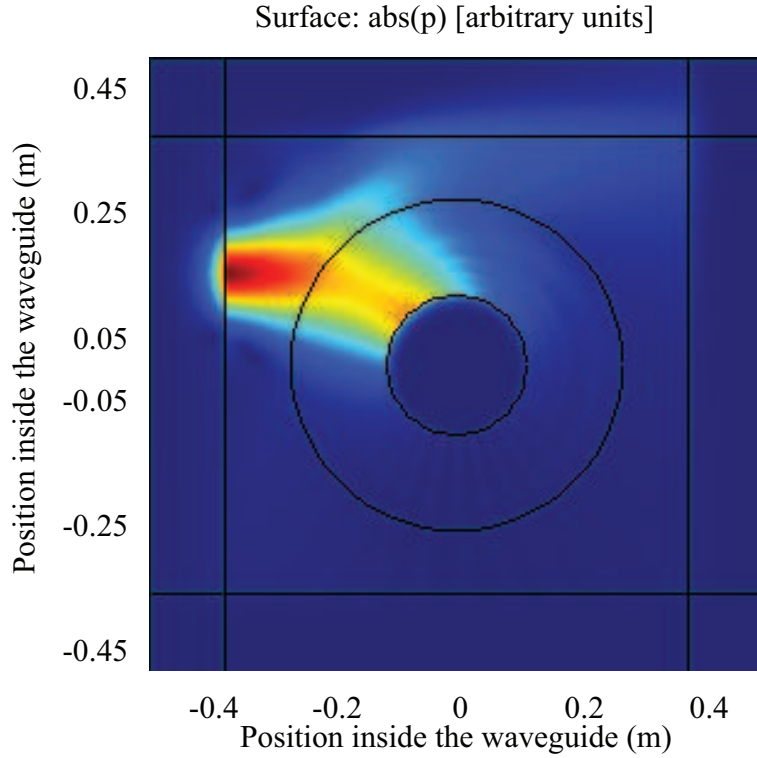


FIGURE 4.4: 2D acoustic black hole pressure field map ($f=3$ kHz, maximum index of refraction 6).

In conclusion, the maximum currently achievable index of refraction could be used to experimentally realize an artificial 2D acoustic black hole. The dimensions of the device are completely specified: 0.27 m outer shell radius, 0.11 m core radius, $\eta \approx 1000$ for the absorbing core, radially and equidistant placed unit cells that will fill the shell. The procedure for the index of refraction to follow a specific profile was described in detail in the previous chapter. For the cross unit cell, the index of refraction of each unit cell is controlled by the dimension of the cross. In the perforated plate unit cell case, the refractive index is tuned by changing the diameter of the hole. We should mention that in order to have the device working at 12 kHz, the unit cell size will be smaller for homogeneity considerations (i.e. the unit cell will have to be at least 10 times smaller than the wavelength). Also, the maximum value

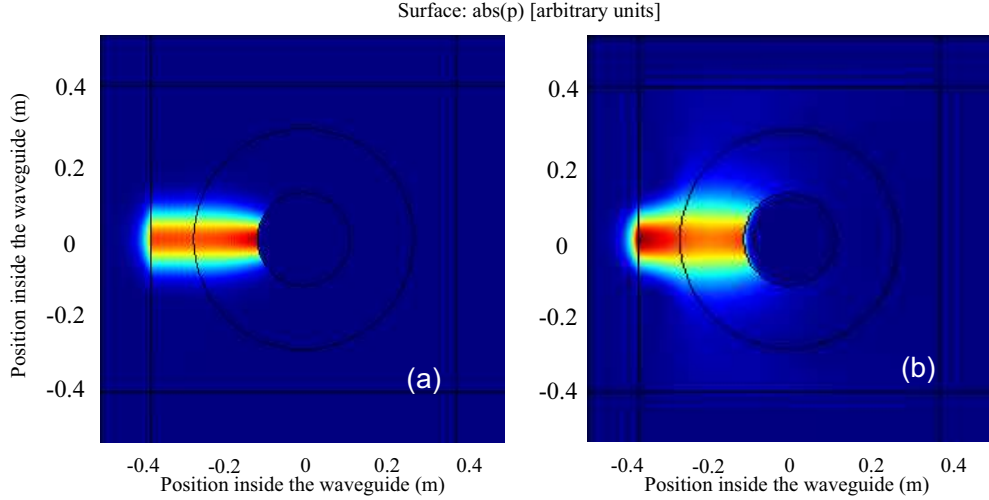


FIGURE 4.5: 2D acoustic black hole pressure field map (maximum index of refraction 6, $f=12$ kHz (a) and $f=3$ kHz (b)).

for the index of refraction that we have taken into consideration is one that could be relatively easily achieved with our fabrication expertise. Otherwise, the index of refraction could be higher. For example, a perforated plate with the unit cell of 0.5 mm with a hole of 0.01 mm will have an index of refraction of approximately 12 at 12 kHz.

4.2 3D Acoustic Ground Cloak

One of the most investigated devices that could be created using the transformation acoustics is the acoustic ground cloak (e.g. a comprehensive review is presented in Ref. [75]). However, even if the recipe to build these devices is relatively easy in theory, only few devices have been experimentally reported. This is mainly because the material parameters required by the cloaking shell that covers the object to hide have extreme values and are very anisotropic and inhomogeneous. For one particular case, the so called ground or carpet cloak, these material parameters have values that could be implemented in practice with some trade off in performance, as we will see

later. It has been theoretically and experimentally shown for the 2D case how such an acoustic cloak could be realized [45]. Here, we use our expertise on this case and extend it to the 3D case, designing and evaluating the performance of differently shaped 3D cloaks placed in air background.

4.2.1 Square Pyramid Shaped Cloak

Let us consider that the object that we want to hide is a solid square based pyramid placed in air background and that the cloaking shell is also a square pyramid, sharing the same base (Fig. 4.6). We should note that $a = 0.5\lambda$, $b = 1.5\lambda$, $c = \lambda$, where λ is the wavelength in air background at the design frequency (11.43 cm). These dimensions will ensure that the cloak will have a reasonable size, comparable with the object that is hiding.

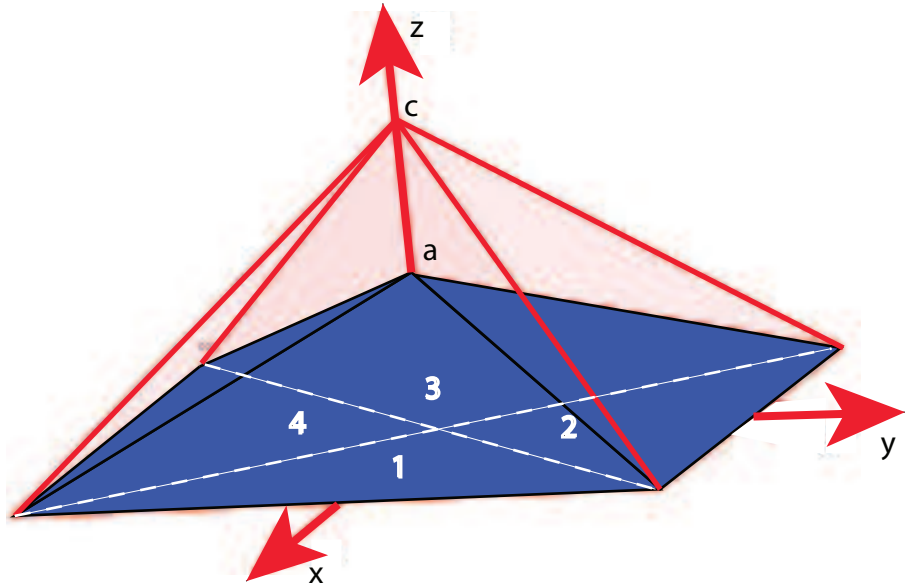


FIGURE 4.6: 3D acoustic cloak for a square pyramid solid object.

Therefore, we need a geometric transformation that will map the blue pyramid, our object to hide in real space (x, y, z) into an infinitely small pyramid in the virtual space (u, v, w). Also, we need this transformation to be linear, because it will lead,

as it was the case for 2D, to a homogeneous cloaking shell. We can split the large pyramid volume into four regions corresponding to the signs of x and y coordinates. A suitable transformation that will meet these requirements is presented below and the full description of the procedure to obtain it is presented in Appendix C.

$$\begin{cases} u = x \\ v = y \\ w = \frac{c}{c-a} \left(\frac{a}{b} \text{sign}(x)x + z - a \right) \end{cases} \quad (4.4)$$

and

$$\begin{cases} u = x \\ v = y \\ w = \frac{c}{c-a} \left(\frac{a}{b} \text{sign}(y)y + z - a \right) \end{cases} \quad (4.5)$$

We can use now the equations 4.1, 4.2 to compute the mass density tensor and the bulk modulus. The material parameters required for the cloak are the eigenvalues (principal components) of the mass density tensor and the bulk modulus:

$$\begin{cases} \rho_{11}^{pr} = 2.28 \\ \rho_{22}^{pr} = 0.5 \\ \rho_{33}^{pr} = 0.44 \\ B^{pr} = 0.5 \end{cases} \quad (4.6)$$

We should note that this material parameters are relative to the background material parameters. For example, in this case the unit cells that will fill the cloak region should have a mass density in one direction 2.28 larger than the mass density of air. But having a natural material less dense and more compressible than air in two directions is not possible. However, we could overcome this impediment following a similar approach with the 2D case: consider that the background is not air but a material described by the following material parameters:

$$\begin{cases} \rho_{background} = m\rho_{air} \\ B_{background} = mB_{air} \end{cases} \quad (4.7)$$

where m is a scaling factor.

For this case, the material parameters required by the cloak are:

$$\begin{cases} \rho_{11}^{pr,new} = m\rho_{11}^{pr} \\ \rho_{22}^{pr,new} = m\rho_{22}^{pr} \\ \rho_{33}^{pr,new} = m\rho_{33}^{pr} \\ B^{pr,new} = mB^{pr} \end{cases} \quad (4.8)$$

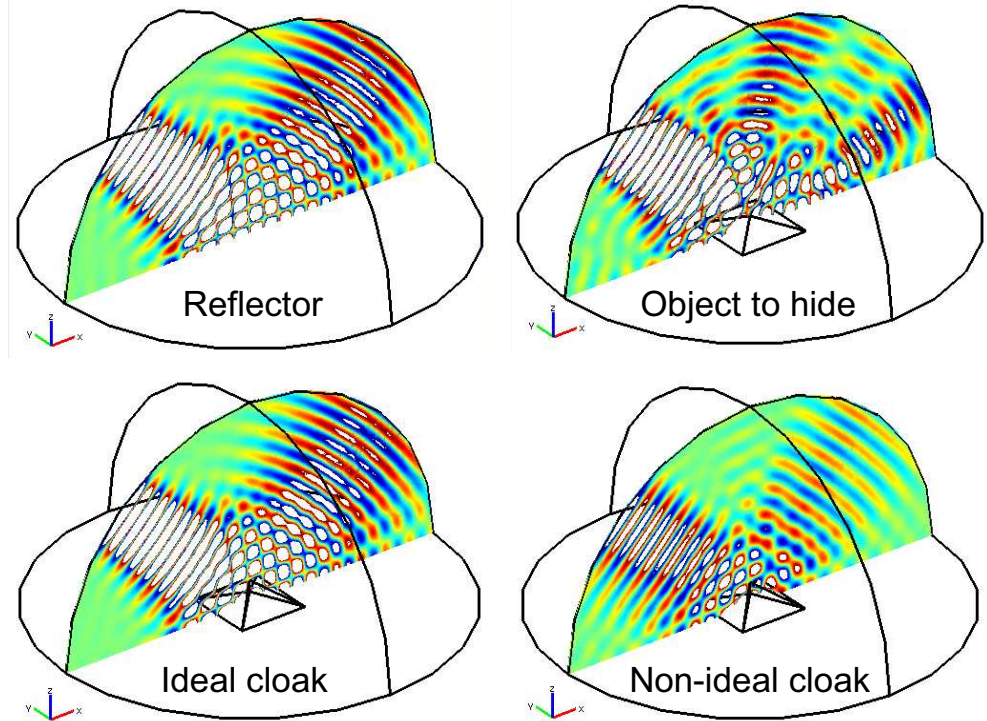


FIGURE 4.7: Cross sectional pressure field maps for: (a) perfect reflector, (b) square pyramid object to hide, (c) square pyramid object to hide and ideal cloak, (d) square pyramid object to hide and non ideal cloak ($m=2.5$).

Consequently, a properly chosen value for the parameter m will lead to effective material parameters that are currently achievable. The price paid is a small

impedance mismatch between the cloak and the air background. For exemplification, we present the simulation results in Fig. 4.7 for $m=2.5$.

The simulations are performed using the Pressure Acoustic module of *COMSOL®* Multiphysics. A Gaussian pressure plane wave is impinging on the ground (perfect reflector), object to hide, object to hide covered with the ideal cloak and object to hide masked by the non ideal. The pressure field is computed in the entire domain. As can be seen, the decrease in the performance due to the non ideal cloaking shell is minimal.

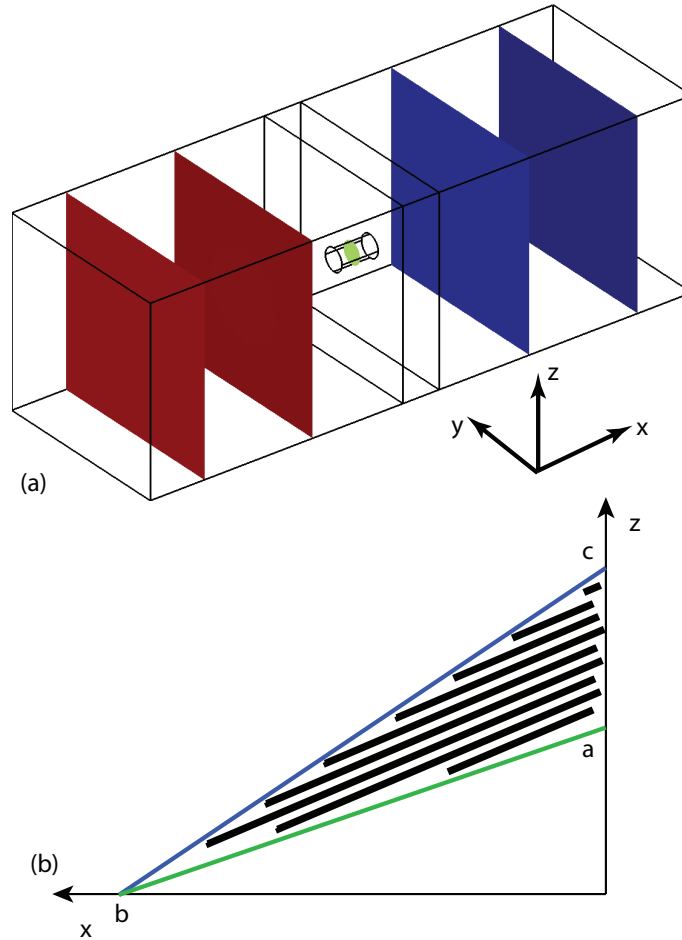


FIGURE 4.8: (a)Unit cell and (b) cloaking shell filling suggestions for square pyramid cloak.

One other advantage of using $m=2.5$ is that two components of the mass density tensor have exactly the same value as for the 2D case, 5.71 and 1.25 respectively. Also, the third one has a very close value, 1.09. Therefore, we can use the exact same unit cell like for the 2D case (Fig. 4.8 (a)). It has been shown that for this kind of unit cell, the effective mass density in one direction is controlled by the hole diameter and in the other two directions by the slab thickness [45]. Also, the bulk modulus is proportional with the volume ratio solid to air. A 1 mm thick plate with 1.6 mm diameter holes will produce a 5.6, 1.26 and 1.26 effective mass densities and 1.22 bulk modulus, values that are very close to those required by the design. In Fig. 4.8 (b) we show a suggestions about how the cloaking region 1 will be filled with unit cells ($y=0$): the green line represents the edge of the object to hide and each black rectangle represents a perforated panel. The holes in the perforated panel are the ones described above and they are oriented towards the origin of the coordinate system. Also, the orientation of each panel is determined from the diagonalization process of the mass density tensor (i.e. the angles that we need to rotate the coordinate system such that the mass density matrix will become a diagonal one). Due to the symmetry with the 2D problems, the angles should be the same like in that case. The blue line represents just the edge of the cloaking region and it could be thought as a continuity boundary, with no correspondent in the experimental implementation. Supplementary, we computed the pressure fields for a similar design, with only two cloaking regions instead of four, but no changes in performance were observed.

4.2.2 Cone Shaped Cloak

In order to reduce the cloak cross section, we consider other shapes for the object to hide and therefore for the cloaked region. Then, we investigate if a non linear transformation will lead to material parameters that are close to those achievable in practice and what the overall performance is.

Let us consider the case depicted in Fig. 4.9.

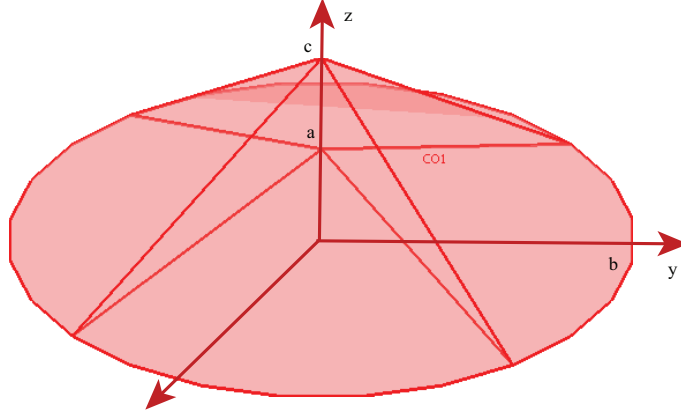


FIGURE 4.9: 3D acoustic cloak for a cone shaped solid object.

A transformation that will map the object to hide points into ground points will be the following (see Appendix C for a more detailed description):

$$\begin{cases} u = x \\ v = y \\ w = \frac{c}{c-a} \left(\frac{a}{b} \rho(x, y) + z - a \right) \end{cases} \quad (4.9)$$

where $\rho(x, y) = \sqrt{x^2 + y^2}$.

Using the same steps as in the previous section, we can derive the material parameters required by the ideal cloak and then their corresponding scaled values that will be used in practice. Although the transformation is not linear, we obtain the same material parameters as for the previous case, only this time each cell will have a different orientation. Moreover, they are homogeneous.

The simulations performed show that the non ideal cloak performs well and the reduction in performance compared with the ideal cloak is minimal (Fig. 4.10). From the practical realization point of view, we should refer to Fig. 4.8 (b), and note that for this case each black rectangle will represent a perforated cone like in Fig. 4.11. All the cones will have the top along the z axis and will be stacked one

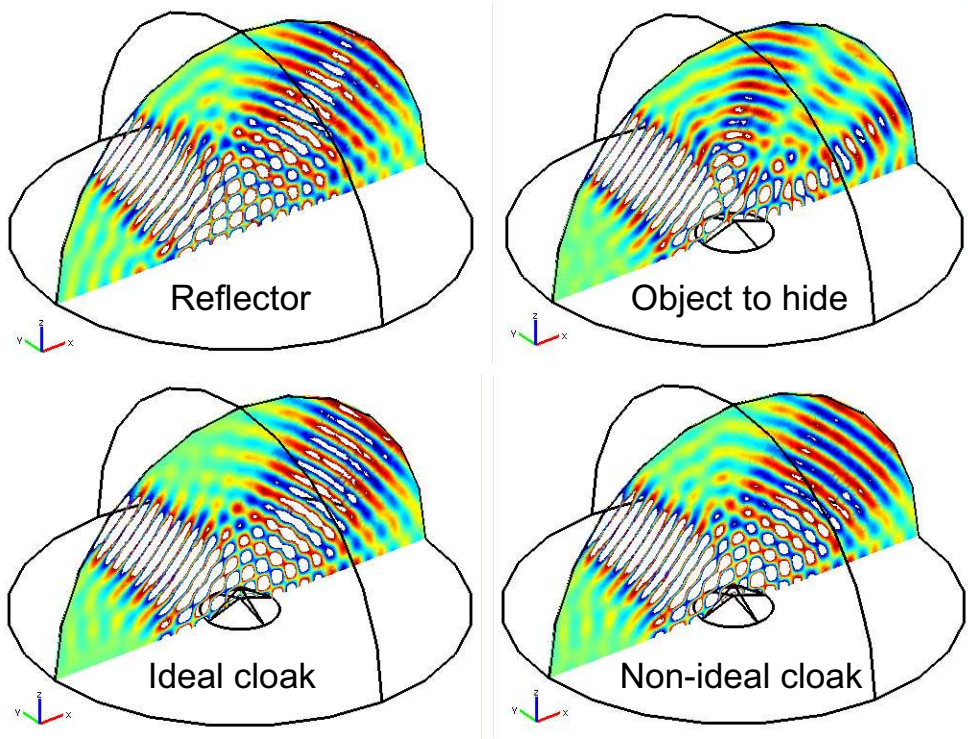


FIGURE 4.10: Cross sectional pressure field maps for: (a) perfect reflector, (b) cone shaped object to hide, (c) cone shaped object to hide and ideal cloak, (d) cone shaped object to hide and non ideal cloak ($m=2.5$).

in top of the other with a vertical spacing equal to the distance between two solid inclusions of two consecutive unit cells (i.e. the vertical spacing that will ensure that the black rectangles will be placed at the proper location, as designed). The cone corresponding to the green line will be a solid one, without any perforations. The blue line again will not have a correspondent in the experimental device. Due to limitations in computing resources we were not able to simulate the entire structure. We estimate that the cone surface curvature will introduce minimal variations in the effective material parameters of the unit cells.

This cone shaped cloak do not meet the goal of reducing the cross section dimension but it offers us an insight of the possible existence of some non linear transfor-

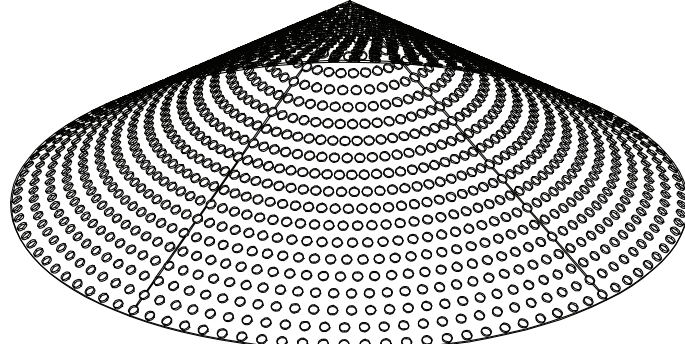


FIGURE 4.11: 3D acoustic cloak for a cone shaped solid object.

mation that will eventually lead to homogeneous cloak.

4.2.3 Crescent Shaped Cloak

We can build on the experience of the cone shaped cloak and change the object to hide in crescent, like in Fig. 4.12.

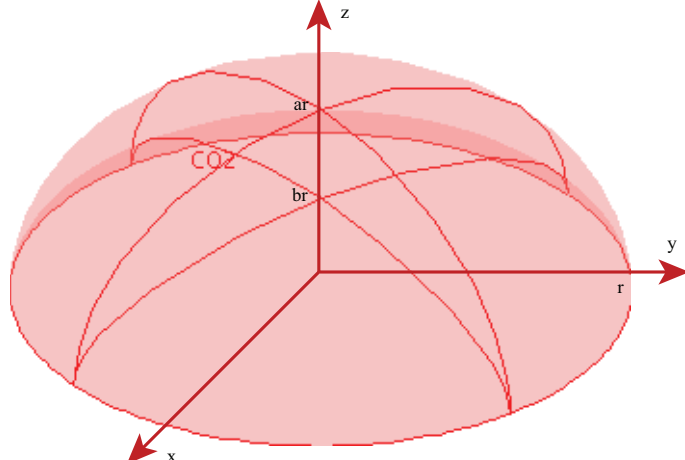


FIGURE 4.12: 3D acoustic cloak for a crescent shaped solid object.

We choose to relate the crescents heights (object to hide crescent and cloak crescent) to the base radius r through the constants a and b in order to make the computations for different form factors easier. A suitable transformation for this case would be (see Appendix C for the complete derivation of these expressions):

$$\begin{cases} u = x \\ v = y \\ w = \frac{a}{a-b} \left(-br\sqrt{1 - \frac{x^2+y^2}{r^2}} + z \right) \end{cases} \quad (4.10)$$

Using the same procedures described in the previous sections, we can derive the effective material parameters required by the cloaking shell. For the particular case when $r = 1.5\lambda$, $ar = \lambda$ and $br = 0.5\lambda$, the simulation results are presented in Fig. 4.13.

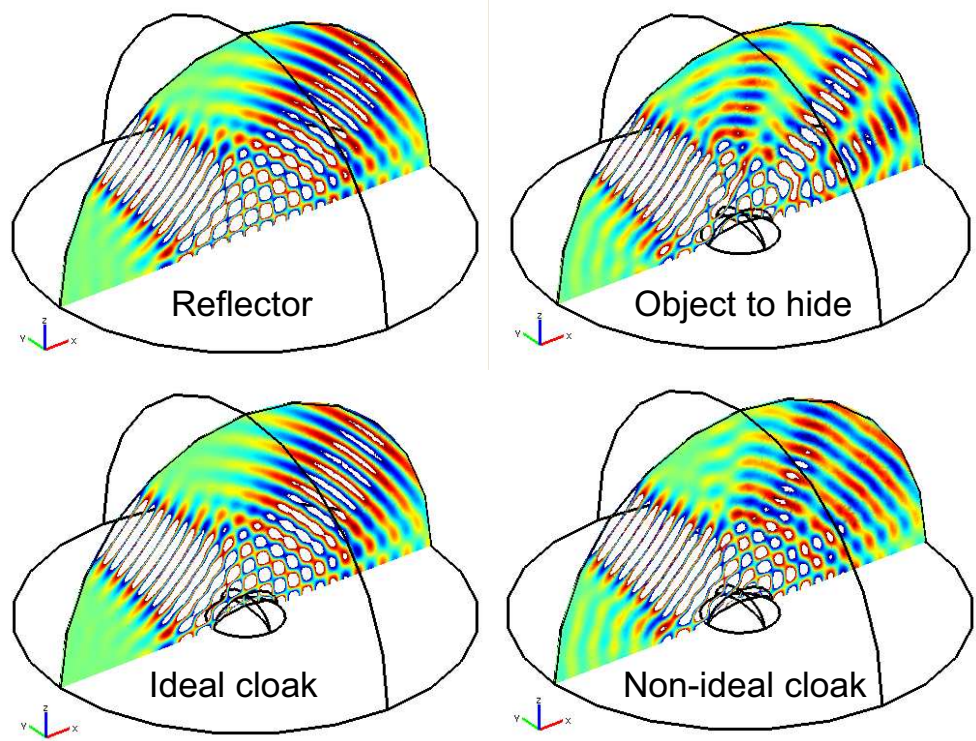


FIGURE 4.13: Cross sectional pressure field maps for: (a) perfect reflector, (b) crescent shaped object to hide, (c) crescent shaped object to hide and ideal cloak, (d) crescent shaped object to hide and non ideal cloak ($m=2.5$).

The main problem encountered by this design is that it requires non homogeneous material parameters. In addition, a scaling factor of $m = 2.5$ will not bring all

the regions in the cloaking area to "achievable". That is, the regions close to the edges will have mass densities and bulk modulus that cannot be experimentally realized with the current acoustic metamaterials. However, as can be seen, the performance of the non ideal cloak is acceptable. Therefore, by cutting out the regions with parameters that could not be realized in practice, we can have a cloaking effect. But, the experimental realization would still be extremely difficult due to the inhomogeneity property of the cloak.

We should mention that all the numerical simulations for all the cloaks considered are on the same scale (even if the units are arbitrary chosen) in order to have relevant comparisons between different cases.

4.3 Conclusions

This work evaluated the performance of two devices designed through transformation acoustics method and implemented experimentally using the current achievable acoustic metamaterials. We used the well known transformation acoustics design technique and propose new, specific experimental realizations recipes for: a 2D omnidirectional absorber and a 3D acoustic cloak. Although non ideal, these devices display excellent performance.

5

Active Acoustic Metamaterials

In this chapter we briefly review the current trends in the field of active acoustic metamaterials and then propose a path to achieve tunable effective material parameters using active elements.

5.1 Motivation

As we have seen in the previous chapters, the numerical design method for passive acoustic metamaterials using a solid inclusion in a fluid background is a very robust one and can be successfully applied in practice. However, there are certain limitations of this method. First, if one needs to vary the values of the effective mass density with many orders of magnitude, then the practical realization of such a metamaterial using solid inclusions in background fluid will be extremely challenging, as the gap between consecutive unit cells or the diameter of the perforation will become smaller and smaller. Second, as it was emphasized in Ref. [45], implementing in practice material parameters that highly vary with position or have mass density tensor components that are much smaller than the surrounding background is very difficult if not impossible to create experimentally with the previous approaches. Therefore, a new

class of acoustic metamaterials is needed: active acoustic metamaterials (AAMM). In this case, the unit cell will comprise an acoustic sensor, an active circuit which will be used to control the material parameters and acoustic drivers excited by the active element (Fig. 5.1).

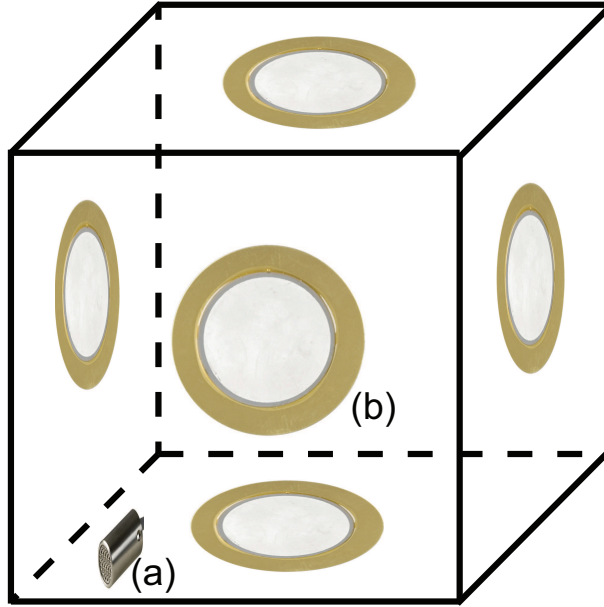


FIGURE 5.1: Schematic diagram of an active acoustic metamaterial unit cell: (a) sensing element and active driving circuit, (b) acoustic driver.

We should note the the sensing and the driving acoustic elements could be the same in some instances. For example, a piezoelectric (PZT) membrane could be used as a microphone and/or speaker at the same time. From the geometric point of view, all the unit cells will be identical.

5.2 One Path to AAMM

The field of AAMM is in the very incipient phase and only few theoretical and experimental advances have been reported in the literature. Lee et al. showed that a chain of cavities separated by thin elastic membranes will act as a 1D acoustic metamaterial with negative effective density [76]:

$$\rho_{eff} = \rho' \left(1 - \frac{\omega_c^2}{\omega^2} \right) \quad (5.1)$$

where ω is the frequency and ω_c is the critical frequency dictated by cavity dimensions and material parameters of the membrane.

As can be seen in the above relation, when the frequency is smaller than the critical frequency, the effective density takes negative values.

Inspired by this work, Baz [38, 77] attempted to answer the following question: what if instead using a membrane and changing the cavity dimensions we use the same cavity but replace the membrane with a piezoelectric boundary? (see Fig. 5.2, adapted from Ref. [77])

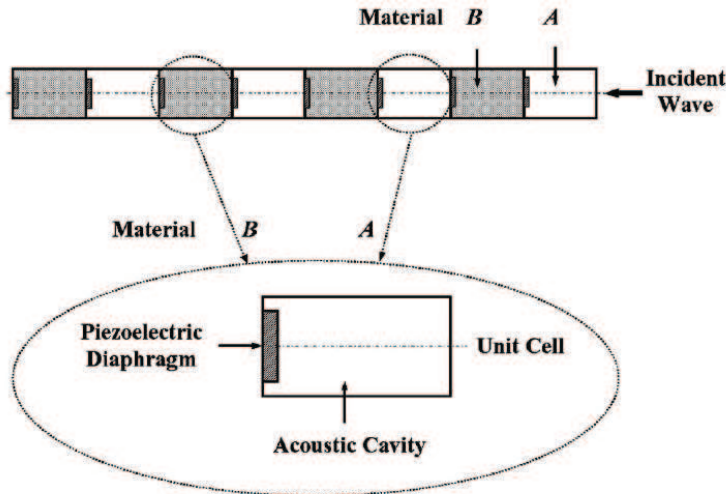


FIGURE 5.2: AAMM unit cell based on a cavity and a piezoelectric membrane [77].

Using an analog electric model for the acoustic cavity and the electric model for the piezoelectric crystal, a direct relationship between the effective density and the control voltage could be determined. From the practical implementation point of view, we should note that at low frequencies the value of the voltage that should be applied on the piezoelectric crystal in order to achieve the desired effective mass

density is very large (hundreds of volts, which is not a realistic value that can be carried on by these materials) but it will dramatically decrease at higher frequencies. These work demonstrates that, at least theoretically, an AAMM with tunable effective mass density is possible.

Using a similar approach, a piezoelectric diaphragm was placed at the bottom of a Helmholtz resonator and the relationship between the effective bulk modulus and the control voltage was computed [39]. This correlation, as it was the case above, involves only the cavity dimensions, the piezoelectric membrane material parameters and bulk modulus of the surrounding background. Again, the control voltage is extremely high at low frequencies and it decreases as the frequency increases.

These theoretical findings have been used to experimentally demonstrate a piezoelectric based unit cell with tunable impedance and transmission loss [78].

5.3 Theoretical Model

As we have seen from equations 2.6 and 2.7, the index of refraction and the impedance of a unit cell could be expressed as a function of the wave number in the background, sample thickness and the reflection and transmission coefficients. Therefore, assuming the same background and thickness for all the unit cells, the effective mass density and bulk modulus of a medium made with these unit cells will depend only on the reflection and transmission coefficients values (see the relations 2.8 and 2.9). Our approach for AAMM will be to tune the material parameters by controlling how the unit cell will respond to the incident wave (i.e. the reflection and transmission coefficients of the unit cell).

Let us consider that the sensing element of the unit cell is a microphone. The total pressure at the microphone can be written as a function of the incident and reflected pressure:

$$p_{t,mic} = p_{inc} + p_{refl} \quad (5.2)$$

Assuming that the amplification process introduces some amplitude and phase changes, the transmitted and reflected pressure due to the amplified signal applied to the PZT is:

$$p_{refl,ON} = G_1 e^{j\phi_1} p_{t,mic} \quad (5.3)$$

$$p_{trans,ON} = G_2 e^{j\phi_2} p_{t,mic} \quad (5.4)$$

where G_1 , G_2 , ϕ_1 , ϕ_2 represents the gains and phases introduced by the amplifier. We should note that we used two different gains and phases because some PZT membranes are different on the two sides. The *ON* subscripts indicate the fact that these pressures are due to the amplifier turned on.

Therefore, the reflection and transmission coefficients could be written as functions of the pressures when the amplifier is on and off:

$$S_{11,ON} = \frac{p_{refl,OFF} + p_{refl,ON}}{p_{inc}} = S_{11,OFF} + \frac{p_{inc} + p_{refl}}{p_{inc}} G_1 e^{j\phi_1} \quad (5.5)$$

$$S_{11,ON} = S_{11,OFF} + (1 + S_{11,OFF}) G_1 e^{j\phi_1} \quad (5.6)$$

$$S_{21,ON} = \frac{p_{trans,OFF} + p_{trans,ON}}{p_{inc}} = S_{21,OFF} + \frac{p_{inc} + p_{refl}}{p_{inc}} G_2 e^{j\phi_2} \quad (5.7)$$

$$S_{21,ON} = S_{21,OFF} + (1 + S_{21,OFF}) G_2 e^{j\phi_2} \quad (5.8)$$

Consequently, the reflection and transmission coefficients and implicitly the effective mass density and bulk modulus will be tuned by the active element consisting in microphone, amplifier, PZT assembly.

5.4 Piezoelectric Based Active Acoustic Metamaterial

5.4.1 Experimental Design

We consider the experimental setup presented in Fig. 5.3. The PZT crystal is fixed in a custom made Plexiglas holder, with the microphone fixed on one side and the amplifier on the other side. The amplifier's gain is chosen such that it will produce a significant level for the signal applied to the PZT and in the same time will keep the sample stable. The 1D sample is placed in the custom made, 1D acoustic waveguide described in Chapter 2 and the reflection and transmission coefficients are measured. In order to have a relevant unit cell (i.e. a unit cell with dimensions significantly smaller than the wavelength) and having the constraints imposed by the waveguide dimensions, our target operating frequency range for the active acoustic metamaterial is 1-3 kHz.

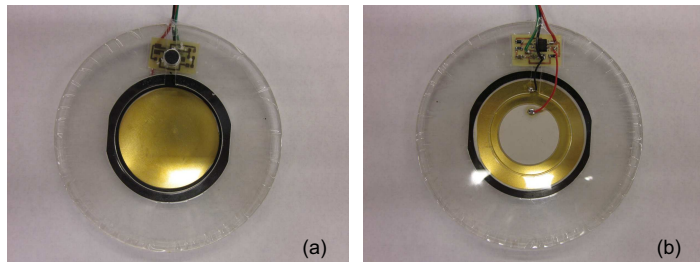


FIGURE 5.3: Snapshots of a 1D PZT based AAMM unit cell: (a) front view (towards the incident wave) and (b) back view.

5.4.2 Measurements and Results

The signal applied to the PZT should be large. However, even for these large values, the pressure wave generated by the PZT is still very weak. Therefore, in order to have comparable levels for the incident pressure and the pressure generated by the PZT, a large gain for the signal collected by the sensing element is needed. Also, as seen in Chapter 2 the method for retrieving the effective materials parameters in our 1D waveguide works better if the amplitude of the signals measured at the two microphones is not extremely small. In our case, since the transmission through the PZT when the amplifier is turned off is very small, we drilled some holes in the plastic holder in order to increase it. We considered two types of amplifiers: *internal* (i.e. attached to the unit cell) and *external* (with the advantage of gains easily adjustable and filtering capabilities but with the disadvantage of eventual phase shifts introduced by the cables from microphone to the amplifier and from amplifier to the PZT). The goal is to investigate how the change in the amplifier's gain will tune the effective material parameters (i.e. we are looking for a relation between amplifier's gain and G_1 , G_2 , ϕ_1 , ϕ_2). Several samples were made and the results for the ones that are stable and show significant effective material properties are shown below.

Figure 5.4 shows the measurement results for a PZT based sample with an internal amplifier, gain around 4800. For this sample, when the amplifier is turned off, the effective mass density is around 130 and the bulk modulus is around 2 (note: all the material parameters referred here are relative to air background). As can be seen, while the bulk modulus remains almost unchanged compared with the passive sample, the effective mass density is significantly lowered and is strongly varying with the frequency.

If we lower the gain to 2300 and we keep the amplifier attached to the unit cell,

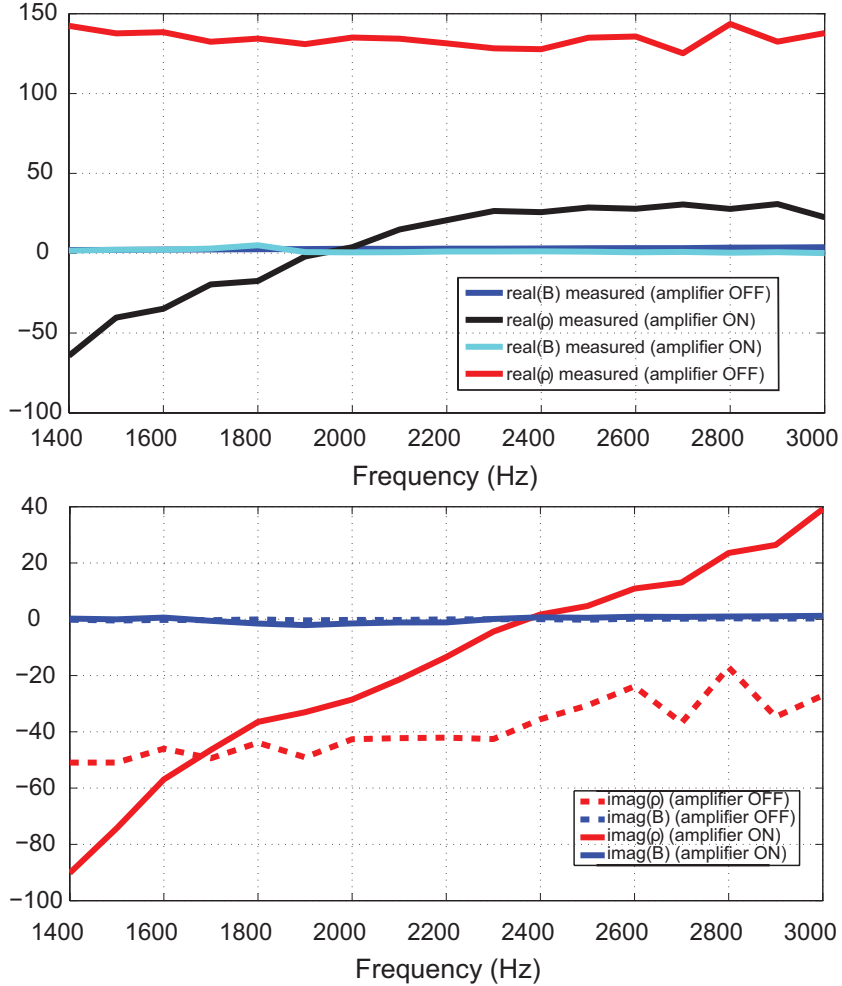


FIGURE 5.4: PZT based AAMM sample 1: real part (top) and imaginary part (bottom) for the effective mass density and bulk modulus.

the effective mass density is lowered again, but not as much as in the previous case. The effective bulk modulus has comparable values with the first sample (see Fig. 5.5). For this sample, when the amplifier is turned off, the effective mass density is around 200 and the bulk modulus is around 5.

By comparison of the two samples, we could note that:

- Due to slight differences in the holding mechanisms for the samples and for the sample in the tube, the effective mass density when the amplifier is turned off

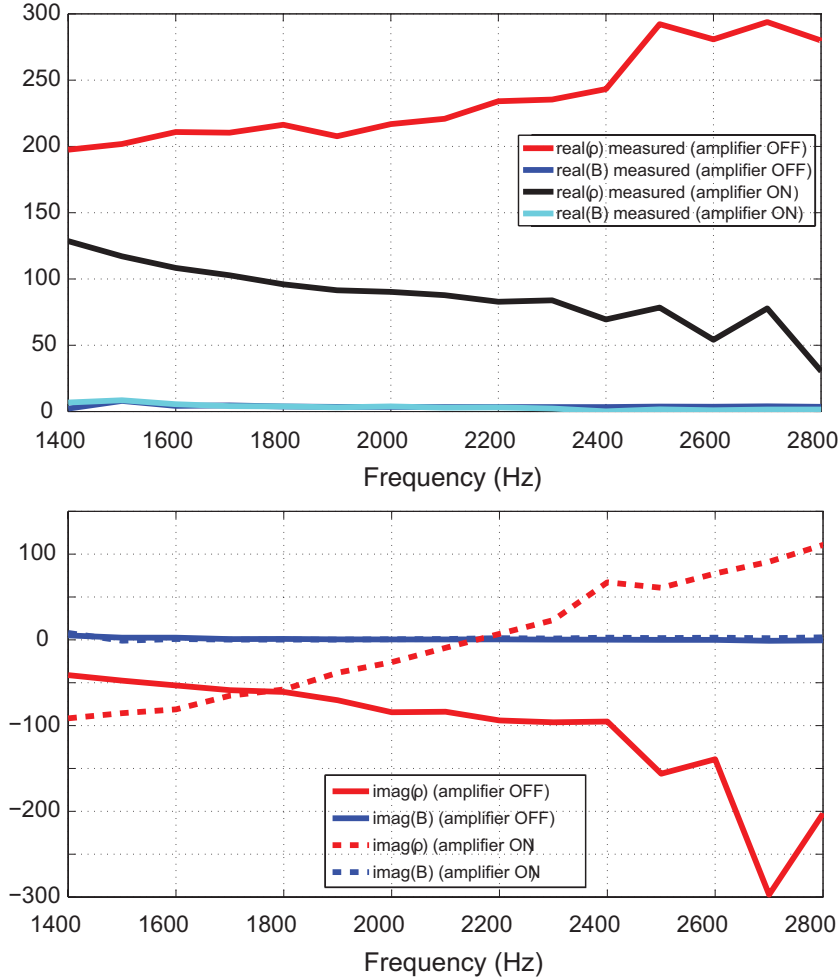


FIGURE 5.5: PZT based AAMM sample 2: real part (top) and imaginary part (bottom) for the effective mass density and bulk modulus.

differs from sample to sample.

- As it was mentioned in the Chapter 2, the time domain method for retrieving the effective materials parameters works better if the amplitude of the signals is not extremely small. In our case, since the transmission through the PZT when the amplifier is OFF is very small, we drilled some holes in the plastic holder in order to increase it. But for the active response to the incident wave is slightly delayed, therefore a new, frequency domain method to compute the

effective material parameters is needed. For this frequency domain approach, we perform again three sets of measurements and we isolate the reflection and transmission signals, similarly with the time domain method. The reflection coefficient is now computed by the ratio of the Fourier transforms of the signals recorded by the first microphone (before the sample) in two cases: sample in the waveguide and perfect reflector in the waveguide. Similarly, the transmission coefficient is computed dividing the Fourier transform of the signal recorded by the second microphone (after the sample) when the sample is placed in the tube with the Fourier transform of the signal recorded at the same channel when the waveguide is empty.

- The imaginary parts of the computed effective material parameters are very large, which suggests that there are significant losses in the system. We observed that for samples with a relatively small index of refraction, this imaginary part tends to be smaller. Therefore, new samples that feature a relatively small index of refraction when the amplifier is turned off were made, as we will see later.

In order to easily change the gain values and to use filtering capabilities that allows more stable samples, we connected the sensing element of the active cell to an external amplifier and then back to the acoustic driver of the unit cell.

For this sample, when the amplifier is turned off, the effective mass density is around 130 and the bulk modulus is around 3. A band pass filter from 1 kHz to 3 kHz is also used. We also try to keep the connection wires as short as possible in order to avoid unnecessary phase changes. The effective mass density is again controlled by the active element and is strongly varying with frequency while the bulk modulus is relatively constant over the frequency range and is not dramatically changed when the active element is used. Also, the loses are still very large.

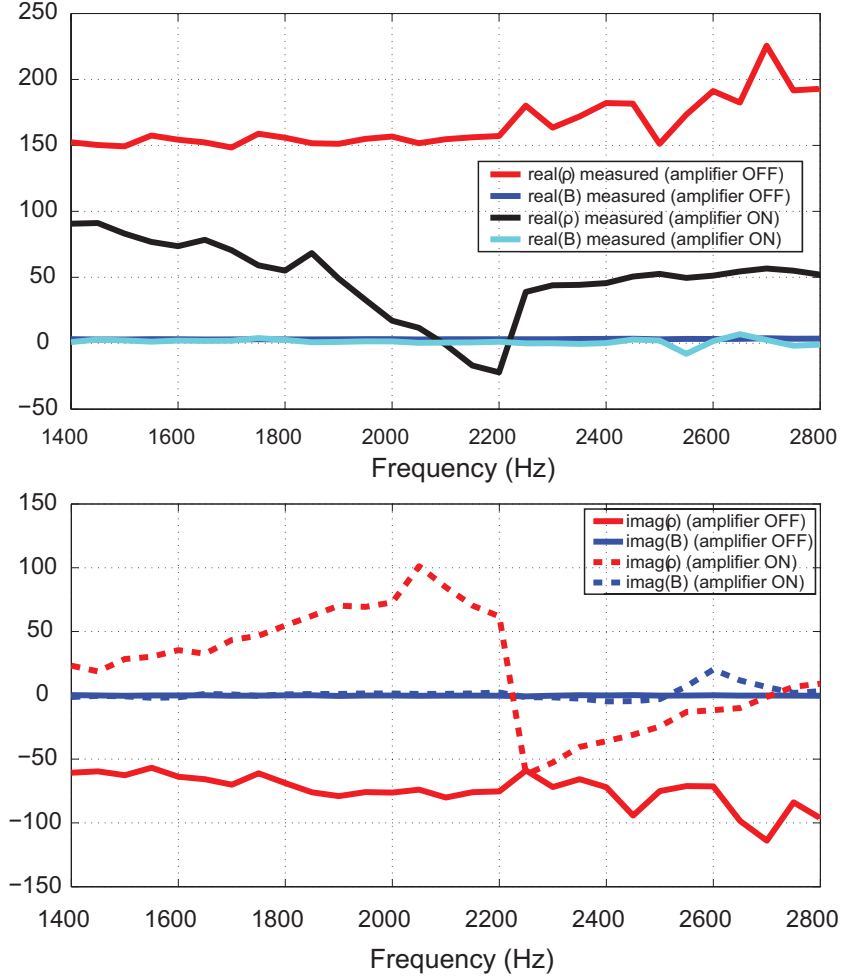


FIGURE 5.6: PZT based AAMM sample 3: real part (top) and imaginary part (bottom) for the effective mass density and bulk modulus.

We should note that, in order to keep the sample stable and also to obtain the maximum possible sound from the PZT membrane, several supplementary measurements and setups have been performed. For example, the frequency response of our PZT samples as well as their complex impedance have been documented and several amplifiers setups have been tried.

5.4.3 Theoretical Model Evaluation

In order to evaluate the model performance we choose the following path: having the measured values for the reflection/transmission coefficients for the active/passive unit cells, we compute the theoretical model parameters G_1 , G_2 , ϕ_1 , ϕ_2 (see equations 5.6 and 5.8) that would perfectly match the model results with the measured results (Fig. 5.7). Then, we evaluate these parameters and try to find the relation between them and the amplifier's gain. If we precisely determine this relation, then we can find what type of amplifier will produce in practice the desired values for the material parameters.

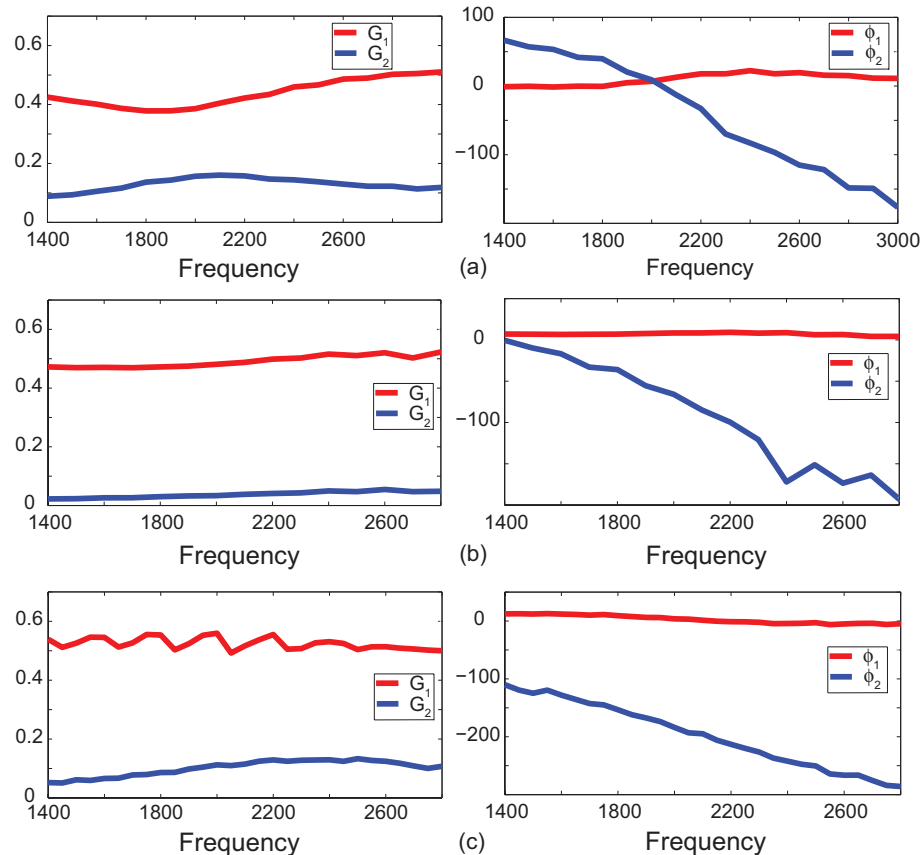


FIGURE 5.7: Measured theoretical model parameters for: (a) sample 1, (b) sample 2 and (c) sample 3.

From Fig. 5.7 we observe that:

- Gains are relatively constant in both directions over the frequency range and changing the amplifier gain changes the G values only in the transmitted wave direction and not in the reflected wave direction. This could be intuitively attributed to the fact that the PZT has a metal sheet covering it in the reflection wave direction.
- Phases are relatively constant over the frequency range in the reflected wave direction, but not in the transmitted wave direction.

Therefore, even if the model performs well over the frequency range and its behavior is reasonably explained, the change in phase for the active signal generated in the transmitted direction needs further explorations. Also, our samples are modestly dispersive due to the high variation of piezoelectric membrane response with frequency and consequently, a frequency domain method to compute the reflection and transmission coefficients is developed. Moreover, the 1D circular acoustic waveguide make a harder transition from one dimensional to two dimensional applications. Consequently, we custom designed a rectangular 1D acoustic waveguide with one of the invariant directions adjustable and the other one fixed at the same height as the parallel plate waveguide.

5.5 Piezoelectric Based Active Acoustic Metamaterial - Rectangular Unit Cell

The practical realization of the 1D rectangular waveguide is presented in Fig. 5.8. It is similar with the circular one presented in Chapter 2: a sound generated by a regular PC speaker travels in a rectangular acoustic waveguide and two microphones, placed at fixed positions, record the sound pressure before and after the sample. The position of the microphone is chosen such that the incident and reflected pulses do not

overlap. The collected signals are sent to the data acquisition card using a *National Instruments*TM terminal block and *Matlab*[®] codes are used to process them. The waveguide is built using 1/4" thick PVC plastic sheets. In order to keep the design's versatility (i.e. to be able to measure samples with different widths), the base plate and one lateral plate are fixed while the other lateral plate can be moved. As long as the distance between the two lateral plates is smaller than the distance between the bottom and the top plate, the cut off frequency is dictated by the height of the waveguide (in our case, it is around 3.4 kHz and up to this frequency only one mode is propagating through the waveguide).

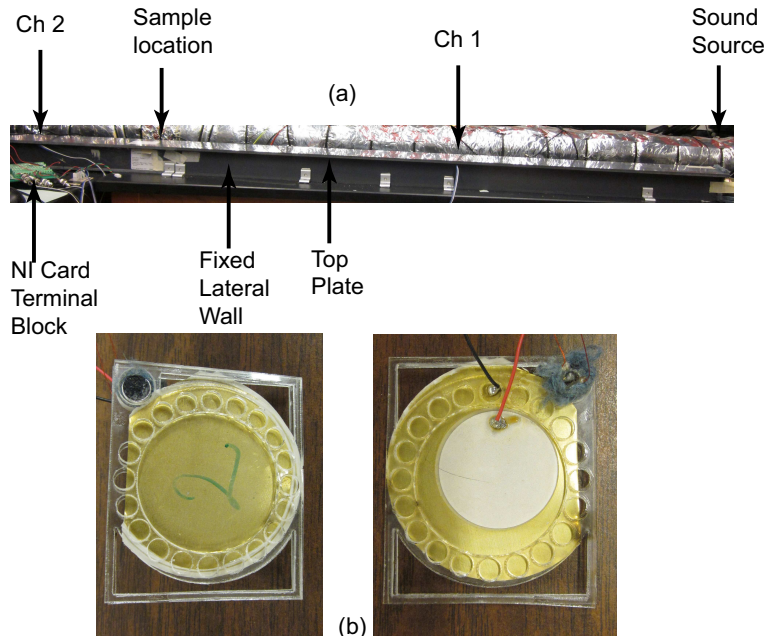


FIGURE 5.8: (a) custom made rectangular acoustic waveguide, (b) rectangular, PZT based active acoustic metamaterial with front view (left, towards the incident wave) and back view (right).

In order to compute the reflection/transmission coefficients, three sets of measurements are performed: for sample, for perfect reflector and for empty waveguide. The reflected pulses are isolated by subtracting the empty waveguide measurement from the measurements when the sample/perfect reflector are placed in the waveguide.

$$S_{11} = \frac{P_{1s}(\omega)}{P_{1r}(\omega)} \quad (5.9)$$

$$S_{21} = \frac{P_{2s}(\omega)}{P_{2a}(\omega)} \quad (5.10)$$

where the subscripts s , r , a denote the sample, perfect reflector and empty waveguide measurements, respectively and the subscripts 1 and 2 denote the measurement points 1 (before the sample) and 2 (after the sample). ω shows that the terms used in the ratio are the Fourier transforms of the time domain signals. We should note that the time domain signals used for the computation of the reflection coefficient contain only the reflected pulses (and not the multiple reflections) and the signals used for the computation of the transmission coefficient are adjusted such that the extra path that the wave travels when the sample is placed in the waveguide compared with the empty waveguide is taken into consideration.

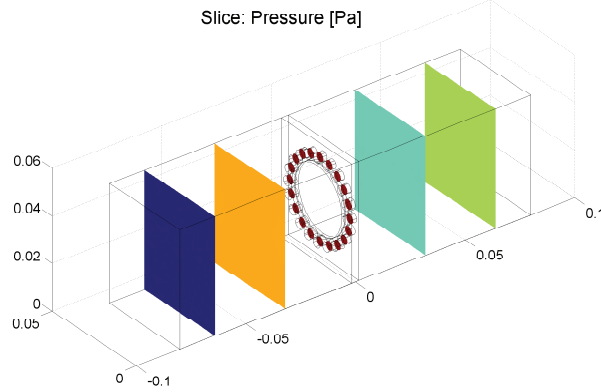


FIGURE 5.9: Numerical simulation results for a perforated panel used as a holder for rectangular, PZT based active acoustic metamaterial.

As it was mentioned in the previous section, the experimental results show improved consistency (i.e. lower imaginary parts for the effective material parameters) if the index of refraction is relatively small when the active element is turned off.

Therefore, numerical simulations have been performed using *COMSOL®* Multi-physics - Acoustics Module in order to determine the best geometrical configuration for the PZT membrane holder (see for example Fig. 5.9, a holder with an index of refraction around 1.5).

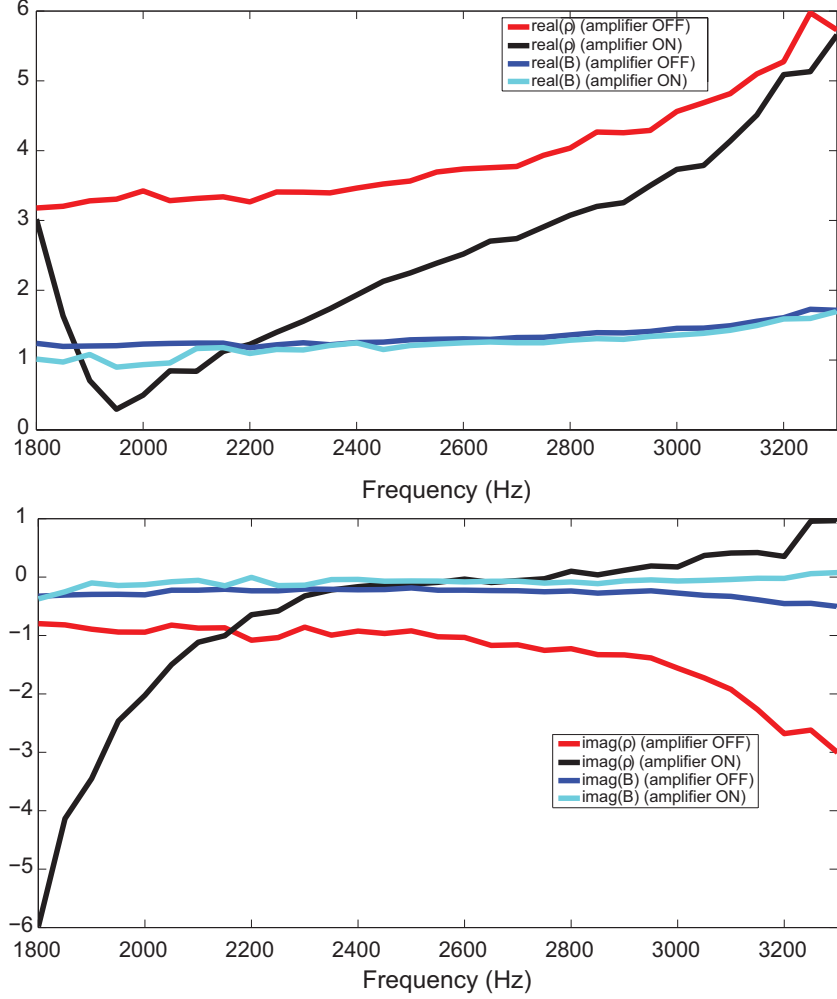


FIGURE 5.10: PZT based AAMM sample 4: real part (top) and imaginary part (bottom) for the effective mass density and bulk modulus.

The results for a rectangular sample (see Fig. 5.8 for snapshots of the actual sample, which is 5 cm x 4.2 cm x 3.5 mm) are presented in Fig. 5.10. This unit cell, generically named *sample 4*, is considered to be 2 cm thick such that at the design

frequency (3 kHz) it is still much smaller than the wavelength. It has the effective mass density around 3 and the bulk modulus close to 1, when the amplifier is turned off. The sample's microphone is connected to an external amplifier with a 500 gain and a band pass filter from 1 kHz to 10 kHz is also used. The sound source (therefore the incident signal) amplitude is chosen such that the amplifier works in the linear regime.

As can be seen, when the active element is in use, the effective mass density is significantly lowered for frequencies around 1.9 kHz while the bulk modulus remains constant over the frequency range in both cases. Also, the imaginary parts of the computed effective material parameters are relatively low, compared with the previous samples.

5.6 Speaker Based Active Acoustic Metamaterials - Rectangular Unit Cell

As we have seen for all the PZT samples considered in the previous sections, there are some disadvantages when they are used for active acoustic metamaterials: the response of these active elements highly varies with frequency and, for some brands, there is a high variation of the response from sample to sample.

Also, the generated signal is relatively small. Therefore, a new active element could be used: a regular membrane speaker which is capable of producing higher levels for the generated acoustic pressure levels. The disadvantage will be a slightly thicker sample, which can be important for some applications. Several relatively small speakers have been tested in order to confirm that indeed, for comparable samples, the speaker based unit cell produces larger values of the pressure field compared with the PZT unit cell. The signals were measured in the rectangular waveguide, the active element was driven from NI card and the pressure level at the two microphones have been measured. The snapshots of this sample, designed also

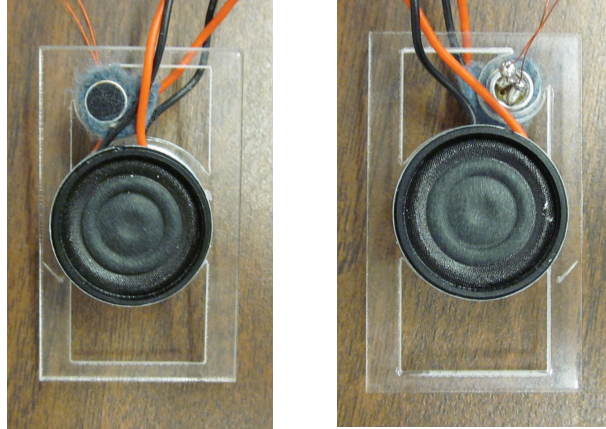


FIGURE 5.11: Speaker based AAMM sample, front view (left, towards the incident wave) and back view (right).

for the rectangular waveguide, are presented in Fig. 5.11.

Similarly with the rectangular, PZT based unit cell, numerical simulations have been performed in order to ensure that the index of refraction when the active element is not in use is around 1.5 (Fig. 5.12).

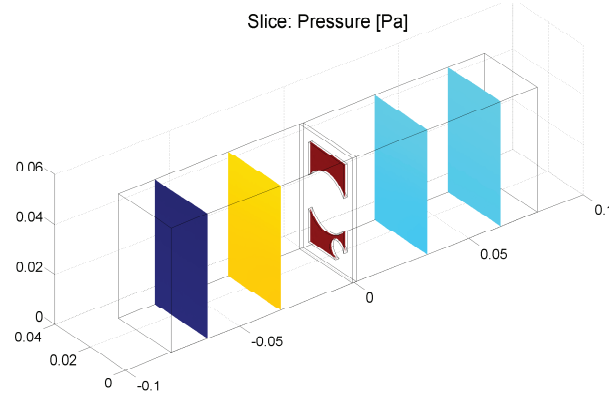


FIGURE 5.12: Numerical simulation results for a perforated panel used as a holder for rectangular, speaker based active acoustic metamaterial.

The speaker holder is made of 1/16" clear cast acrylic sheet using a universal laser cutting machine. Based on several experimental observations, we decided to use an insulating foam when we mount the microphone on the speaker holder and

also to use very thin wires for its connection to the external, low noise amplifier in order to reduce the positive feedback from speakers to the microphone. Also, because our external amplifier is not able to drive the speakers that we use, an additional, regular PC speaker amplifier was used. In order to assess the combined gained of the two amplifiers, we used a reference signal from a standard source and measured the output of the amplifiers chain.

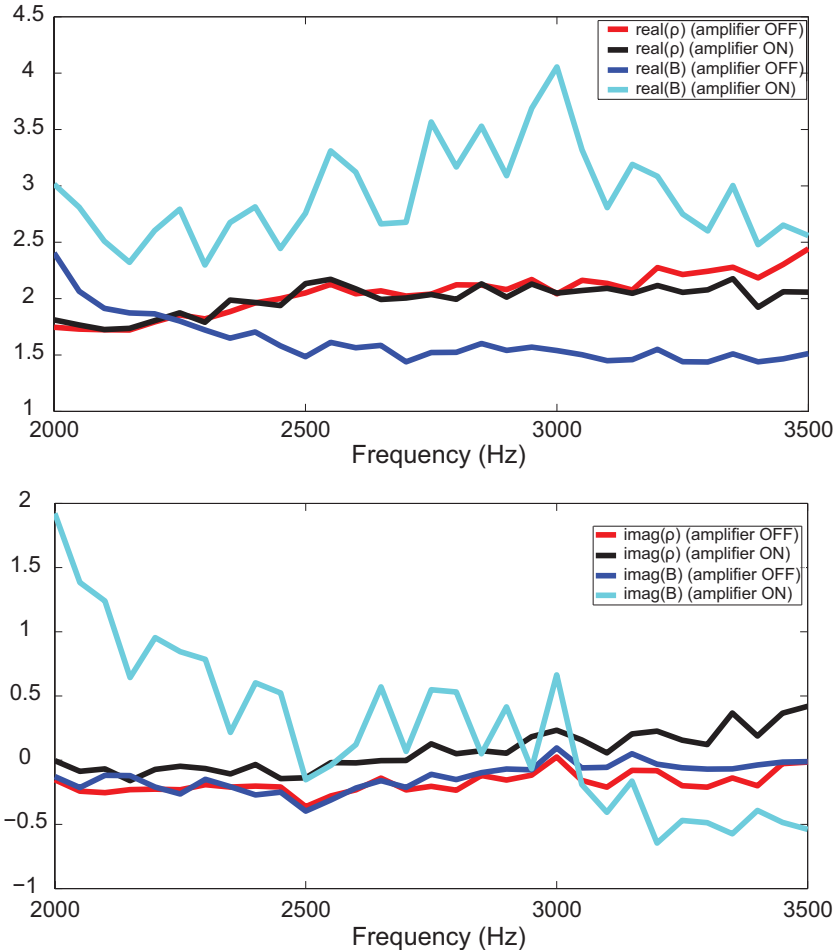


FIGURE 5.13: Speaker based AAMM sample 1: real part (top) and imaginary part (bottom) for the effective mass density and bulk modulus.

The speakers that we use are manufactured by *CUI Inc*, with 23 mm diameter, 5.7 mm thickness, an impedance of 80Ω and a frequency response relatively flat for

frequencies between 1 kHz and 10 kHz. The rated sound pressure level is around 90 dB measured at 50 cm away from the speaker, for a 1 W input power. This unit cell exhibits an effective mass density close to 2 and a bulk modulus around 1.5, when the amplifiers are turned off. When the amplifiers provide a gain of 100 (gain of 10 for each), then the effective mass density does not change but the effective bulk modulus is increasing. This is different compared with the previous samples, where the effective mass density was controlled and the bulk modulus remained virtually unchanged when the active element was involved. Also, we should note that the measurements are much noisier compared with the previous case. We attribute these variations to the way that the speakers are fixed on the holder and the influence that they exercise to each other.

5.7 Conclusions

In this section we have shown a consistent progress towards AAMM. Several problems and their solutions have been identified. A proper unit cell design and experimental setup have been developed. The positive feedback have been reduced without the use of complicated circuits. We therefore demonstrated unit cells that have the same shape but that could have *programmable* material parameters based on their response to the incident wave. The realization of such materials could make the practical implementation of novel applications more feasible. For example, devices imagined in the EM context such as field concentrators or field rotators [64] could be designed for acoustic waves and implemented in practice. Or, as another example, an acoustic diode, a device that will eventually let the acoustic energy flux to travel only in one direction could be realized if the feedback between the sensing element and the acoustic driver will be drastically reduced. This could consequently be used for a myriad of applications (see for example Ref. [79] for a review of some novel applications that are possible now).

6

Conclusions and Suggested Future Work

6.1 Summary

Acoustic metamaterials offer effective material parameters that could be precisely controlled and that are not achievable using traditional materials. Therefore, novel applications that were previously impossible could be realized. This work focuses on the possible ways to realize in practice broadband acoustic metamaterials and on how to use them in various devices and applications. We selected a design method that allows us to create simple unit cells consisting in solid inclusions in a background fluid. These unit cells have the desired effective materials parameters, mass density and bulk modulus. By using a proper measurement technique and experimental setup, we demonstrated that practical acoustic metamaterials (with an effective mass density and a bulk modulus closely matching the predicted values from numerical simulations) could be experimentally realized. Unit cells designed using this procedure were used to realize a 2D acoustic GRIN lens and a 2D acoustic ground cloak in air and could be used to realize a 2D acoustic black hole or a 3D acoustic ground cloak in air. However, this technique of passive metamaterials has its limitations,

including a reduced range for the material parameters that could be obtained when conventional geometries, easy to be implemented in practice are used. Therefore, if one wants to broaden the range for the material parameters, the active acoustic metamaterials (AAMM) should be taken into consideration. One possible way to implement AAMM is to use an active sound source and to control its behavior using an external electric circuit. Two designs using a microphone and a piezoelectric membrane or a speaker have been demonstrated and several samples have been designed and characterized in terms of their ability to show tunable effective material parameters.

6.2 Suggested Future Work

The field of metamaterials in general and of acoustic metamaterials in particular is still in the incipient phase and numerous theoretical and/or experimental works could be suggested. As we have seen in this work, our objective was focused on experimental implementations of acoustic metamaterials and the realization of practical applications. Therefore, our suggestions will be focused in this area too. As we mentioned in the previous chapters, finding the proper amplifier for the PZT crystals or speakers as well as the proper harnessing and holding mechanisms is challenging and future efforts could solve this problem. Moreover, numerical simulations could be performed to find out the best holding mechanism that will provide modest losses and also that will ensure a small index of refraction compared with the air background. A different future work could be focused on multi physics simulations of the actual unit cells using *COMSOL®* Multiphysics and the SPICE model of the amplifier. This will make the search for the best configuration (i.e. active element plus amplifier much easier). Also, a refined theoretical model that will predict the effective material parameters of AAMM more accurately could be defined. This will allow a fine tuning of the material parameters that are only coarse tunable now. In

addition, it looks like better 2D acoustic lens with the same unit cell inside the array but each one of them externally controlled is possible. Therefore, this design, along with a 2D acoustic diode seem feasible at this point and will be a natural next step for experimental realization.

Appendix A

Description of the Data Acquisition Process in the 1D Acoustic Waveguides (Circular and Rectangular)

In this work custom made, circular/rectangular 1D acoustic waveguides have been made and *Matlab*® codes have been developed to perform data acquisitions and compute the effective material parameters (density and bulk modulus) of the samples. The tubes are completely described in Chapter 2 and Chapter 5, respectively. This appendix is intended to help a user to perform measurements.

1. Based on our experience, it is important that all the measurements are performed in the same day in order to enhance the accuracy. Connect the microphones to the data acquisition system and to the power supply. Load the sample, the perfect reflector or leave the tube empty. Pay attention to the mounting system and make sure that the sample is mounted with a minimum sound leakage at the contact between the sample and the tube. Perform the measurements using the appropriate *Matlab*® code, `make_measurement_1DCWG.m` or `make_measurement_1DRWG.m`, respectively. Configure the location where the

data is saved. An example of the data acquisition script is provided below.

2. Compute the effective material parameters using the proper *Matlab*® code. If the samples are not extremely dispersive, the time domain method described in Chapter 2 could be used (*rt_coefficients_td_1DWG.m*). For not circular samples or that are expected to have material parameters which highly vary with frequency, the frequency domain method described in Chapter 5 should be used (*rt_coefficients_fd_1DWG.m*).

Below is an example for a code used to collect the data. The volume of the sound is adjusted such that, for all the measured frequencies, the measured signal at the two channels is not saturated. The volume settings should be kept the same for all the three sets of measurements (*note: the volume settings do not necessarily need to be the same for the entire frequency range*).

```
% input  
fs=44100;  
duration=1;  
avg=10;  
% end of input  
for i=1:30  
    freq=i*100;  
    if freq < 1000 && freq ≠ 100;  
        % signal  
        sig=f_gaussian_pulse(freq, fs, duration, duration/2, 5/freq);  
        vol=1/6;  
        sig=sig*vol;  
        elseif freq < 2000 && freq ≠ 100;  
            % signal
```

```

sig=f_gaussian_pulse(freq, fs, duration, duration/2, 5/freq);
vol=1/3;
sig=sig*vol;
else
% signal
sig=f_gaussian_pulse(freq, fs, duration, duration/2, 5/freq);
vol=1/1.5;
sig=sig*vol;
end
% measure output signals
[ch1,ch2,t]=f_measurement(sig,fs,avg);
meas=struct('t',t,'ch1',ch1,'ch2',ch2);
sample=meas;
save(['sound_01272010_' num2str(freq) '_sample'],'sample','freq','fs');
figure;
subplot(2,1,1);plot(t,ch1);xlabel('time');ylabel('Ch1 Amplitude');grid on;
Title(['F=' num2str(freq) 'Hz']);
subplot(2,1,2);plot(t,ch2);xlabel('time');ylabel('Ch2 Amplitude');grid on;
display(['Frequency ' num2str(freq) 'Hz; run completed']);
end;

```

Appendix B

Description of the Data Acquisition Process in the 2D Parallel Plate Acoustic Waveguide

In this work a custom made, parallel plate 2D acoustic waveguide has been made and *Matlab*[®] codes have been developed to perform data acquisitions and compute the pressure fields inside the waveguide. The 2D waveguide is completely described in Chapter 3 and here we present the auxiliary information that will help a user to perform measurements.

1. Similarly with the 1D acoustic waveguide, it is recommended to perform all the measurements in the same day if multiple measurements are needed (e.g. one set of measurements performed for the empty waveguide and another when the sample is placed in the waveguide). Connect the microphones to the data acquisition system and to the power supply. Hold only the top plate and place the sample inside the waveguide. Use caution during this operation such that the rails that move the scanning microphone will not be bent. Place the sound source in the desired location. Perform the measurements using the last version of *Matlab*[®] graphical user interface (Fig. B.1).

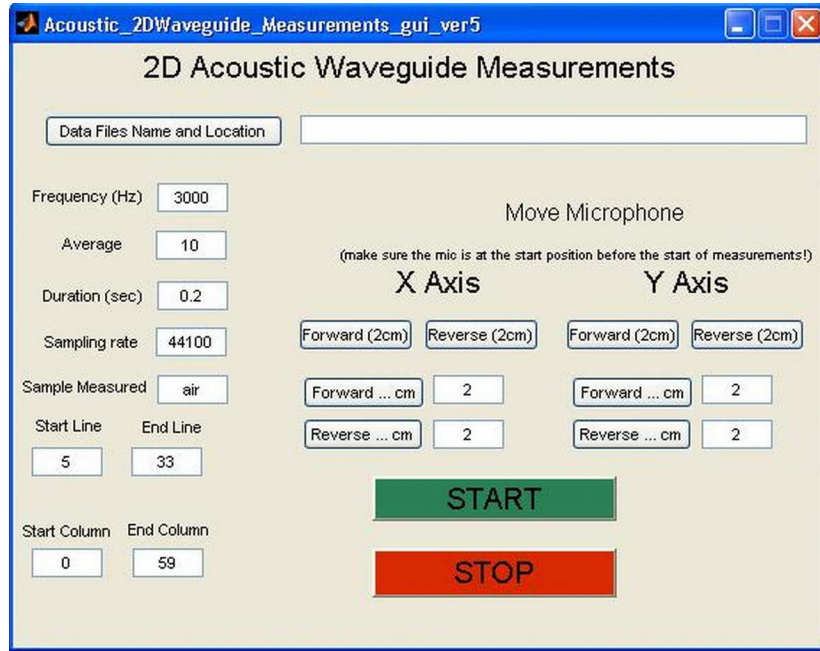


FIGURE B.1: 2D acoustic waveguide graphical user interface.

This code attempts to perform measurements from *Start Line* to *End Line* and from *Start Column* to *End Column*, moving the microphone in a square grid of 2 cm. The dimension of the grid was selected such that there are at least four measurement points per wavelength. If a finer resolution is needed, the callback function of the *START* button should be edited and a different value for the stepper motors moves should be selected. That is, the value of 800 steps which correspond to 2 cm should be changed to a smaller number (e.g. 400 for 1 cm). If the grid is to be square, the values for each stepper motor (for *x* and *y* directions) should be equal (e.g. 400 for each stepper motor will ensure the microphone will move on a square grid of 1 cm).

2. Configure the following parameters:

- Choose the folder where the acquired data is saved;
- Select the central frequency of the pulse that is generated by the speaker

(see Chapter 2 for a complete description of the signal that excites the speaker; if a different signal is desired, the GUI should be change accordingly). The default value is 3 kHz.

- Select the number of measurements averaged for each data point. The average process is necessary in order to increase the signal over noise ratio. The default value is 10.
- Default sampling rate is 44100, imposed by the NI card currently used.
- Specify the name of the sample that is measured. This name will be found in the file name: sound_x_y_frequency_sample_name
- Select the region that is to be scanned. The default values indicate the minimum and maximum allowed values.

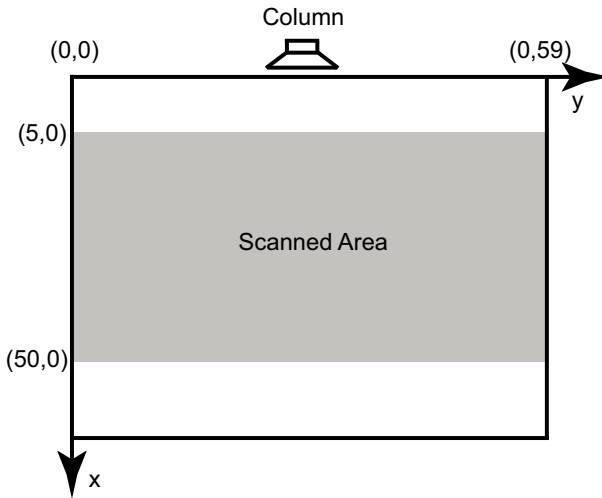


FIGURE B.2: 2D acoustic waveguide: schematic diagram.

For example, *Start Line 5* indicates a start from 10 cm away from the edge of the waveguide. Every line and column is 2 cm spaced from each other (see Fig. B.2). For example, $x = 15$ and $y = 25$ means that the microphone is 30 cm in the x direction and 50 cm in the y direction. Please note the limit values: 5 and 50 for x axis, 0 and 59 for y axis.

- Move the microphone to the start position using the GUI buttons for moving the microphone. Use either the predefined buttons or enter your own value. Make sure that you enter the correct value as the microphone cannot go over the edges of the waveguide and, as of now, there is no feedback about the microphone position inside the waveguide.
 - Use the START/STOP buttons to start or stop the acquisition process. Please make sure there scanning area is not overlapping the sample, as the microphone cannot go over the sample.
3. Use the collected data and analyze them as desired. Please note that each data point contains two signals: the reference signal collected by the microphone placed in the fixed position and the data signal collected by the microphone moving inside the waveguide.

Below is an example of a *Matlab*® script used to generate a movie that shows the wave propagation inside the waveguide.

```

clear all;
clc;
run=0;
m=linspace(1,58,58);
n=linspace(0,50,50);
q=linspace(1,44101,44101);
% ALIGN ALL THE COLLECTED SIGNALS USING THE REFERENCE
load (['sound_24032011_3000_10_0_cloakABS']);
s1ref=cloak.ch1;
for k=1:58
    for l=10:34
        load (['sound_24032011_3000_' num2str(l) '_' num2str(k-1) '_cloakABS']);
    end
end

```

```

s1=reflector.ch1;
s2=reflector.ch2;
[s1a, dt]=f_overlap_signals(s1,s1ref);
s2a=f_delay_signal(s2,dt);

% OR USE THE METHOD OF CROSS CORRELATION

% [z,lags]=xcorr(s1ref,s1);
% [a,dt]=max(z);
% s2b=f_delay_signal(s2,dt);

% SAVE THE ALIGNED SIGNALS USING A SUBSCRIPT "a"

%TO DENOTE THAT THE ALIGNEMENT HAS BEEN PERFORMED

save(['s2cloakABS_' num2str(l) '_' num2str(k-1)],'s2a');
display(['Column' num2str(k-1) ';Line' num2str(l) ': run completed']);
end;

end;

%SAVE NULL SIGNALS FOR LINES NOT MEASURED (x=0 to 5)

%IF THESE LINES ARE SHOWN IN THE MOVIE

s1ref(:)=0;
for l=0:5
    for k=1:58
        s2a=s1ref;
        save(['s2cloakABS_' num2str(l-1) '_' num2str(k-1)],'s2a');
        display(['Column' num2str(k-1) ';Line' num2str(l-1) ':run completed']);
        end;
    end;
end;

%CLOAK POINTS MEASURED

S2C=zeros(40,58,301);
for k=1:58

```

```

for l=11:35
    load ([`s2cloakABS_` num2str(l-1) '_' num2str(k-1) ]);
    S2C(l,k,:)=s2a(5350:5650);
end;
end;

S2Cnew=flipdim(S2C,1);

figure;
for it=1:301;
%close all;

%USE THE INTERPOLATION FOR A BETTER MOVIE
S2CnewI=interp2(S2Cnew(:,:,it),'spline');imagesc(S2CnewI,[-5 5]);
AXIS([0 y*58/115*2 0 x*40/79*2]);
daspect([1 1 1]);%colorbar;
set(gca,'FontSize',14,'FontName','Arial');
xlabel('Position (cm)');
ylabel('Position (cm)')
Title('Triangle+CloakABS','FontSize',16,'FontName','Arial','FontWeight','bold');
line([0 y*58/115*2],[0 0],'Color','r','LineWidth',4)
line([42.85 60 77.15],[0 5.7 0],'Color','r','LineWidth',4)
line([42.85 60 77.15],[0 10 0],'Color','r','LineWidth',4)
drawnow;

%SAVE IMAGES AND MAKE A MOVIE FROM THE IMAGE SEQUENCE
saveas(gcf,['frame' num2str(it) '.jpg'])
display(it);
end;

```

Appendix C

3D Acoustic Cloak Transformations

C.1 Square Pyramid Cloak

For the square pyramid cloak presented in Fig. 4.6, let consider the particular case presented below:

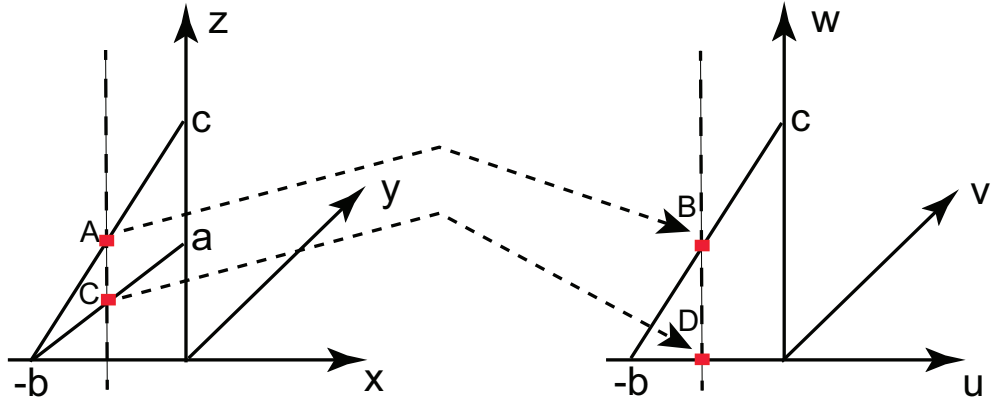


FIGURE C.1: Cross section square pyramid cloak.

We are looking for a linear transformation that will map the point A from real space into the point B in virtual space, and similarly the point C to point D, respectively. The easiest way to obtain such a transformation will be the following:

$$\begin{cases} u = x \\ v = y \\ w = c_1x + c_2y + c_3z + c_4 \end{cases} \quad (C.1)$$

Also:

$$\begin{cases} \frac{z}{a} = \frac{x+b}{b} & , \text{for line including point C} \\ \frac{z}{a} = \frac{x+b}{b} & , \text{for line including point A} \end{cases} \quad (C.2)$$

Then:

$$\begin{cases} w = c_1x + c_2y + c_3\frac{a}{b}(x+b) + c_4 = 0 & , \text{for point D} \\ w = c_1x + c_2y + c_3\frac{c}{b}(x+b) + c_4 = \frac{c}{b}(x+b) & , \text{for point B} \end{cases} \quad (C.3)$$

Subtracting the last two equations, we obtain $c_3 = \frac{c}{c-a}$. For $x=0, y=0, z=a$ we need $w=0$; therefore, $c_4 = -a\frac{c}{c-a}$. However, the other two constants c_1 and c_2 should be determined for the particular cases of x and y coordinates. For example, for the particular case depicted in Fig. C.1 where $y=0$, $c_1 = -\frac{a}{b}\frac{c}{c-a}$ (from the condition that the point $C(x,0,z)$ will be mapped to point $D(u,0,0)$) and we can choose $c_2 = 0$. Similarly, for the other regions. In order to verify that selecting $c_2 = 0$ will work for the case when y is not 0, we will consider the case presented in Fig. C.2.

We should note that b' is the distance between the origin and the edge of the pyramid ($z=0$) for the points of interest and θ is the angle between this line and the x axis.

$$\begin{cases} b' = \frac{b}{\cos\theta} \\ w = \frac{c}{c-a} \left(-\frac{a}{b'}d + z - a \right) = \frac{c}{c-a} \left(-\frac{a}{b} \frac{x}{\sqrt{x^2+y^2}} \sqrt{x^2+y^2} + z - a \right) = \frac{c}{c-a} \left(-\frac{a}{b}x + z - a \right) \end{cases} \quad (C.4)$$

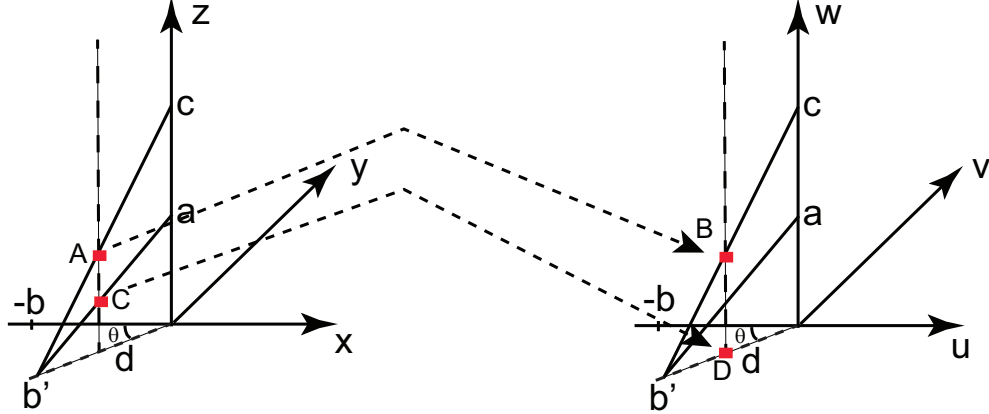


FIGURE C.2: Cross section cone cloak.

Therefore, the same expression of the transformation is valid for any value of y coordinate, as long as the sign of the x coordinate is not changing.

C.2 Cone Shaped Cloak

We will consider the case depicted in Fig. C.2, only this time the base of the pyramid is a circle. Let us consider, based on the previous section results, that the transformation that we need is the following:

$$\begin{cases} u = x \\ v = y \\ w = \frac{c}{c-a} \left(\frac{a}{b} \rho(x, y) + z - a \right) \end{cases} \quad (\text{C.5})$$

where $\rho(x, y) = \sqrt{x^2 + y^2}$.

In order to verify that this transformation is a proper one, we choose an arbitrary point on the object to hide in real space and check that it is mapped into the ground in the virtual space ($w=0$):

$$\begin{cases} x = d \cos \theta \\ y = d \sin \theta \\ z = \frac{a(b-d)}{b} \end{cases} \quad (\text{C.6})$$

So, using the transformation expression:

$$w = \frac{c}{c-a} \left(\frac{a}{b}d + \frac{a(b-d)}{b} - a \right) = 0 \quad (\text{C.7})$$

For a point on the cloaking shell in real space, we need to verify that the transformation keeps it at the same location in the virtual space (i.e. $w=z$):

$$\begin{cases} x = d \cos \theta \\ y = d \sin \theta \\ z = \frac{c(b-d)}{b} \end{cases} \quad (\text{C.8})$$

So, using the transformation expression:

$$w = \frac{c}{c-a} \left(\frac{a}{b}d + \frac{c(b-d)}{b} - a \right) = \frac{c(b-d)}{b} = z \quad (\text{C.9})$$

C.3 Crescent Shaped Cloak

Again, we start looking for a transformation that will map the point from the object to hide to the ground and that keeps unchanged the points for the cloaking region.

$$\begin{cases} u = x \\ v = y \\ w = c_1(x, y) + c_2(x, y)z \end{cases} \quad (\text{C.10})$$

Also:

$$\begin{cases} \left(\frac{x}{r}\right)^2 + \left(\frac{y}{r}\right)^2 + \left(\frac{z}{br}\right)^2 = 1 & , \text{for the object to hide} \\ \left(\frac{x}{r}\right)^2 + \left(\frac{y}{r}\right)^2 + \left(\frac{z}{ar}\right)^2 = 1 & , \text{for the cloaking region} \end{cases} \quad (\text{C.11})$$

Then:

$$\begin{cases} z = br\sqrt{1 - \left(\left(\frac{x}{r}\right)^2 + \left(\frac{y}{r}\right)^2\right)} & , \text{ for the object to hide} \\ z = ar\sqrt{1 - \left(\left(\frac{x}{r}\right)^2 + \left(\frac{y}{r}\right)^2\right)} & , \text{ for the cloaking region} \end{cases} \quad (\text{C.12})$$

Imposing the condition $w = 0$ for the point mapped from the object to hide to ground and $w = ar\sqrt{1 - \frac{x^2+y^2}{r^2}}$:

$$\begin{cases} w = c_1(x, y) + c_2(x, y) br\sqrt{1 - \frac{x^2+y^2}{r^2}} = 0 \\ w = c_1(x, y) + c_2(x, y) ar\sqrt{1 - \frac{x^2+y^2}{r^2}} = ar\sqrt{1 - \frac{x^2+y^2}{r^2}} \end{cases} \quad (\text{C.13})$$

From these two equations we obtain:

$$\begin{cases} c_1(x, y) = -\frac{a}{a-b} br\sqrt{1 - \frac{x^2+y^2}{r^2}} \\ c_2(x, y) = \frac{a}{a-b} \end{cases} \quad (\text{C.14})$$

Therefore:

$$\begin{cases} u = x \\ v = y \\ w = \frac{a}{a-b} \left(-br\sqrt{1 - \frac{x^2+y^2}{r^2}} + z \right) \end{cases} \quad (\text{C.15})$$

Bibliography

- [1] M. Lapine and S. Tretyakov. Contemporary notes on metamaterials. *IET Microwaves Antennas & Propagation*, 1(1):3–11, 2007.
- [2] W. S. Weiglhofer and A. Lakhtakia. *Introduction to complex mediums for optics and electromagnetics*. SPIE Optical Engineering Press, 1999.
- [3] T. J. Cui, R. Liu, and D. R. Smith. *Metamaterials : theory, design, and applications*. Springer, New York, 2010.
- [4] V. G. Veselago. Electrodynamics of substances with simultaneously negative values of sigma and mu. *Soviet Physics Uspekhi-USSR*, 10(4):509–514, 1968.
- [5] J. B. Pendry, A. J. Holden, W. J. Stewart, and I. Youngs. Extremely low frequency plasmons in metallic mesostructures. *Physical Review Letters*, 76(25):4773–4776, 1996.
- [6] J. B. Pendry, A. J. Holden, D. J. Robbins, and W. J. Stewart. Magnetism from conductors and enhanced nonlinear phenomena. *Ieee Transactions on Microwave Theory and Techniques*, 47(11):2075–2084, 1999.
- [7] D. R. Smith, W. J. Padilla, D. C. Vier, S. C. Nemat-Nasser, and S. Schultz. Composite medium with simultaneously negative permeability and permittivity. *Physical Review Letters*, 84(18):4184–4187, 2000.
- [8] J. B. Pendry. Negative refraction makes a perfect lens. *Physical Review Letters*, 85(18):3966–3969, 2000.
- [9] D. Schurig and D. R. Smith. Negative index lens aberrations. *Physical Review E*, 70(6):065601(R), 2004.
- [10] D. R. Smith, J. J. Mock, A. F. Starr, and D. Schurig. Gradient index metamaterials. *Physical Review E*, 71(3):036609, 2005.
- [11] J. B. Pendry, D. Schurig, and D. R. Smith. Controlling electromagnetic fields. *Science*, 312(5781):1780–1782, 2006.

- [12] D. Schurig, J. J. Mock, B. J. Justice, S. A. Cummer, J. B. Pendry, A. F. Starr, and D. R. Smith. Metamaterial electromagnetic cloak at microwave frequencies. *Science*, 314(5801):977–980, 2006.
- [13] J. Li and C. T. Chan. Double-negative acoustic metamaterial. *Physical Review E*, 70(5):055602(R), 2004.
- [14] Z. Yang, J. Mei, M. Yang, N. H. Chan, and P. Sheng. Membrane-type acoustic metamaterial with negative dynamic mass. *Physical Review Letters*, 101(20):204301, 2008.
- [15] S. H. Lee, C. M. Park, Y. M. Seo, Z. G. Wang, and C. K. Kim. Acoustic metamaterial with negative density. *Physics Letters A*, 373(17):4464, 2009.
- [16] N. Fang, D. J. Xi, J. Y. Xu, M. Ambati, W. Srituravanich, C. Sun, and X. Zhang. Ultrasonic metamaterials with negative modulus. *Nature Materials*, 5(6):452–456, 2006.
- [17] S. Zhang, L. L. Yin, and N. Fang. Focusing ultrasound with an acoustic metamaterial network. *Physical Review Letters*, 102(19):194301, 2009.
- [18] J. S. Li, L. Fok, X. B. Yin, G. Bartal, and X. Zhang. Experimental demonstration of an acoustic magnifying hyperlens. *Nature Materials*, 8(12):931–934, 2009.
- [19] Z. Yang, H. M. Dai, N. H. Chan, G. C. Ma, and P. Sheng. Acoustic metamaterial panels for sound attenuation in the 50-1000 hz regime. *Applied Physics Letters*, 96(4):041906, 2010.
- [20] S. X. Yang, J. H. Page, Z. Y. Liu, M. L. Cowan, C. T. Chan, and P. Sheng. Focusing of sound in a 3d phononic crystal. *Physical Review Letters*, 93(2):024301, 2004.
- [21] L. Fok, M. Ambati, and X. Zhang. Acoustic metamaterials. *Materials Research Society Bulletin*, 33(10):931–934, 2008.
- [22] D. Torrent, A. Hakansson, F. Cervera, and J. Sanchez-Dehesa. Homogenization of two-dimensional clusters of rigid rods in air. *Physical Review Letters*, 96(20):204302, 2006.
- [23] D. Torrent and J. Sanchez-Dehesa. Effective parameters of clusters of cylinders embedded in a nonviscous fluid or gas. *Physical Review B*, 74(22):224305, 2006.
- [24] S. S. Lin, T. J. Huang, J. Sun, and T. T. Wu. Gradient-index phononic crystals. *Physical Review B*, 79(9):094302, 2009.

- [25] Y. Q. Ding, Z. Y. Liu, C. Y. Qiu, and J. Shi. Metamaterial with simultaneously negative bulk modulus and mass density. *Physical Review Letters*, 99(9):093904, 2007.
- [26] G. W. Milton, M. Briane, and J. R. Willis. On cloaking for elasticity and physical equations with a transformation invariant form. *New Journal of Physics*, 8:248, 2006.
- [27] S. A. Cummer and D. Schurig. One path to acoustic cloaking. *New Journal of Physics*, 9:45, 2007.
- [28] H. Y. Chen and C. T. Chan. Acoustic cloaking in three dimensions using acoustic metamaterials. *Applied Physics Letters*, 91(18):183518, 2007.
- [29] S. A. Cummer, M. Rahm, and D. Schurig. Material parameters and vector scaling in transformation acoustics. *New Journal of Physics*, 10:115025, 2008.
- [30] S. A. Cummer, B. I. Popa, D. Schurig, D. R. Smith, J. Pendry, M. Rahm, and A. Starr. Scattering theory derivation of a 3d acoustic cloaking shell. *Phys. Rev. Lett.*, 100:024301, 2008.
- [31] D. Torrent and J. Sanchez-Dehesa. Acoustic cloaking in two dimensions: a feasible approach. *New Journal of Physics*, 10:063015, 2008.
- [32] Y. Cheng, F. Yang, J. Y. Xu, and X. J. Liu. A multilayer structured acoustic cloak with homogeneous isotropic materials. *Applied Physics Letters*, 92(15):151913, 2008.
- [33] A. N. Norris. Acoustic cloaking theory. *Proceedings of the Royal Society A: Mathematical, Physical and Engineering Science*, 464(2097):2411–2434, 2008.
- [34] D. Torrent and J. Sanchez-Dehesa. Anisotropic mass density by two-dimensional acoustic metamaterials. *New Journal of Physics*, 10:023004, 2008.
- [35] D. Torrent and J. Sanchez-Dehesa. Acoustic cloaking in two dimensions: a feasible approach. *New Journal of Physics*, 10:063015, 2008.
- [36] J. B. Pendry and J. Li. An acoustic metafluid: realizing a broadband acoustic cloak. *New Journal of Physics*, 10:115032, 2008.
- [37] B. I. Popa and S. A. Cummer. Design and characterization of broadband acoustic composite metamaterials. *Physical Review B*, 80(17):174303, 2009.
- [38] A. Baz. The structure of an active acoustic metamaterial with tunable effective density. *New Journal of Physics*, 11:123012, 2009.

- [39] W. Akl and A. Baz. Multi-cell active acoustic metamaterial with programmable bulk modulus. *Journal of Intelligent Material Systems and Structures*, 21(5):541–556, 2010.
- [40] D. T. Blackstock. *Fundamentals of physical acoustics*. Wiley, New York, 2000.
- [41] D. R. Smith, S. Schultz, P. Markos, and C. M. Soukoulis. Determination of effective permittivity and permeability of metamaterials from reflection and transmission coefficients. *Physical Review B*, 65(19):195104, 2002.
- [42] V. Fokin, M. Ambati, C. Sun, and X. Zhang. Method for retrieving effective properties of locally resonant acoustic metamaterials. *Phys. Rev. B*, 76(14):144302, 2007.
- [43] L. Zigoneanu, B. I. Popa, A.F. Starr, and S. A. Cummer. Design and measurements of a broadband 2d acoustic metamaterial with anisotropic mass density. *Journal of Applied Physics*, 109:054906, 2011.
- [44] D. Li, L. Zigoneanu, B. I. Popa, and S. A. Cummer. Design of an acoustic metamaterial lens using genetic algorithms. *The Journal of the Acoustical Society of America*, 132(4):2823–2833, 2012.
- [45] B. I. Popa, L. Zigoneanu, and S. A. Cummer. Experimental acoustic ground cloak in air. *Physical Review Letters*, 106:253901, 2011.
- [46] D. Y. Maa. Potential of microperforated panel absorber. *The Journal of the Acoustical Society of America*, 104(5):2861–2866, 1998.
- [47] Y.Y. Lee, E.W.M. Lee, and C.F. Ng. Sound absorption of a finite flexible micro-perforated panel backed by an air cavity. *Journal of Sound and Vibration*, 287(12):227–243, 2005.
- [48] J. Kang and M.W. Brocklesby. Feasibility of applying micro-perforated absorbers in acoustic window systems. *Applied Acoustics*, 66(6):669–689, 2005.
- [49] D. Y. Maa. General theory and design of microperforated-panel absorbers. *Acta Acustica*, 5, 1997.
- [50] K. Sakagami, M. Morimoto, M. Yairi, and A. Minemura. A pilot study on improving the absorptivity of a thick microperforated panel absorber. *Applied Acoustics*, 69(2):179–182, 2008.
- [51] T. Bravo, C. Maury, and C. Pinhede. Vibroacoustic properties of thin micro-perforated panel absorbers. *The Journal of the Acoustical Society of America*, 132(2):789–798, 2012.

- [52] C. Yang, L. Cheng, and J. Pan. Absorption of oblique incidence sound by a finite micro-perforated panel absorber. *The Journal of the Acoustical Society of America*, 133(1):201–209, 2013.
- [53] ASTM Standard E2611-09. *"Standard Test Method for Measurement of Normal Incidence Sound Transmission of Acoustical Materials Based on the Transfer Matrix Method"*. ASTM International, West Conshohocken, PA, 2009.
- [54] ASTM Standard E413-10. *"Classification for Rating Sound Insulation"*. ASTM International, West Conshohocken, PA, 2010.
- [55] C. Gomez-Reino, C. Bao, and M. V. Perez. *Gradient-index optics : fundamentals and applications*. Springer, Berlin, 2002.
- [56] D. Torrent and J. Sanchez-Dehesa. Acoustic metamaterials for new two-dimensional sonic devices. *New Journal of Physics*, 9:323, 2007.
- [57] A. Climente, D. Torrent, and J. Sanchez-Dehesa. Sound focusing by gradient index sonic lenses. *Applied Physics Letters*, 97(10):104103, 2010.
- [58] T. P. Martin, M. Nicholas, G. J. Orris, L. W. Cai, D. Torrent, and J. Sanchez-Dehesa. Sonic gradient index lens for aqueous applications. *Applied Physics Letters*, 97(11):113503, 2010.
- [59] S. S. Peng, Z. J. He, H. Jia, A. Q. Zhang, C. Y. Qiu, M. Z. Ke, and Z. Y. Liu. Acoustic far-field focusing effect for two-dimensional graded negative refractive-index sonic crystals. *Applied Physics Letters*, 96(26):263502, 2010.
- [60] L. Zigoneanu, B. I. Popa, and S. A. Cummer. Design and measurements of a broadband two-dimensional acoustic lens. *Physical Review B*, 84:024305, 2011.
- [61] A. B Wood. *A textbook of sound; being an account of the physics of vibrations with special reference to recent theoretical and technical developments*. Macmillan, New York, 1955.
- [62] A. A. Krokhin, J. Arriaga, and L. N. Gumen. Speed of sound in periodic elastic composites. *Physical Review Letters*, 91:264302, 2003.
- [63] U. Leonhardt. Optical conformal mapping. *Science*, 312(5781):1777, 2006.
- [64] H. Chen, C. T. Chan, and P. Sheng. Transformation optics and metamaterials. *Nature Materials*, 9(5):387–396, 2010.
- [65] U. Leonhardt and T. G. Philbin. General relativity in electrical engineering. *New Journal of Physics*, 8:247, 2006.
- [66] E. E. Narimanov and A. V. Kildishev. Optical black hole: Broadband omnidirectional light absorber. *Applied Physics Letters*, 95(4):041106, 2009.

- [67] W. L. Lu, J. F. Jin, Z. F. Lin, and H. Y. Chen. A simple design of an artificial electromagnetic black hole. *Journal of Applied Physics*, 108(6):064517, 2010.
- [68] S. Y. Liu, L. Li, Z. F. Lin, H. Y. Chen, J. Zi, and C. T. Chan. Graded index photonic hole: Analytical and rigorous full wave solution. *Physical Review B*, 82(5):054204, 2010.
- [69] Q. Cheng, T. J. Cui, W. X. Jiang, and B. G. Cai. An omnidirectional electromagnetic absorber made of metamaterials. *New Journal of Physics*, 12:063006, 2010.
- [70] H. Y. Chen, R. X. Miao, and M. A. Li. Transformation optics that mimics the system outside a schwarzchild black hole. *Optics Express*, 18(14):15183, 2010.
- [71] R. Q. Li, X. F. Zhu, B. Liang, Y. Li, X. Y. Zou, and J. C. Cheng. A broadband acoustic omnidirectional absorber comprising positive-index materials. *Applied Physics Letters*, 99(19):193507, 2011.
- [72] A. Climente, D. Torrent, and J. Sanchez-Dehesa. Noise reduction by perfect absorbers based on acoustic metamaterials. In *Proceedings of the ASME 2011 International Mechanical Engineering Congress & Exposition*, Denver, CO, 2011.
- [73] A. Climente, D. Torrent, and J. Sanchez-Dehesa. Omnidirectional broadband acoustic absorber based on metamaterials. *Applied Physics Letters*, 100(14):144103, 2012.
- [74] C. Q. Wang and L. X. Huang. On the acoustic properties of parallel arrangement of multiple micro-perforated panel absorbers with different cavity depths. *Journal of the Acoustical Society of America*, 130(1):208–218, 2011.
- [75] H. Y. Chen and C. T. Chan. Acoustic cloaking and transformation acoustics. *Journal of Physics D-Applied Physics*, 43(11), 2010.
- [76] C. K. Kim, S. H. Lee, C. M. Park, Y. M. Seo, and Z. G. Wang. Acoustic metamaterial with negative density. *Physics Letters A*, 373(48):4464–4469, 2009.
- [77] A. M. Baz. An active acoustic metamaterial with tunable effective density. *Journal of Vibration and Acoustics*, 132(4):041011, 2010.
- [78] Wael Akl and Amr Baz. Analysis and experimental demonstration of an active acoustic metamaterial cell. *Journal of Applied Physics*, 111(4):044505, 2012.
- [79] B. Liang, B. Yuan, and J. C. Cheng. Acoustic diode: Rectification of acoustic energy flux in one-dimensional systems. *Physical Review Letters*, 103:104301, 2009.

Biography

Lucian Zigoneanu graduated from Polytechnic University of Bucharest, Romania with a BS degree in Electronics and Telecommunications (major in Applied Electronics) and a MS degree in Quality and Reliability Engineering. He worked for several years as service engineer for Excel Comp, Bucharest and Romsys SA, Bucharest and was also exchange student at École Nationale Supérieure d'Arts et Métiers, Paris, France (1997), visiting engineer at Wincor Nixdorf, Paderborn, Germany (2003) and Dell Europe, Bracknell, UK (2004). In 2006, he received a MS degree from Mechanical Engineering Department of Louisiana State University in Baton Rouge, LA. From 2008, he matriculated to Duke University in Durham, NC, earning the Ph.D degree in Electrical Engineering in 2013.

Awards

- 3rd place Student Poster Competition, NC-ASA meeting, Concord NC (2011)

Publications

- L. Zigoneanu, B. I. Popa, and S. A. Cummer, “Experimental characterization of perforated plates as acoustic metamaterials”. (to be submitted, 2013)
- G. Lu, S. A. Cummer, J. Li, and L. Zigoneanu et al., “Coordinated observations of sprites and in-cloud lightning flash structure”. (in review, 2013)
- Y. Xie, B. I. Popa, L. Zigoneanu, and S. A. Cummer, “Measurements of Broadband Negative Index in Space-Coiling Acoustic Metamaterials”. (in review, 2013)
- L. Zigoneanu, B. I. Popa, S. A. Cummer, “Sound manipulation with acoustic metamaterials”. Proceedings of the Internoise 2012/ASME NCAD meeting, New York NY (2012).

- J. Li, S. A. Cummer, G. Lu, L. Zigoneanu, “Charge moment change and lightning-driven electric fields associated with negative sprites and halos”. *J. Geophys. Res.*, v. 117, A09310, 2012.
- D. Li, L. Zigoneanu, B. I. Popa and S. A. Cummer, “Design of an Acoustic Metamaterial Lens Using Genetic Algorithms”. *J. Acoust. Soc. Am.*, 132(4): 2823, 2012.
- B. I. Popa, L. Zigoneanu, and S. A. Cummer, “Experimental acoustic ground cloak in air”. *Phys. Rev. Lett.*, 106:253901, 2011.
- L. Zigoneanu, B. I. Popa, and S. A. Cummer, “Design and measurements of a broadband two-dimensional acoustic lens”. *Phys. Rev. B*, 84:024305, 2011.
- L. Zigoneanu, B. I. Popa, A.F. Starr, and S. A. Cummer, “Design and measurements of a broadband 2D acoustic metamaterial with anisotropic mass density”. *J. Appl. Phys.*, 109:054906, 2011.

Conference and Workshop Presentations

- Romanian Ministry of Education and Research, UEFISCDI, Bucharest, Romania (2012)
- Duke Pratt School of Engineering, External Advisory Board Visit, Durham NC (2012)
- International Congress on Noise Control Engineering (Inter-Noise), New York NY (2012)
- Duke Pratt School of Engineering, Graduate Research Workshop, Durham NC (2012)
- North Carolina chapter of the Acoustical Society of America meeting, Concord NC (2011)
- Graduate Student Annual Conference, Department of Mechanical Engineering, LSU (2006)